

LIQUID-PHASE EPITAXY OF DOPED KY(WO₄)₂ LAYERS FOR WAVEGUIDE LASERS

THÈSE N° 3390 (2005)

PRÉSENTÉE À LA FACULTÉ SCIENCES ET TECHNIQUES DE L'INGÉNIEUR

Institut d'imagerie et optique appliquée

SECTION DE MICROTHECHNIQUE

ÉCOLE POLYTECHNIQUE FÉDÉRALE DE LAUSANNE

POUR L'OBTENTION DU GRADE DE DOCTEUR ÈS SCIENCES

PAR

Yaroslav ROMANYUK

M.Sc. in Chemistry, Lesya Ukrainka Volyn State University, Lutsk, Ukraine
et de nationalité ukrainienne

acceptée sur proposition du jury:

Prof. R.P. Salathé, directeur de thèse

Prof. B. Deveaud-Plédran, rapporteur

Prof. M. Pollnau, rapporteur

Dr D. Rytz, rapporteur

Lausanne, EPFL
2006

Abstract

Rare-earth-ion doped $\text{KY}(\text{WO}_4)_2$ (hereafter KYW:RE) is a promising material for novel solid-state lasers. Its low laser threshold, high laser efficiency, and third-order nonlinear effects have stimulated research towards miniaturized thin-film waveguide lasers and amplifiers.

A method of liquid-phase epitaxy (LPE) to produce KYW:RE thin layers with vertical substrate dipping has been developed. Undoped KYW crystals having laser-grade polished (010) faces served as the substrates. Two solvents, the tungstate $\text{K}_2\text{W}_2\text{O}_7$ and the chloride NaCl-KCl-CsCl , were tested.

The $\text{K}_2\text{W}_2\text{O}_7$ solvent contains no impurity ions and is a good solvent for KYW, which is the only stable phase to be crystallized from the solution. The substrate position and rotation rate were optimized by numerical simulation of liquid flow in the crucible in order to obtain uniform layer thickness. A crystallization rate of $1.2 \text{ mg K}^{-1} \text{ g}^{-1}$ at the growth temperature of 900°C results in high-quality layers with thickness up to $100 \mu\text{m}$ and RE^{3+} concentrations ranging from 0.2 to 3 mol% with respect to Y^{3+} . Dipping the substrate at 0.1-0.3 K above the saturation point helps to eliminate surface defects and assure a defect-free interface. An undoped overlay of KYW can subsequently be grown on KYW:RE layers to obtain buried structures.

The chloride NaCl-KCl-CsCl solvent with its melting point of 480°C allows epitaxial growth at temperatures as low as 520°C , which can reduce thermal stress in heavily RE-doped layers. However, the LPE is complicated by the formation of parasitic phases and pronounced 3D island nucleation, which limit the maximum layer thickness to approx. $10 \mu\text{m}$.

The original concept of microchannel epitaxy (MCE) has been applied for the first time to produce channel structures with an oxide material. KYW:RE ribs, $40\text{-}200 \mu\text{m}$ wide and $3\text{-}20 \mu\text{m}$ high, can be grown from the $\text{K}_2\text{W}_2\text{O}_7$ solvent on KYW substrates with a patterned gold or platinum mask deposited on the substrate surface.

Surface and buried planar layers as well as channels of KYW:RE have been tested as optical waveguides. End-coupling and propagation of laser light at 633 nm or pumping at 981 nm results in excellent passive (633 nm) or active (e.g. 1030-nm Yb^{3+} fluorescence) waveguiding performance with propagation losses of only $0.1\text{-}0.2 \text{ dB cm}^{-1}$.

Continuous-wave (CW) lasing in both surface and buried KYW:Yb planar waveguides has been demonstrated at 1025 nm in the fundamental mode. The maximum output power is 290 mW and the slope efficiency is as high as 80.4% , which is, to the best of our knowledge, the highest value ever reported for a planar waveguide laser.

Résumé

Les doubles tungstates du type $KY(WO_4)_2$ dopés par des ions de terres rares (notés KYW:RE) sont des matériaux prometteurs pour la réalisation de nouvelles sources laser solides. Leurs faibles seuils et leurs fortes efficacités laser ainsi que la possibilité d'obtenir des effets non-linéaires du troisième ordre ont stimulé une recherche intense dans le domaine des amplificateurs et des lasers miniaturisés à base de couches minces.

Dans ce travail de thèse, un procédé d'épithaxie en phase liquide (LPE) utilisant une trempe verticale de l'échantillon a été développé pour la réalisation de couches minces de KYW:RE sur des substrats de KYW non dopés. Cette étude a été menée avec deux solvants à base de tungstate $K_2W_2O_7$ et de chlorures NaCl-KCl-CsCl.

Le flux $K_2W_2O_7$ ne présente pas d'impureté ionique et est bien adapté à l'obtention du double tungstate KYW. Ce dernier est en effet la seule phase stable pouvant cristalliser à partir de la solution. Afin de former des couches d'épaisseur uniforme, la position et la vitesse de rotation du substrat ont été optimisées grâce à la simulation numérique de l'écoulement du liquide dans le creuset. La mise en œuvre d'un taux de cristallisation de $1,2 \text{ mg K}^{-1}\text{g}^{-1}$ avec une température de croissance de 900°C a donné lieu à des couches monocristallines sans défaut caractérisées par des épaisseurs pouvant dépasser $100 \mu\text{m}$ et par des taux de substitution RE/Y allant de 0,2 à 3 mol%. Une interface sans défaut a été obtenue en plongeant le substrat à 0,1-0,3 K au-dessus de la température de saturation. Des structures enterrées ont également été réalisées en déposant une couche supplémentaire de KYW non dopée.

Le point de fusion du solvant NaCl-KCl-CsCl étant situé à 480°C , des croissances épithaxiales ont pu être réalisées à des températures de 520°C , réduisant ainsi la formation de contraintes thermiques dans les couches fortement dopées par des ions de terres rares. Cependant, l'existence de phases parasites et la nucléation d'îlots 3D compliquent la formation de couches monocristallines et sans défaut ni fissure, ce qui impose une épaisseur maximum de l'ordre de $10 \mu\text{m}$.

Le concept original de l'épithaxie en micro-canaux (MCE) a ensuite été appliqué pour la première fois pour la réalisation de structures à largeur limitée sur KYW. Grâce à l'utilisation d'un masque d'or ou de platine avec des motifs rectilignes, des guides d'ondes rubans de KYW:RE présentant des largeurs de 40 à $200 \mu\text{m}$ et des hauteurs de 3 à $20 \mu\text{m}$ ont été réalisés sur un substrat de KYW à partir d'un flux de $K_2W_2O_7$.

Des caractérisations optiques ont été menées sur ces guides d'ondes rubans ainsi que sur les guides planaires de surface et enterrés. L'observation de la propagation de la lumière de lasers He-Ne à 633 nm ou de pompe (981 nm) a permis de mettre en évidence un très bon comportement du guidage passif (à 633 nm) et actif (pour la longueur d'onde de luminescence de l'ion Yb^{3+} à 1030 nm) avec de faibles pertes par propagation de 0,1-0,2 dB cm^{-1} .

L'obtention d'un effet laser en configuration continue (CW) a finalement été démontrée à 1025 nm pour les deux structures guidantes (planaires de surface et enterrée) à base de KYW:Yb. La puissance maximum de sortie et l'efficacité différentielle ont été respectivement mesurées à 290 mW et 80,4 %. D'après notre recherche bibliographique, ce dernier résultat correspond à la meilleure valeur jamais publiée pour un guide d'ondes laser en configuration planaire.

Contents

Abstract	I
Résumé	II
Contents.....	IV
1. Introduction	1
2. Rare-earth-ion (RE) doped KY(WO ₄) ₂ – a promising laser material	3
2.1. Properties of KY(WO ₄) ₂ crystals	3
2.1.1. Crystal structure	3
2.1.2. General physical and chemical properties	7
2.1.3. Optical properties	10
2.1.4. Single crystal growth	12
2.2. Active RE ³⁺ ions in the KY(WO ₄) ₂ host	15
2.2.1. Yb ³⁺ as an active ion	16
2.2.2. Other RE ³⁺ ions: Tb ³⁺ , Dy ³⁺ , Tm ³⁺ , and Er ³⁺	20
2.3. KY(WO ₄) ₂ :RE lasers.....	22
2.3.1. Overview of demonstrated KY(WO ₄) ₂ :RE lasers.....	22
2.3.2. Quasi-three-level laser model for KY(WO ₄) ₂ :Yb.....	24
3. Fundamentals of liquid-phase epitaxy (LPE)	29
3.1. Introduction to LPE	29
3.2. Phase diagrams	31
3.3. Nucleation and epitaxy	32
3.4. Growth modes	41
3.5. Growth rate	43
3.6. LPE techniques	47
4. LPE of the KY(WO ₄) ₂ :RE layers	51
4.1. State of the art in LPE of the KY(WO ₄) ₂ :RE layers	51
4.2. Substrate preparation	52
4.3. Experimental set-up	54
4.4. Choice of solvent	56
4.4.1. Properties of the K ₂ W ₂ O ₇ solvent	57
4.4.2. Properties of the NaCl–KCl–CsCl solvent	60

4.5.	LPE from the $K_2W_2O_7$ solvent	64
4.5.1.	Experimental conditions	64
4.5.2.	Growth mode	66
4.5.3.	Simulation of liquid flow	70
4.6.	LPE from the NaCl–KCl–CsCl solvent	74
4.6.1.	Experimental conditions	74
4.6.2.	Growth mode	75
4.7.	Microchannel epitaxy (MCE)	79
4.7.1.	Mask fabrication	81
4.7.2.	MCE of $KY(WO_4)_2:Yb$ ribs	83
5.	Characterization of the grown layers	87
5.1.	Orientation and crystallinity	87
5.2.	Composition	89
5.2.1.	Stoichiometry of the $KY(WO_4)_2$ matrix	89
5.2.2.	Incorporation of the RE^{3+} ions	91
5.3.	Comparison of layers grown from the $K_2W_2O_7$ and NaCl–KCl–CsCl solvents ..	93
6.	$KY(WO_4)_2:RE$ optical waveguides	95
6.1.	Theory of optical waveguides and waveguide lasers	95
6.2.	Surface and end-face polishing	100
6.3.	Waveguiding and beam profiles	104
6.4.	Loss measurements	107
6.5.	Planar waveguide laser based on $KY(WO_4)_2:Yb$	111
7.	Conclusions and Outlook	117
	References	119

Acknowledgements

List of Publications and Conference Contributions

Cirriculum Vitae

1. Introduction

Integrated optics is the technology of integrating various optical devices and components for generation, amplification, focusing, polarization, modulation, coupling, switching, and detection of light, all on a single substrate (chip). This concept, proposed as early as 1969 by S. E. Miller [mil69], is developing rapidly nowadays as an optical equivalent of electronic integrated circuits. Planar and channel waveguides are basic components of integrated optics, because they provide connections between the integrated components. Furthermore, when doped with active ions, waveguides can generate, amplify, and modulate visible and near-infrared signals. Miniature waveguide lasers and amplifiers are useful wherever size, weight, and material cost have to be considered, e.g., in optical communication and portable, airborne, or space equipment.

The primary objective of this work is to develop a production method for high-quality thin layers of $\text{KY}(\text{WO}_4)_2$ (hereafter KYW) doped with rare-earth (RE) ions employing liquid-phase epitaxy, and demonstrate their applicability as optical waveguides and waveguide lasers. The proposed work, however, is not limited only to growth and optical investigation of this specific material. It also assumes an exploration of liquid-phase epitaxy as a suitable method to fabricate complex functional structures, like buried, shaped, and channel waveguides, which are imperative for integrated optics.

Monoclinic KYW crystals doped with RE ions (hereafter KYW:RE) are recognized as relatively new, but very promising materials for solid-state lasers operating at room temperature, both in pulsed and continuous-wave mode [kul97, kule97]. Their low laser threshold, high efficiency, and third-order nonlinear effects stimulate research towards miniaturized lasers and amplifiers. Due to its high refractive indices on the order of 2.0, KYW is quite suitable for the fabrication of integrated optical devices.

Many RE ions incorporated into KYW exhibit very high absorption and emission cross-sections. In particular, the Yb^{3+} ion in KYW has an absorption maximum near 981 nm with a cross-section, for polarization parallel to the N_m principal optical axis, about 15 times larger than that of the well-established laser material $\text{Y}_3\text{Al}_5\text{O}_{12}:\text{Yb}$ (YAG:Yb). The short absorption length in highly-doped KYW:Yb together with an extremely small laser quantum defect as low as 1.6% [klo03] makes this material a favorable candidate for the thin-disk laser concept [bru02], where the active medium is a thin crystal or deposited layer. Moreover, the Yb^{3+} ion, which can be intensively excited with commercially available InGaAs laser diodes, is often used as an efficient sensitizer for other RE^{3+} ions, like Er^{3+} , Tm^{3+} , Ho^{3+} , or Pr^{3+} .

However, in Yb-doped lasers, a significant part (5% at room temperature in YAG:Yb [lac91]) of the total ground-state population is thermally excited in the lower Stark laser level. This laser scheme, often called the “quasi-three-level system”, gives rise to pronounced reabsorption and a rather high pump threshold. One way of decreasing the threshold is the use of a waveguiding structure in which high pump-power densities and excellent overlap of pump and resonator modes can be achieved. This approach requires fabrication of high-quality KYW:Yb layers on suitable substrates, and defect-free interfaces between the layer and the substrate to ensure low-loss propagation.

Liquid-phase epitaxy (LPE) is a suitable and reliable method for producing thin layers of different optical materials. In LPE, a single crystal layer can be grown from a dilute molten solution onto a flat, oriented single crystal substrate. Contrary to pulsed laser deposition (PLD) or ion implantation methods, LPE operates under near thermodynamic equilibrium conditions and allows high-quality single crystalline layers to be produced. Waveguide lasers based on LPE-grown layers of other materials, like YAG:Nd [han92] or YAG:Yb [pel95], normally exhibit low propagation losses on the order of 0.1 dB cm^{-1} and better laser performance than those fabricated with PLD or ion implantation.

This thesis work discusses the use of KYW:RE as a promising laser material, the LPE growth and characterization of KYW:RE layers, and, finally, applications of the grown layers as optical waveguides.

Chapter 2 starts with an overview of KYW properties: crystallography, physics, chemistry, and crystal growth. The following text is a description of RE ions selected as the active dopants for the KYW host. A survey of KYW:RE lasers reported in the literature concludes with a consideration of the quasi-three-level laser model which is an important prerequisite for understanding the behavior of KYW:Yb lasers.

In Chapter 3, the fundamentals of the LPE technique are presented and important experimental parameters, like supersaturation, substrate misorientation, and lattice misfit, are considered quantitatively with respect to the LPE of KYW:RE layers on KYW substrates.

Chapter 4 presents experimental results on the LPE of KYW:RE thin layers using two different solvents. The consideration of microchannel epitaxy is given in a separate subchapter because of the novelty and importance of the proposed approach. The characterization of the grown layers is given in Chapter 5.

Chapter 6 deals with the preparation and investigation of the grown layers as active and passive optical waveguides. A KYW:Yb planar waveguide laser, having a low laser threshold and the highest efficiency ever reported for an Yb-doped CW laser, is described.

Final conclusions of this work are given in Chapter 7.

2. Rare-earth-ion (RE) doped KY(WO₄)₂ – a promising laser material

Development of a new laser material requires the careful selection of active ions with the desired emission characteristics as well as thorough analysis of the physical and chemical properties of a suitable host. This chapter discusses the properties and growth methods of KYW single crystals which are considered as the host material. Then comes a description of the energy level schemes and laser potential of rare-earth ions selected as the active dopants for the KYW host. A special emphasis is made on the Yb³⁺ ion, because of its outstanding lasing properties. A survey of KYW:RE lasers reported in the literature is followed by a consideration of the quasi-three-level model, which is an important prerequisite for the investigation of KYW:Yb lasers.

2.1 Properties of KY(WO₄)₂ crystals

2.1.1 Crystal structure

KYW crystals belong to a large family of double tungstates with the general formula A^IT^{III}(WO₄)₂, where A is a monovalent alkali-metal cation (Li, Na, K, Rb, or Cs) and T is a trivalent metal or rare-earth cation (Al, Ga, In, Sc, Bi, Y, La or Ln=Ce...Lu). Together with the double molybdates, their crystal structure is related to that of Scheelite (CaWO₄), where Ca is substituted by the pair A^IT^{III}.

For the first time, the crystal structure of KYW was described by Borisov and Klevtsova in 1968 [bor68]. There are two polymorphic modifications of KYW with a phase transition temperature of 1010°C [kle68] or 1025°C [gal98]. The high-temperature β -modification has a tetragonal structure which is not stable at room temperature. The low-temperature α -KYW modification crystallizes in the monoclinic centrosymmetric space group *C2/c* or *I2/c* (*Z*=4) with unit cell parameters:

$$\begin{array}{llll}
 C2/c: & a = 1.064 \text{ nm}, & b = 1.035 \text{ nm}, & c = 0.754 \text{ nm}, & \beta = 130.50^\circ \\
 I2/c: & a^* = 0.805 \text{ nm}, & b^* = 1.035 \text{ nm}, & c^* = 0.754 \text{ nm}, & \beta^* = 94.0^\circ
 \end{array}$$

Both space groups belong to the $2/m$ point group and have Schönflies notation C_{2h}^6 , i.e. they describe the same crystal structure but use different setting coordinates for a monoclinic unit cell. The connection of basis vectors for both settings is shown in Fig. 2.1. The second $I2/c$ setting is more attractive because its parameters, including the monoclinic angle $\beta \approx 94^\circ$, correlate better with the morphology of grown KYW crystals. This simplifies significantly the orientation and cutting of the crystals. However, the $C2/c$ group is recommended by the International Crystallographic Union as the standard setting, and this setting was used in many previous works on optical properties of KYW materials. Thus, the $C2/c$ notation is employed hereafter in the text for the crystallographic descriptions.

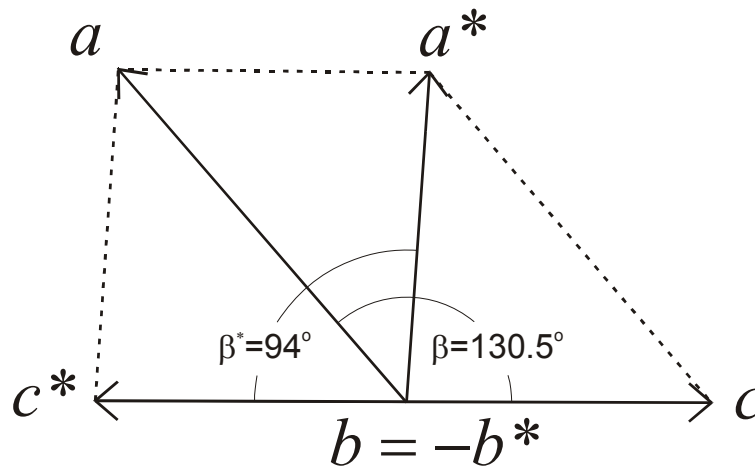


Fig. 2.1. Orientation of crystallographic axes of the KYW crystal structure according to the $C2/c$ space group (without asterisk) and the $I2/c$ space group (with asterisk).

A projection of the α -KYW crystal structure along the b -axis together with the nearest coordination of the Y ions is shown in Fig. 2.2. There are three different types of coordination polyhedrons in the α -KYW structure.

The tungsten and oxygen atoms occupy general $8f$ Wyckoff positions, forming coordinated polyhedrons of C_1 symmetry, which can be presented as highly distorted octahedrons. Two WO_6 octahedrons are joined by sharing edges O...O (double oxygen bridge) in the W_2O_{12} unit. These units form a double chain along the crystallographic c -axis by sharing vertex O.

Eight oxygen atoms, forming a square antiprism, coordinate the yttrium atom. The polyhedrons form a single chain in the $[101]$ direction. The Y–Y distance in the same chain is 0.406(3) nm, and between different chains it is 0.604(2) nm [kry02]. These separations are very important for energy-transfer processes between active trivalent ions substituting for the yttrium ion.

The alkali cation K^+ occupies the specific $4e$ Wyckoff position. Its coordination consists of twelve oxygens forming a distorted icosahedron. These polyhedrons form chains with shared edges.

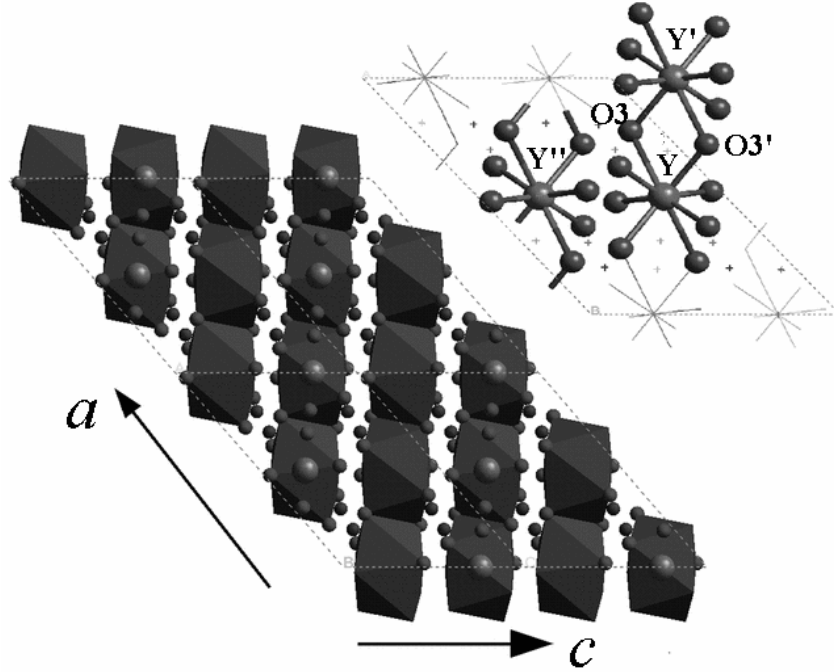


Fig. 2.2. Projection of the KYW crystal structure along the $[010]$ direction and coordination polyhedra of yttrium ions [puj01].

KYW has a crystalline habit that is formed mainly by the $\{110\}$, $\{\bar{1}11\}$, $\{010\}$, and $\{310\}$ faces, as is shown on the morphological sketch of a typical KYW crystal grown by top-seeded solution growth (TSSG) (Fig. 2.3). The appearance/absence of particular faces in the habit can be explained from the Hartman-Perdok theory about periodic bond chains (PBCs). Each chemical bond between the atoms can be presented as a segment of the line joining the atoms, assuming that the segment length is proportional to the binding energy. All segments of a specific length oriented along the same crystallographic direction form the periodic chains in the crystal. The chains differ by their orientations and also by their strength, i.e. stronger chains have shorter segments, and, respectively, stronger chemical bonds along the chain. The PBC theory postulates that only faces that are parallel to at least two systems of the shortest PBCs appear on real crystals. There are four shortest PBCs in the KYW crystal structure, which coincide with the crystallographic directions $[110]$, $[001]$, $[112]$, or $[101]$. Thus, the most developed faces $\{110\}$ and $\{\bar{1}11\}$ are parallel to three selected PBCs, and the $\{010\}$ face is parallel to two PBCs. $\{310\}$, $\{\bar{1}10\}$, and $\{100\}$ are parallel to one PBC, which agrees with the fact that these faces are less developed or not observed at all.

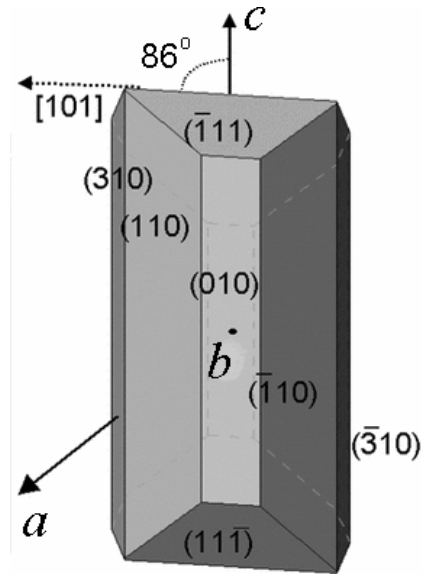


Fig. 2.3. Morphology of a KYW crystal grown by TSSG [azn04].

The stable crystal faces represent the slowest growth directions, and the absence of a face indicates a fast growing direction. The fast growing direction for KYW are $[101]$ and $[001]$. Indeed, when using (101) or (001) -oriented seeds for the TSSG of KYW, the growth rates are higher than for (010) -oriented seeds. The high growth rates can provoke the formation of macrodefects, e.g. inclusions. Therefore, (010) -, i.e. b -oriented seeds are preferred for the growth of high-quality bulk KYW crystals, and hence, b -orientation is the most favorable to achieve a stable growth on the crystal face.

Obviously, the crystal habit depends not only on the crystal structure, but also on growth conditions, like temperature, supersaturation, and growth medium. For instance, Métrat *et al.* reported about prismatic and pyramidal KYW crystals grown by the top-nucleated floating crystal method (TNFC) [met99]. They observed $\{010\}$, $\{\bar{1}11\}$, $\{122\}$, $\{\bar{3}11\}$, and $\{\bar{2}\bar{1}2\}$ faces on the habit, which gave rise to some discrepancy between the proposed lattice symmetry and the grown crystal forms. The polyhedral habit of many high-quality bulk crystals of monoclinic tungstates grown in several laboratories located in Russia (e.g. [pav97]) included mainly $\{110\}$ and $\{\bar{1}11\}$ prisms, as well as, $\{010\}$, $\{100\}$, and $\{101\}$ pinakoids.

Natural edges of the KYW crystal coincide with the c -axis and $[101]$ direction, and form a characteristic angle of 86° . The presence of this characteristic angle allows easy determination of the crystallographic directions with respect to the crystal edges and considerably simplifies orientation and cutting of KYW crystals.

2.1.2 General physical and chemical properties

The KYW compound is formed in the K_2O – Y_2O_3 – WO_3 ternary system investigated in detail by Gallucci *et al.* [gal98]. Projection of the liquidus surface in the WO_3 -rich corner of the system is shown in Fig. 2.4.

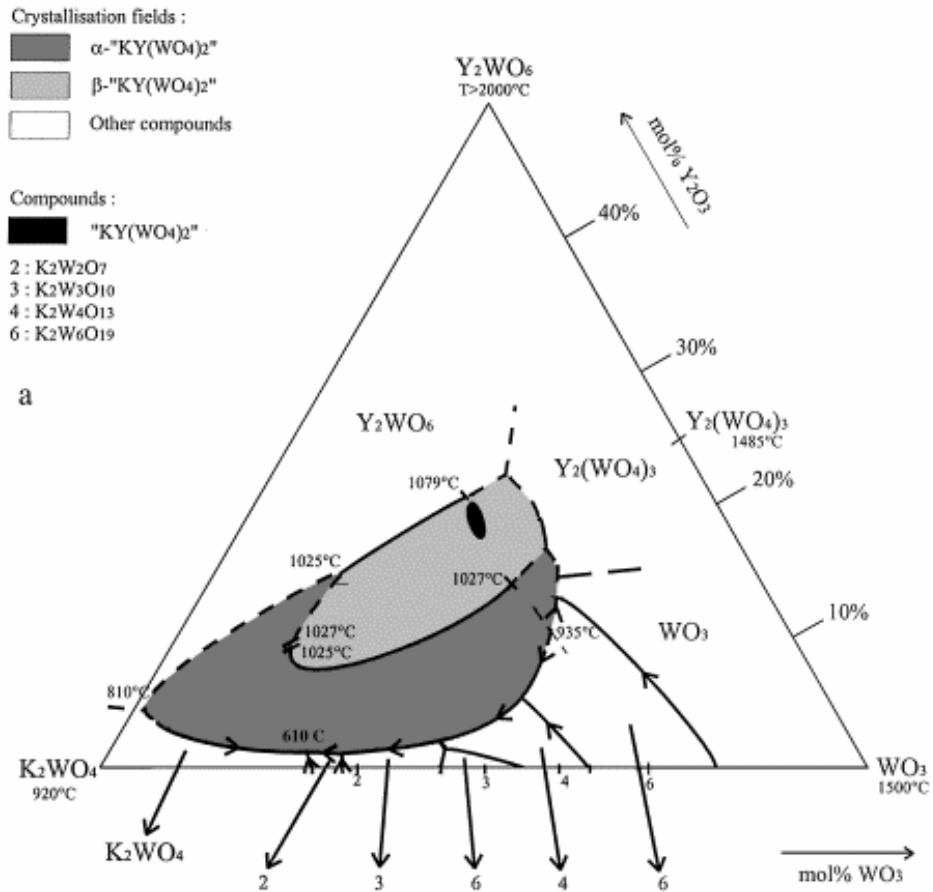


Fig. 2.4. Projection of the liquidus surface of the K_2WO_4 - Y_2WO_6 - WO_3 system [gal00].

The liquidus surface consists of crystallization fields of several ternary phases (Y_2WO_6 , $Y_2(WO_4)_2$, K_2WO_4 , $K_2W_2O_7$, $K_2W_3O_{10}$, $K_2W_4O_{13}$, and $K_2W_6O_{19}$), and two polymorphous modifications of the only KYW quaternary phase. The β -KYW modification has a melting point of 1079°C [gal98], 1080°C [kam02], or 1050°C [kle68]. Temperature of the $\beta \leftrightarrow \alpha$ phase transition is between 1027°C and 1025°C, depending on the composition of solidified alloy [gal98]. According to [kle68], the phase transformation temperature is constant and equals 1010°C.

When investigating the binary $K_2W_2O_{13}$ - Y_2O_3 section, it was found that KYW is not a stoichiometric phase [gal98, gal00]. The congruent melting was observed for composition $KY_{1.173}(WO_4)_2$ (excess of Y_2O_3 as compared to $KY(WO_4)_2$), and a solid solution range of

about 2 mol% was delimited around that composition. Later, Gallucci *et al.* investigated the non-stoichiometric nature of KYW by neutron diffraction [galu00]. Nevertheless, it was concluded that the non-stoichiometry of KYW should have no incidence on the laser properties of the KYW:RE crystals because the RE³⁺ ions occupy only the Y³⁺ regular sites.

Table 2.1. Some physical properties of the α -KYW single crystals [kam01].

Melting point	1080°C
Phase transition	1025°C
Density	6.565 g cm ⁻³
Specific heat	500 J kg ⁻¹ K ⁻¹
Thermal conductivity	3.3 W m ⁻¹ K ⁻¹
Thermal expansion coefficient	[100] 11.0×10 ⁻⁶ K ⁻¹ [010] 1.9×10 ⁻⁶ K ⁻¹ [001] 17.8×10 ⁻⁶ K ⁻¹
Mohs' hardness	4.5-5
Optical classification	Biaxial
Optical transparency	0.35-5.5 μ m
Band gap	3.83 eV
Stimulated Raman Scattering (SRS) active vibration modes	$\omega_{R1} = 905$ cm ⁻¹ $\omega_{R2} = 765$ cm ⁻¹ $\omega_{R3} \approx 87$ cm ⁻¹
Steady-state Raman gain coefficient	3.6 for ω_{R1} and ω_{R2}

The density of KYW measured by the bottle method is 6.565 g cm⁻³ [kam01]. This is lower than the theoretical density of 6.61 g cm⁻³ calculated from the KYW unit cell parameters [kle68]. The KYW crystals possess a hardness of 4.5-5 according to the Mohs' scale [kam01], i.e. they can be scratched with a steel knife. The crystals are quite brittle, however, no pronounced cleavage planes have been reported. Some physical properties of the α -KYW crystals are given in Table 2.1.

The thermal conductivity of KYW crystals, averaged over three directions, is 3.3 W m⁻¹ K⁻¹, which is approximately four times that of a typical phosphate laser glass [klo03]. High thermal conductivity is a desired property for laser materials because it provides efficient heat removal and cooling of the active laser zone. The linear thermal expansion of KYW was investigated by powder X-ray diffraction in a temperature range of 25-500°C

[Puj99]. The linear thermal expansion coefficients of KYW along three crystallographic directions are given in Table 2.1. The thermal dilatation is maximal along the [001] direction. The positions of the principal expansion axes with respect to the crystallographic axes are shown in Fig. 2.5 as the thermal expansion ellipsoid of KYW. Here, X'_3 is the principal axis with the maximum thermal expansion, and X'_1 is the axis with the minimum thermal expansion.

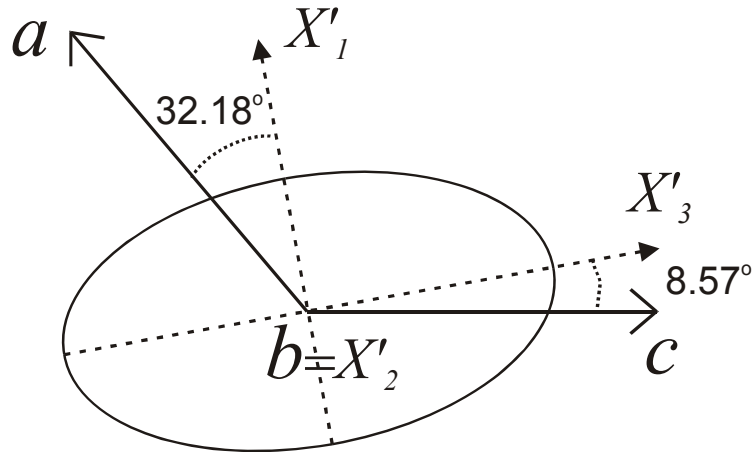
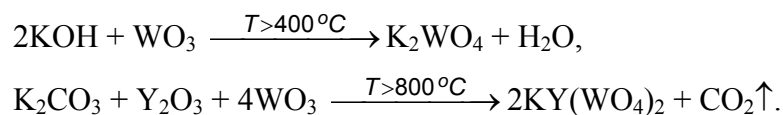
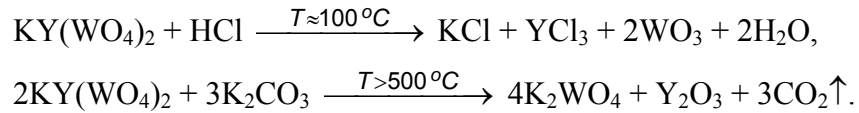


Fig. 2.5. Thermal expansion ellipsoid of KYW.

Data on chemical properties of KYW are practically absent in the literature. It is widely accepted that KYW is non-hygroscopic, chemically inert and stable against different reactive media. The compound can be considered as a mixed potassium-yttrium salt of weak wolframate acid $[H_2WO_4]$, which can be extracted neither in free state nor in water solutions. The respective acid anhydrite WO_3 exhibits its acid nature only when fused with bases or basic oxides:



In all tungstates, the tungsten has the oxidation state 6+. Since it is the highest possible oxidation state for group VI-B elements of the Periodic Table, oxidation properties of W^{6+} manifest themselves solely with the strongest reducing agents, like atomic hydrogen. More typical are exchange reactions at elevated temperatures:



The solubility of KYW in water is small, presumably below the solubility of CaWO_4 , which is 0.64 mg per 100 g H_2O [crc00].

2.1.3 Optical properties

Optical properties of monoclinic crystals are related to their crystallographic anisotropy. Monoclinic α -KYW is a biaxial crystal, whose optical properties are described by the $2/m$ point group.

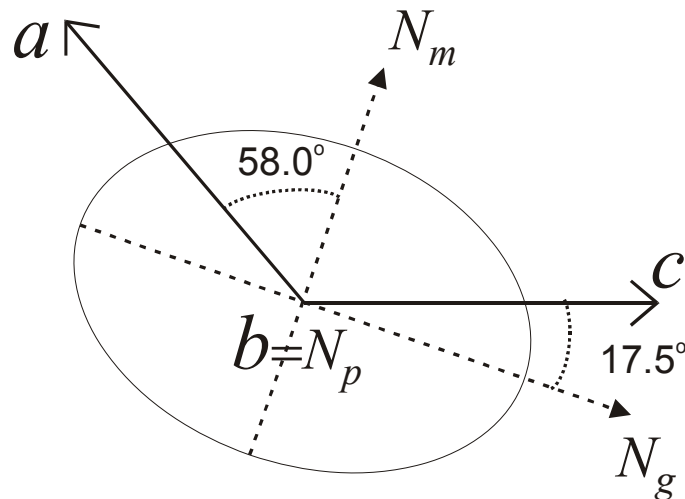


Fig. 2.6. Optical ellipsoid of KYW.

One of the principal optical axes is parallel to the b -crystallographic axis and is labeled as N_p . The two other principal optical directions are in the ac crystallographic plane. The respective optical ellipsoid is shown in Fig. 2.6. Here, N_g is the traditional labeling of an optical direction with the highest refractive index n_g of the optical indicatrix, N_m has the intermediate refractive index n_m , and N_p has the smallest refractive index n_p exactly along the $[010]$ direction of the monoclinic crystal. All the refractive indices of KYW can be approximated by the single-term Sellmeier dispersion formula [kam01]:

$$n_i^2(\lambda) - 1 = K_i \lambda^2 / (\lambda^2 - \lambda_i^2). \quad (2.1)$$

Here K_i and λ_i are the Sellmeier coefficients for $i = g, m, \text{ or } p$, and λ is the wavelength of the incident beam. The K_i and λ_i values for the principal optical directions are listed in Table 2.2.

Table 2.2. Values of K_i and λ_i used in the dispersion equation (2.1) for calculation of the principal refractive indices n_g , n_m , and n_p of KYW at room temperature [kam01].

n_i	K_i	λ_i (μm)
n_g	3.1278346	0.161512
n_m	2.9568303	0.1591855
n_p	2.8134935	0.1529056

Fig. 2.7 shows the dispersion of the refractive indices within the wavelength range of 0.4–1.1 μm at room temperature.

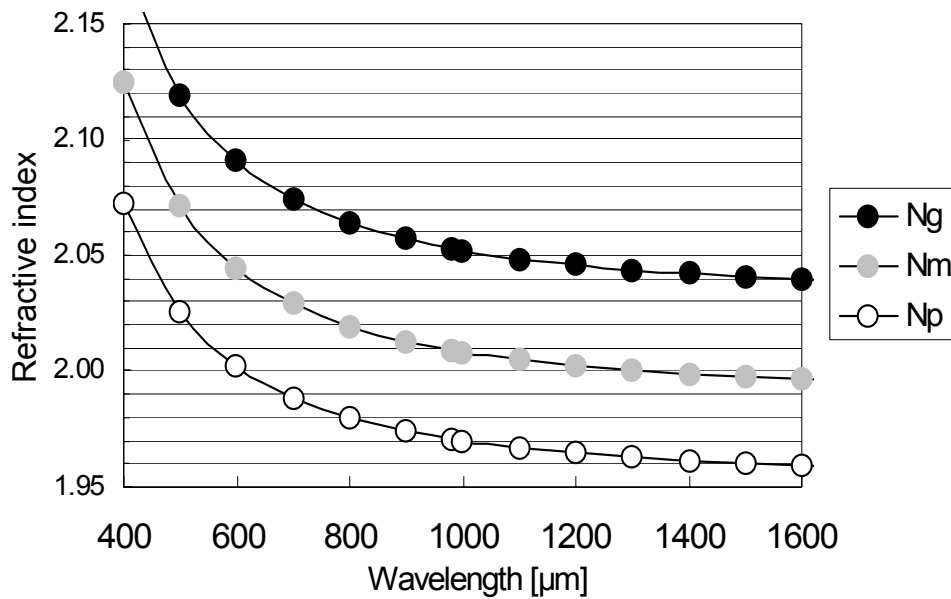


Fig. 2.7. Wavelength dependence of the refractive indices of KYW along the principal optical directions.

The main optical properties of KYW single crystals are listed in Table 2.1. The UV cutoff wavelength of KYW is near 320 nm ($31\,250\text{ cm}^{-1}$), which corresponds to an optical band gap of 3.83 eV. The transparency window of KYW crystals extends up to 5.5 μm . The monoclinic tungstate has large nonlinear optical susceptibilities $\chi^{(3)}$, and, therefore, can be used in various laser experiments and applications based on the stimulated Raman scattering phenomena

(SRS). In KYW, two SRS-active modes with $\omega_{R1} = 905 \text{ cm}^{-1}$ and $\omega_{R1} = 765 \text{ cm}^{-1}$ are explained by internal W–O vibrations in edge-sharing W-octahedra [kam01].

2.1.4 Crystal growth

As mentioned in Section 2.1.2, the KYW phase undergoes a polymorphic structural transformation at 1025°C. Therefore, the monoclinic α -KYW crystals cannot be grown from the stoichiometric melt using the conventional Czochralski technique because of the structural decomposition of single KYW crystals upon the polymorphic transformation. However, the crystal growth is possible from high-temperature solutions at growth temperatures below the phase transition. Three solution-based techniques to produce bulk undoped and RE-doped KYW crystals have been reported. The growth techniques are listed in the order of their relevance and of expected crystalline quality:

- top-seeded solution growth (TSSG);
- induced nucleated floating crystal (INFC) growth;
- vertical Bridgman-Stockbarger method.

TSSG is the most important method used for the production of laser-grade KYW:RE crystals. It is often called “modified Czochralski” method [kul97, kam01], because the only difference from the conventional Czochralski method is that an appropriate solution is employed instead of the stoichiometric melt. In TSSG, a seed crystal is put in contact with the saturated solution and a bulk crystal is grown onto the seed from the supersaturated solution while the system temperature is slowly decreased. Potassium tungstates, K_2WO_4 and $\text{K}_2\text{W}_2\text{O}_7$, have been employed as suitable solvents for KYW because they contain no ions other than those required for the crystal growth and high growth rates are possible. The properties of the tungstate solvents are discussed in detail in Section 4.4.1.

As the first step of TSSG, the solution components, which are high-purity powders of K_2CO_3 , Y_2O_3 , WO_3 , and RE_2O_3 (dopant), are mixed to obtain a homogeneous mixture. The mixture composition corresponds to the KYW concentration of 10-50 mol% in the K_2WO_4 or $\text{K}_2\text{W}_2\text{O}_7$ solvent. The powder is heated in a platinum crucible to a maximum temperature, which is normally 50 K above the expected saturation temperature. The solution is homogenized for several hours or even days [wan90, wan92, tu94, han02], and then slowly cooled down to the saturation temperature. A seed crystal of KYW is put in contact with the saturated solution. Often, the seed crystal is immersed into the solution already above the saturation point to dissolve the outer surface of the seed and to ensure a defect-free nucleation

[wan90, wan92]. Pujol *et al.* showed that *b*-oriented seeds appear to be the most suitable for the growth of monoclinic tungstate crystals with minimum number of defects [pujo99]. Other orientations result in an increased number of defects, like solvent or gas bubbles.

Table 2.3. Some examples of TSSG for KYW:RE crystals, reported in the literature.

Crystal	Solvent	Solute conc. [mol%]	Saturation temp. [°C]	Cooling rate [K h ⁻¹]	Crystal dimensions [mm ³]	Reference
KYW:Nd	K ₂ WO ₄	50	-	0.08	55×35×17	[wan90]
KYW:Er,Yb	K ₂ WO ₄	20	≈ 900	0.08-0.16	76×66×32	[wan92]
KYW:Er,Nd	K ₂ WO ₄	45	1010	0.08-0.12	45 mm long	[tu94]
KYW:Er,Yb	K ₂ WO ₄ +KF	41.4	960	0.04	30×23×15	[han02]
KYW:Yb	K ₂ W ₂ O ₇	-	< 1000	0.05	10×15×40	[kule97]
KYW:Yb	K ₂ W ₂ O ₇	-	900-1000	0.05-0.08	80 mm long	[dem00]
KYW:Dy	K ₂ W ₂ O ₇	-	< 1000	-	50 cm ³	[kam02]
KYW:Yb	K ₂ W ₂ O ₇	12	920	0.05	5×5×8	[azn04]

Once the seed is in the solution, the system temperature is slowly decreased at a rate of 0.05-0.16 K h⁻¹ to maintain the necessary supersaturation. A small axial temperature gradient of 0.5-1 K cm⁻¹ is often used to keep the crucible bottom hotter and to avoid the crystallization of parasitic KYW crystals. To ensure efficient solution mixing and stable growth rates for all crystal faces, the seed is rotating around its vertical *b*-axis at a rate of 4.5 rpm [wan90, wan92, tu94, han02], 40 rpm [azn04] or even 50-90 rpm [kam02]. Often, the growing crystal is also slowly (0.2 mm h⁻¹) pulled from the solution, as it were the conventional Czochralski method [kam02].

After the growth, which takes from 5 [azn04] to 30 days [tu94], the crystal is drawn out from the melt and cooled down slowly to room temperature to avoid thermal shocks. Depending on the initial charge mass, the crucible volume, and the growth time, crystals of different sizes can be obtained. The maximum length of a KYW:Yb crystal was reported to be 80 mm [dem00]. By using large solution mass and pulling the seed, larger crystals should be accessible. In particular, Pavlyuk *et al.* grew crystals of another double tungstate, KGdW:Nd, up to 120 mm long and weighing up to 3 kg [pav97].

The INFC method was employed for the first time by Métrat *et al.* to grow KYW:Nd [met97] or KYW:Yb [met99] crystals. Contrary to classical growth methods (Czochralski, TSSG, Kyropoulos), no crystal seed was used. The seed was created on the melt surface by controlled local transient supersaturation. As for the rest, the preparation procedure for INFC was similar to that described above for TSSG. Oxide powders were mixed in a platinum crucible to form a solution with 63 mol% of KWO_4 and 37 mol% of KYW:Yb/Nd. The seed crystals were nucleated on the surface of the supersaturated solution that was kept at a constant temperature of 925°C . During early stages of the growth, the small crystals floated freely on the melt surface. When they became too heavy, they had to be kept up by a pumping device to avoid sinking. After one day of growth, relatively large (up to $13 \times 13 \times 5 \text{ mm}^3$) crystals were produced, giving rise to a high linear growth rate of 0.5 mm h^{-1} . As-grown crystals had a platelet or pyramidal shape. Several inclusions of the mother liquid were observed in the grown platelets, otherwise the crystal quality was good enough for optical investigations. The identification of crystal face indices revealed some discrepancy between the monoclinic lattice symmetry and the crystal forms. However, that discrepancy has been confirmed in no further investigations.

Applicability of the vertical Bridgman-Stockbarger method for the KYW:RE crystal growth was examined in the works of Galucci *et al.* [gal00, gal01]. This method is based on the progressive crystallization of compound by lowering a growth container in a vertical furnace with decreasing temperature gradient. K_2WO_4 was used as an appropriate solvent and the solution composition was chosen from the field of primary crystallization of KYW. The charge contained in a platinum crucible was placed into a vertical furnace at the maximum temperature of 950°C . After melting and homogenizing the liquid, the crucible was lowered slowly inside the furnace towards the colder bottom (between 0.4 and 2°C h^{-1}) to complete the solution crystallization. The solidified charge was cooled to room temperature and cut into sections with a diamond wheel in order to extract raw crystals. A final shaping work using soft polishing was needed to clean the crystals from the solidified solvent and to remove superficial defects induced by the crystal extraction from the crucible. As-grown crystals had maximum dimensions of $7 \times 5 \times 4 \text{ mm}^3$ and a relatively poor crystalline habit without any developed natural faces.

There was also an attempt to produce monoclinic KYW crystals using the laser heated pedestal growth (LHPG) [gal98]. However, only polyphased fibers containing $\text{Y}_2(\text{WO}_4)_3$ and Y_2WO_6 were obtained from an initial charge having the theoretical stoichiometry $\text{KY}(\text{WO}_4)_2$.

2.2 Active RE^{3+} ions in the KYW host

Since their first synthesis by Van Uitert and Soden in 1961 [uit61], KYW crystals have been widely used as a suitable host material for most RE ions, where the RE^{3+} ion substitutes for the Y^{3+} ion, for various spectroscopic and laser applications. Due to similar ionic radii of the Y^{3+} and RE^{3+} ions, KREW crystals, where RE = Sm, Eu, Gd, Tb, Dy, Ho, Er, Tm, Yb, and Lu, have the same monoclinic structure and space group $C2/c$ as KYW [kle69]. Thus, the formation of continuous solid solutions between KYW and KREW is possible, and doping concentrations of RE in KYW can be as high as 100 mol% with respect to Y. This results in the formation of stoichiometric laser materials, e.g. KYbW [puj02] or KErW [kam83], which possess very short absorption lengths and unique laser properties.

The other KREW compounds, where RE = La, Ce, Pr, Nd, and Pm, crystallize in the tetragonal Scheelite structure. The tetragonal unit cell is different from the monoclinic KYW cell because the ionic radii for the above RE^{3+} ions are considerably larger than the Y^{3+} radius. However, doping concentrations of up to 5 mol% are still possible for these RE^{3+} ions without changing the monoclinic KYW symmetry.

The RE^{3+} ion enters the KYW structure in a crystallographic site of the Y^{3+} ion with the C_2 point symmetry. Eight oxygens forming a square antiprism coordinate the RE^{3+} ion. Although the KYW unit cell contains four formula units, the oxygen polyhedrons around the RE^{3+} ions differ only by their orientation in space. Therefore, in the absence of any external perturbations, all ions of the RE element should have the same crystal field and energy level spectrum in the KYW matrix.

Transitions between the $4f$ electronic levels are responsible for the optical properties of the RE^{3+} ions. The energy level schemes for some RE^{3+} ions in the KYW host are shown in Fig. 2.8, together with the indication of possible laser $4f-4f$ transitions. Generally, the positions of energy levels for the trivalent RE ions in KYW do not differ significantly from those in other oxide crystals [die63] because of the electronic shielding of the $4f$ sub-shell by the outer $5s$ and $5p$ sub-shells. The RE-doped KYW crystals have colors that are characteristic for RE-doped oxides: with Ce – greenish shade, Pr – green, Nd – lilac, Sm – yellow, Tb – light brown, Dy – light green, Ho – greenish-yellow, Er – rose, with La, Eu, Gd, Yb, and Lu the crystals are practically colorless [kle69].

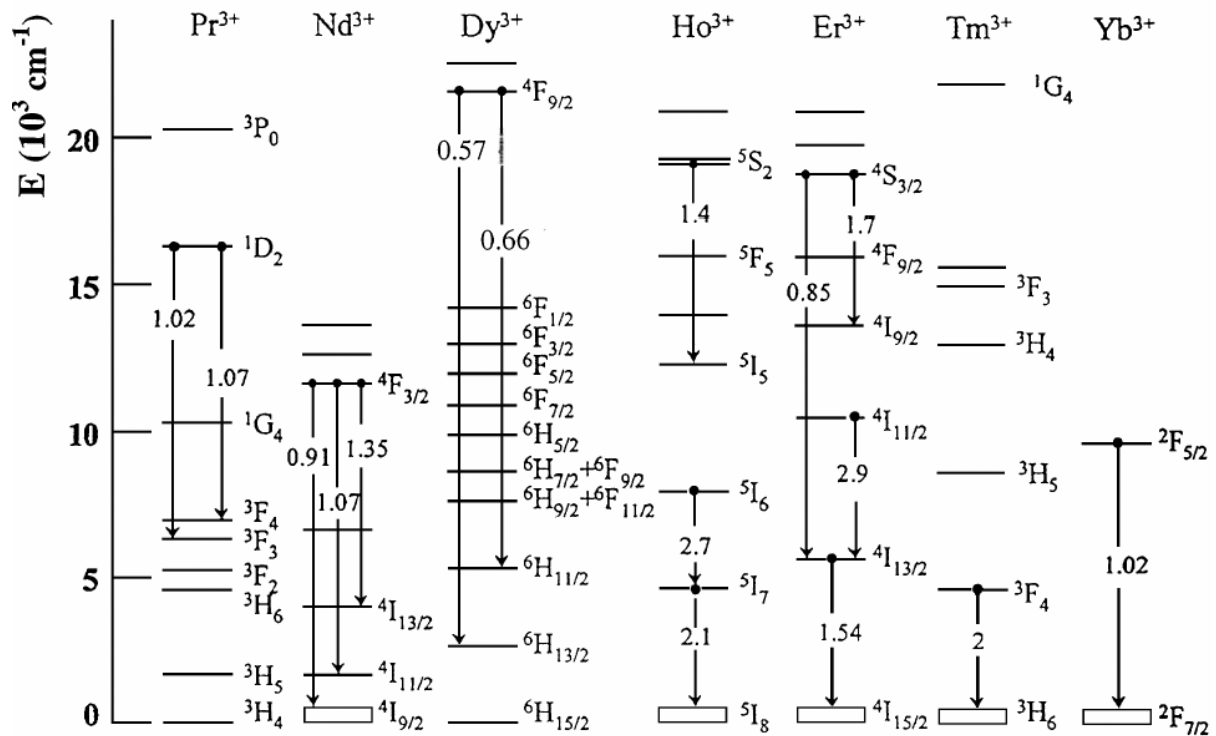


Fig. 2.8. Energy levels of selected RE³⁺ ions used as active dopants for the KYW crystals. Possible laser transitions are indicated with arrows and numbers indicate the transition wavelengths in μm [kam02].

2.2.1 Yb³⁺ as an active ion

Energy level scheme

The Yb³⁺ ion has the electronic configuration $[\text{Xe}] 4f^{13}$, i.e., it lacks one electron to complete the $4f$ shell. The ground-state level can be found according to Hund's selection rules: the total electron-spin number S and the total orbital angular number L should be maximal; the total angular number $J = |L - S|$ for shells less than half filled, while $J = L + S$ for shells that are more than half filled. Thus, the Yb³⁺ ground state has $S = 1/2$ and $(2S+1) = 2$, $L = 3$, and $J = 3 + 1/2 = 7/2$, which corresponds to the spectroscopic term $2\text{F}_{7/2}$. The only excited state, $2\text{F}_{5/2}$, has the same multiplicity and orbital momentum and differs only by the angular momentum $J = 3 - 1/2 = 5/2$. The energy-level scheme of the Yb³⁺ in the KYW host is shown in Fig. 2.9.

The two energy states, $2\text{F}_{5/2}$ and $2\text{F}_{7/2}$, are split due to the crystal field of the ligands. In ions with an odd number of electrons like Yb³⁺ at least twofold degeneracy remains (Kramer's theorem), and $(J + 1/2)$ Stark sub-levels are generated: three and four Stark sub-levels for the $2\text{F}_{5/2}$ and $2\text{F}_{7/2}$ states, respectively.

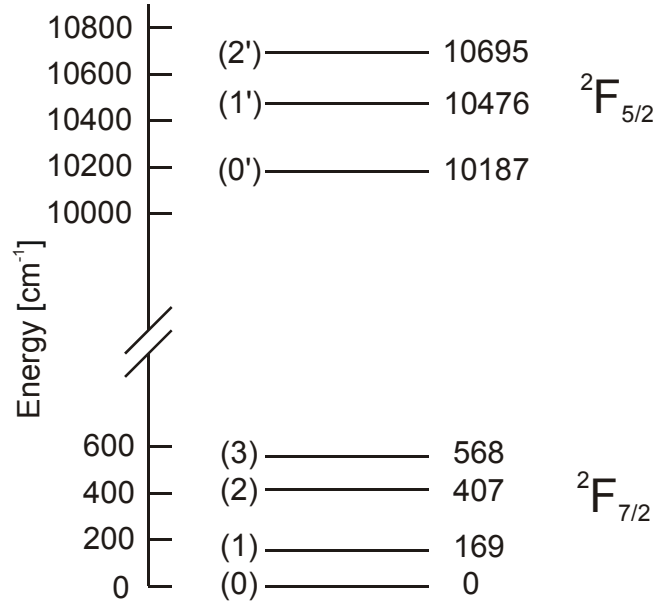


Fig. 2.9. Energy level scheme of the Yb³⁺ ion in the KYW host [kule97].

The Stark splitting is only a few hundreds cm⁻¹ and the partial population f within a Stark multiplet obeys the Boltzmann distribution

$$f_i = \frac{\exp[(E_1 - E_i)/(k_b T)]}{\sum_i \{\exp[(E_1 - E_i)/(k_b T)]\}} \quad (2.2)$$

Here, E_1 and E_i are the energies of the lowest and upper sub-levels, T is the temperature, and k_b is the Boltzmann constant. At $T = 300$ K, the partial populations of the ground ${}^2F_{7/2}$ state are 60.5%, 26.9%, 8.6%, and 4.0% for sub-levels (0), (1), (2), and (3), respectively. The partial populations of the excited ${}^2F_{5/2}$ state are 74.8%, 18.7%, and 6.5% for sub-levels (0'), (1'), and (2'), respectively.

Absorption and emission

The absorption and emission of the KYW:Yb crystals are very polarization dependent because of the pronounced anisotropy of the KYW crystal. Effective absorption and emission cross-sections are given in Fig. 2.10 for polarizations parallel to the crystallographic axes in the $I2/c$ setting. A strong absorption line is observed at 981.2 nm for the $E // a^*$ polarization, with a linewidth (FWHM) of 3.5 nm at room temperature. The peak cross-section of ground-state absorption (GSA), σ_{GSA} , is 1.33×10^{-19} cm² at 981.2 nm for $E // a^*$ [kule97]. It is 15 times higher than the absorption cross-section of the well-established laser material Yb:YAG. At 981 nm, $\sigma_{\text{GSA}} \approx 3.35 \times 10^{-20}$ cm² for $E // b^*$ and $\sigma_{\text{GSA}} \approx 2.1 \times 10^{-20}$ cm² for $E // c^*$. The ratio

between the absorption cross-sections is 6.3 : 1.6 : 1 for the E polarization parallel to a^* : b^* : c^* , respectively. The effective cross-sections values depend only on the propagation direction and are minimally influenced by different doping levels. Therefore, these values are comparable with those obtained for the stoichiometric KYbW crystal, 7.0 : 1.3 : 1 for N_m : N_p : N_g , respectively [puj02], because the crystallographic axes in the $I2/c$ setting almost coincide with the directions of the optical indicatrix (Fig. 2.1 and 2.6).

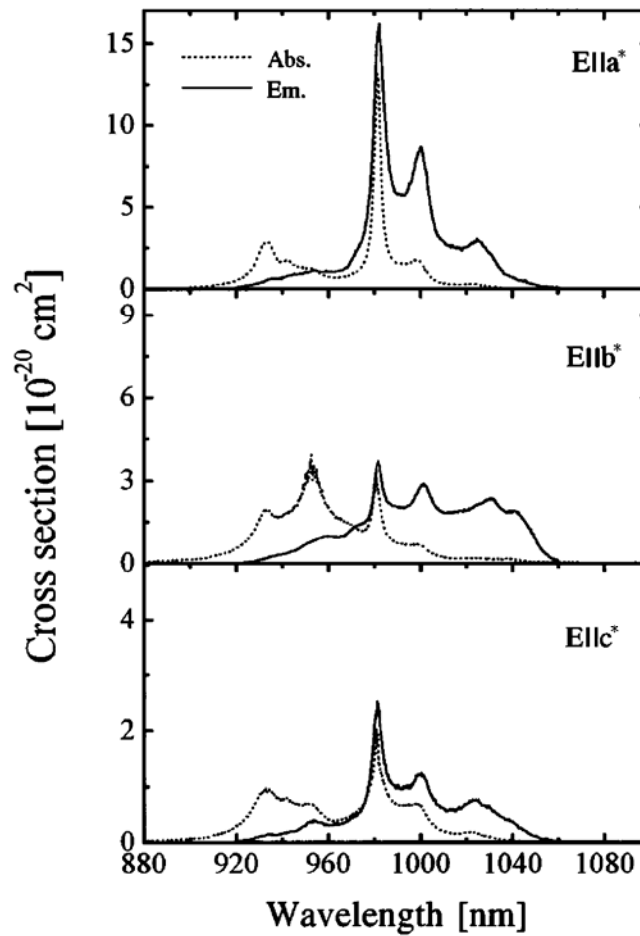


Fig. 2.10. Room-temperature polarized absorption and emission spectra of KYW:Yb [kule97].

The stimulated emission cross-sections were calculated using the reciprocity method [del93]. From an absorption cross-section value σ_{GSA} , one can readily obtain a respective stimulated-emission cross-section as follows:

$$\sigma_{\text{SE}}(\nu) = \sigma_{\text{GSA}}(\nu) \frac{Z_g}{Z_e} \exp\left[\frac{(E_{z_l} - h\nu)/kT}{kT}\right]. \quad (2.3)$$

Here, Z_g and Z_e are the partition functions of the ground state (g) and the excited state (e) respectively, E_{z_l} is the energy of the zero line (energy gap between the lower Stark sub-levels

(0) and (0')), and σ_{SE} is the stimulated emission cross-section at the wave frequency ν . The partition functions are simply equal to degeneracies, d_k , of the two states at high temperatures

$$Z_k = \sum_k d_k \exp(-E_k / kT). \quad (2.4)$$

For the energy level structure of Yb^{3+} in KYW, the ratio of the partition functions $Z_g / Z_e = 1.24$. The calculated peak stimulated-emission cross-section is also maximum for the $E // N_m$ polarization and it equals $3.0 \times 10^{-20} \text{ cm}^2$ at 1025 nm.

Fluorescence lifetime

The fluorescence lifetime of the Yb^{3+} excited state in KYW has been measured in many works for different Yb concentrations: 0.85 ms for 5 mol% Yb:KYW [kul97], 0.6 ms for 5 mol% Yb:KYW [kule97], 0.3 ms for 1 mol% Yb:KYW [dem00], 0.240 ms for 10mol% Yb:KYW, 0.233 ms for 10 mol% Yb:KYW [kis04], 0.232 ms for 0.2 mol% Yb:KYW [pet05], and 0.2 ms for KYbW [puj02]. The large spread of values found in literature can be explained by the fact that measurements of the intrinsic fluorescence Yb^{3+} lifetime are complicated by the following phenomena [bou03]:

- at low Yb^{3+} concentrations (up to 1-5 mol%), radiative energy transfer between the Yb^{3+} ions, which is called *self-trapping*, increases the measured fluorescence lifetime;
- at elevated Yb^{3+} concentrations (5-100 mol%), traces of other RE ions, like Er^{3+} or Tm^{3+} , decrease the detected IR fluorescence lifetime of Yb^{3+} because of fast non-radiative energy migration to the impurity ions with the subsequent emission of visible fluorescence;
- total internal reflection (TIR) can prolong the lifetime measured for bulk crystals.

Using 0.2 mol% Yb:KYW crystals in the form of fine powders immersed in a refractive-index-matching fluid (e.g. ethyleneglycol), the fluorescence lifetime of Yb^{3+} was reliably measured to be 0.232 ms [pet05].

Laser potential of KYW:Yb

Summarizing the properties of the Yb^{3+} ion in the KYW host, one can list its main advantages for laser applications:

- simple two-level electronic structure avoids undesired loss processes such as excited-state absorption (ESA) and energy-transfer upconversion (ETU);

- high absorption cross-section allows for efficient pumping with commercially available InGaAs laser diodes around 980 nm;
- broad spectral emission band allows tuning over the 1020-1075 nm range and generation of ultrashort laser pulses;
- small Stokes shift between absorption and emission wavelengths (laser quantum defect) reduces heat generation and thermal load of a lasing KYW:Yb crystal.
- relatively long lifetime of 0.232 ms favors an efficient energy storage of the laser.

On the other hand, a problem of Yb^{3+} as a laser ion is that a significant part (4% at room temperature) of the total ground-state population is thermally excited in the upper Stark sublevel which is the lower laser level, giving rise to pronounced reabsorption at the emission wavelengths. The appropriate model for Yb^{3+} -doped lasers is called the “quasi-three-level laser”, which will be described in detail in Sect. 2.3.2. To saturate the reabsorption losses of the quasi-three-level laser, high pump intensities are required. This is more easily obtained in a waveguiding structure, in which high pump-power densities and excellent overlap of pump and resonator modes can be achieved (Sect. 6.1).

2.2.2 Other RE^{3+} ions: Tb^{3+} , Dy^{3+} , Tm^{3+} , and Er^{3+}

Besides the Yb^{3+} ion, which has a top priority in this thesis, KYW can be easily doped with other active RE^{3+} ions. In particular, our interest is focused towards Tb^{3+} , Dy^{3+} , Er^{3+} , and Tm^{3+} . These ions are incorporated into the KYW host without changing the monoclinic symmetry of the unit cell, and, hence, high doping concentrations are possible. The incorporation of the Dy^{3+} , Er^{3+} , and Tm^{3+} ions into KYW has already been demonstrated and laser action in the doped crystals has been achieved (see Table 2.4). Often, to improve the laser performance, these lasing ions are excited indirectly with a sensitizer ion. Yb^{3+} is a suitable candidate for this role because of its high absorption cross-section, the broad absorption spectrum, and the considerable overlap between the Yb^{3+} emission and absorption bands of some other RE^{3+} ions. However, the investigation of fundamental spectroscopy and energy transfer processes in RE^{3+} - Yb^{3+} co-doped KYW crystals has started only recently.

Tb^{3+} - Yb^{3+} . Whereas spectroscopy of Dy^{3+} , Er^{3+} , or Tm^{3+} in KYW has been studied in [mac98, kam78, bag00], nothing is known about Tb^{3+} or energy-transfer mechanisms of the Tb^{3+} - Yb^{3+} pair in KYW. A possible limitation is the specific energy scheme of Tb^{3+} , which does not allow for a direct energy transfer from the only excited energy level of Yb^{3+} .

Still, the Yb^{3+} ion can be used as a sensitizer, and the excitation of Tb^{3+} into the upper 5D_4 level is possible via simultaneous energy transfer from two nearest Yb^{3+} ions (Fig. 2.11). This mechanism, known as *cooperative upconversion*, gives rise to a greenish fluorescence from the excited Tb^{3+} ions. However, in some Tb^{3+} - Yb^{3+} systems, the visible upconversion (UC) fluorescence was assigned to the direct GSA/ESA mechanism within coupled Tb^{3+} - Yb^{3+} pairs, especially at low temperatures [sal01]. In this respect, investigation of the Tb^{3+} - Yb^{3+} co-doped KYW layers can give fundamental insight into the energy transfer processes and reveal which factor (temperature, ratio of dopant concentrations, interatomic distances, etc.) determines one or the other UC mechanism.

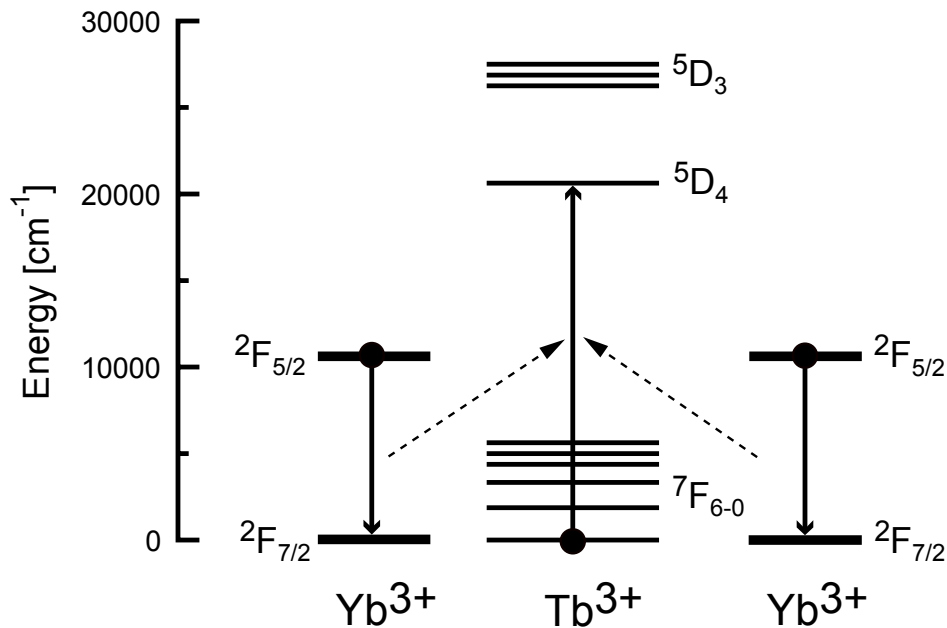


Fig. 2.11. Energy level schemes for the Tb^{3+} and Yb^{3+} ions. The cooperative energy transfer among two donors (Yb^{3+} ions) and an acceptor (Tb^{3+} ion) is indicated.

Dy³⁺-Yb³⁺. In contrary to Tb^{3+} , the Dy^{3+} ion has some intermediate energy levels, which match with the excited $^2F_{5/2}$ level of the Yb^{3+} ion (Fig. 2.8). This enables a direct energy transfer from an excited Yb^{3+} ion to a Dy^{3+} ion in its ground state. A second transfer from an excited Yb^{3+} ion to the same Dy^{3+} ion may upconvert the Dy^{3+} ion to the higher-lying $^4F_{9/2}$ excited state and leads to the generation of UC fluorescence. However, the dense energy level scheme of Dy^{3+} assumes numerous secondary relaxation channels and favors radiationless decay of the excited level. A fundamental study of the energy transfer processes within the Dy^{3+} - Yb^{3+} pair in KYW is required in order to evaluate a laser potential of this system.

Er³⁺-Yb³⁺. The Er^{3+} ion has a rich energy level scheme, which enables efficient laser operation in KYW:Er crystals at different wavelengths in the range of 0.85 to 2.9 μm (Fig.

2.8). Using the Yb^{3+} ion as the sensitizer, room-temperature CW laser operation around 1.54 μm has been demonstrated with KYW:Er,Yb crystals [kul97]. Moreover, the green UC fluorescence of Er^{3+} has been observed after selective excitation of Yb^{3+} in KYW:Er,Yb crystals [kul97, mat05]. This indicates the possibility of demonstrating green laser emission of the $^4\text{S}_{3/2} \rightarrow ^4\text{I}_{15/2}$ transition of Er^{3+} in KYW:Er,Yb, as has been shown in LiYF_4 :Er,Yb [mob97].

Tm³⁺ and Tm³⁺-Yb³⁺. Thulium-doped laser materials are emerging as very interesting active media with broad tunability for the 2- μm spectral region. The laser emission around 2 μm is based on the $^3\text{F}_4 \rightarrow ^3\text{H}_6$ transition, as indicated in Fig. 2.8. Recently, a KYW:Tm laser, having a slope efficiency up to 45%, was demonstrated under direct Ti:sapphire laser pumping near 800 nm [bag00]. The excitation of Tm^{3+} ions can also be realized in Tm^{3+} - Yb^{3+} co-doped KYW under laser diode pumping of Yb^{3+} at 980 nm with subsequent energy transfer to Tm^{3+} [bata02]. Still, the research of optimum doping levels, pumping wavelengths, and polarization configurations is required to develop a reliable diode-pumped KYW:Tm laser at 2 μm .

The investigation of energy-transfer mechanisms requires intense pumping [pol00], which significantly increases the probability of cooperative upconversion (Tb^{3+} - Yb^{3+} system) or two-step energy transfer (Dy^{3+} - Yb^{3+} and Er^{3+} - Yb^{3+} systems). The high pump density can be achieved by exploiting the waveguiding effect in thin active layers, as is described in Sect. 6.1.

2.3 KY(WO₄)₂:RE lasers

2.3.1 Overview of demonstrated KY(WO₄)₂:RE lasers

Due to the low symmetry and strong anisotropy of the KYW host, the emission and absorption cross-sections of RE^{3+} ions are exceptionally large for specific polarizations. The resulting short absorption lengths and high gain factors favor laser applications based on diode pumping, whereas the relatively broad linewidths permit generation of femtosecond pulses similar to glass materials but with improved performance. Since the first demonstration of laser action in KYW:Nd by Kaminskii *et al.* in 1971 [kam71], a number of CW and pulsed lasers based on KYW:RE crystals have been created (Table 2.4).

Table 2.4. Properties of some lasers based on bulk KYW:RE crystals.

Active ion ^A	Concentration (mol%) ^B	Emission wavelength (μm)	Temperature (K)	Operation mode ^C	Reference
Pr^{3+}	1.0	1.0223	300	P	[kam97]
Nd^{3+}	0.3 – 2.5	0.9137	77	P	[kam72]
	2.5	1.0688	300	P, CW	[kam71]
	2.5	1.3525	300	P, CW	[kam71]
Dy^{3+}	1 – 3	0.5737	110	P	[kam02]
	1 – 3	0.6637	110	P	[kam02]
Ho^{3+}	3	2.9395	300	P	[kam79]
Ho^{3+} (sens. $\text{Er}^{3+}, \text{Tm}^{3+}$)	3 (Ho^{3+}) 30 (Er^{3+}) 3 (Tm^{3+})	2.0720	220	P	[kam77]
Er^{3+}	3	0.8621	300	P	[kam78]
Er^{3+}	3-10	1.7355	300	P	[kam78]
Er^{3+}	3-50	2.8070	300	P	[kam78]
Er^{3+}	100	1.7372	300	P	[kam83]
Er^{3+} (sens. Yb^{3+})	0.5 (Er^{3+}) 5 (Yb^{3+})	1.54	300	CW	[kul97]
Er^{3+} (deactiv. $\text{Ho}^{3+}, \text{Tm}^{3+}$)	30 (Er^{3+}) 3 (Ho^{3+}) 3 (Tm^{3+})	2.6887	300	P	[kam77]
Tm^{3+}	6	1.928-1.936	300	P	[bat02]
Tm^{3+}	15	1.850-1.950	300	CW	[bag00]
Tm^{3+} (sens. Er^{3+})	0.5 (Tm^{3+}) 5 (Er^{3+})	1.92	110	P	[kam97]
Tm^{3+} (sens. Yb^{3+})	6 (Tm^{3+}) 5 (Yb^{3+})	1.85-2.00	300	CW	[bata02]
Yb^{3+}	5	1.025	300	P, CW	[kul97]
Yb^{3+}	5	1.028	300	P	[bru02]
Yb^{3+}	10	1.030-1.050	300	CW, P	[kis04]
Yb^{3+}	20	1050	300	CW, P	[dem00]
Yb^{3+}	30	1.035-1.053	300	CW, P	[kis04]
Yb^{3+}	100	1.074	300	q-CW	[klo02]
Yb^{3+}	100	1.068	300	CW	[klo03]

^A Active ion is the lasing ion; sensitizing or deactivating ions are also noted if any.

^B Concentration of the RE^{3+} ion is given with respect to the Y^{3+} ion.

^C P - pulsed mode, CW – continuous-wave mode, q-CW – quasi-continuous-wave mode.

2.3.2 Model of quasi-three-level laser for $\text{KY}(\text{WO}_4)_2:\text{Yb}$

As shown by Einstein, the probabilities of stimulated absorption and emission are equal for a given transition, and hence, in a simple two-level system it is not possible to create population inversion, which is a necessary condition for the generation of stimulated emission. Nevertheless, lasing is reachable in Yb^{3+} -doped materials because of the Stark splitting of the $^2\text{F}_{7/2}$ and $^2\text{F}_{5/2}$ states and respective Boltzmann population distributions within each Stark multiplet. Population inversion is achieved between excited Stark sub-levels with large Boltzmann factors and ground Stark sub-levels with small Boltzmann factors. This laser scheme is known as the “quasi-three-level” system [lac91]. Because a special emphasis is given to KYW:Yb in this thesis, it is necessary to describe in more detail the main parameters and rate equations of quasi-three-level lasers.

We consider an idealized energy scheme for an active ion that has two energy states (Fig. 2.12). Because of Stark splitting, each state is split into a few sub-levels which are strongly coupled and, hence, in thermal equilibrium. In this case, N_1 and N_2 represent the total population densities of all ground-state and all upper-state sub-levels, respectively. The population density of ions in both the ground and excited states equals the total active ion concentration, $N = N_1 + N_2$. Now let (0) and (1) represent the lower and upper sub-levels of the ground state, whereas (2) and (3) represent the lower and upper sub-levels of the excited state. The population densities are $N_1 b_1$ and $N_2 b_2$ in sub-levels (1) and (2), respectively, where b_1 and b_2 are the Boltzmann factors calculated from equation (2.2). The fluorescence lifetime of the excited state is represented by τ .

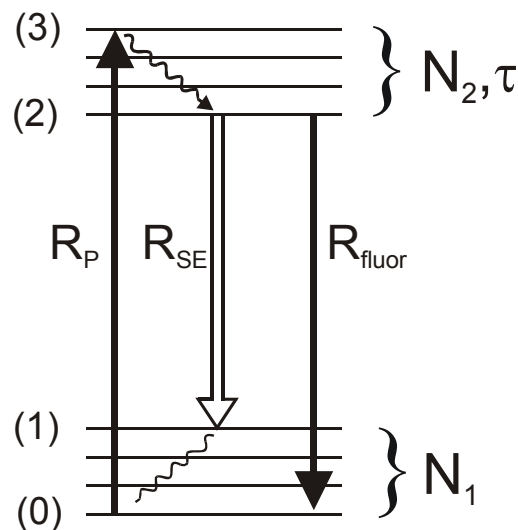


Fig. 2.12. Quasi-three-level laser scheme.

When pump light propagates through the active medium, the ions are excited from the ground state to the excited state, and the pump rate per unit time and volume can be calculated as:

$$R_P = \eta_q \frac{1}{\pi w_p^2 l} \frac{\lambda_p}{hc} P_{\text{abs}}. \quad (2.5)$$

Here, η_q is the quantum efficiency, which will be defined after equation (2.15). w_p is the mode waist of the pump beam, λ_p is the pump wavelength, h is Plank's constant, and c is the speed of light in vacuum. The absorbed pump power, P_{abs} , is a function of the initial pump power, P_{in} , and the active medium length l :

$$P_{\text{abs}} = \eta_{\text{coupl}} P_{\text{in}} \left\{ 1 - \exp[-\alpha(\lambda_p)l] \right\}. \quad (2.6)$$

Here, η_{coupl} accounts for incoupling losses of the initial pump beam into the active medium.

The absorption coefficient $\alpha(\lambda_p)$ at the pump wavelength λ_p is given by

$$\alpha(\lambda_p) = \sigma_a(\lambda_p) N_1. \quad (2.7)$$

$\sigma_a(\lambda_p)$ is the effective absorption cross-section at the selected pump wavelength. It includes the Boltzmann factor of the initial Stark sub-level.

The excited ions can decay into the ground state via spontaneous emission of the characteristic photon (fluorescence) or by stimulated emission of the characteristic photon after interaction with another photon having the same energy. The spontaneous fluorescence rate is

$$R_{\text{fluor}} = N_2 / \tau. \quad (2.8)$$

The stimulated emission is the inverse process of stimulated absorption, which has the same probability for a given transition. Therefore, the total stimulated emission rate is written as

$$R_{\text{SE}} = (\sigma_e N_2 - \sigma_a N_1) c \phi, \quad (2.9)$$

where σ_e and σ_a are the effective cross-sections for stimulated emission and absorption, respectively, and ϕ is the photon density in the active medium. Using equations 2.8 and 2.9, the rate equation for the population density in the excited state can be written as:

$$\frac{dN_2}{dt} = R_P - R_{\text{SE}} - R_{\text{fluor}} = R_P - (\sigma_e N_2 - \sigma_a N_1) c \phi - \frac{N_2}{\tau}. \quad (2.10)$$

When the difference $(\sigma_e N_2 - \sigma_a N_1) > 0$, population inversion between the upper and lower levels is achieved, which is a necessary condition for the Light Amplification using

Stimulated Emission Radiation (LASER). The stimulated emission can be repeatedly amplified within a resonator consisting of two mirrors. The respective change of photon density within the resonator is:

$$\frac{d\phi}{dt} = \frac{1}{2l_{\text{opt}}} \left\{ 2lR_{\text{SE}} - (-\ln[(1-L)R_1R_2])c\phi \right\}. \quad (2.11)$$

Here, l_{opt} and l are the lengths of the resonator and active medium, respectively. R_1 and R_2 are the reflectivities of the mirrors, and L stands for the round-trip cavity losses.

Once the stimulated-emission rate is high enough to compensate the reabsorption and cavity losses, the threshold condition for laser action is achieved. The photon density in the resonator as well as the population density of the excited state are constant under CW pumping. Setting equations (2.10) and (2.11) to zero, we obtain the absorbed power threshold:

$$P_{\text{thr}} = \frac{1}{\tau} \frac{2\sigma_a Nl - \ln[(1-L)R_1R_2]}{2(\sigma_e + \sigma_a)} \frac{1}{\eta_q} \pi w_p^2 \frac{hc}{\lambda_p}. \quad (2.12)$$

Expression (2.12) for quasi-three-level lasers is different from a similar formula for conventional four-level lasers by the presence of term $2\sigma_a Nl$ in the numerator [sve98]. This additional term, which accounts for the partial thermal population of the lower laser level, implies a larger absorbed power needed to create population inversion and reach laser threshold. Therefore, quasi-three-level lasers exhibit relatively high threshold powers.

The output laser power through one mirror with the reflectivity R_1 is:

$$P_{\text{out}} = \frac{1}{2} \frac{1}{\tau} \frac{2\sigma_a Nl - \ln[(1-L)R_1R_2]}{2(\sigma_e + \sigma_a) \ln[(1-L)R_1R_2]} \pi w_L^2 \frac{hc}{\lambda_p} \ln R_1 \left(\frac{P_{\text{abs}}}{P_{\text{thr}}} - 1 \right). \quad (2.13)$$

It follows from equation (2.13) that after the absorbed power passes the threshold, the output laser power increases linearly with the absorbed pump power. The performance of the laser system can be expressed via the slope efficiency

$$\eta_{\text{sl}} = dP_{\text{out}} / dP_{\text{abs}}, \quad (2.14)$$

which can be rewritten by differentiating equation (2.13):

$$\eta_{\text{sl}} = \eta_q \eta_{\text{St}} \frac{w_L^2}{w_p^2} \frac{\ln R_1}{\ln[(1-L)R_1R_2]}. \quad (2.15)$$

Here, η_q is the quantum efficiency $\eta_q = n_L / n_p$, where n_L and n_p are the numbers of laser and absorbed pump photons, i.e., η_q describes which percentage of pump photons is converted into laser photons. η_{St} is the Stokes efficiency $\eta_{\text{St}} = \lambda_p / \lambda_L$.

It is important to note that all above equations (2.5)-(2.15) hold true only for the space-independent model. This model considers a laser oscillating with uniform pump and mode energy distribution in the active medium [Sve98]. For example, an axially dependent absorption of pump energy, resulting in an axially dependent excitation density, is not considered in this model.

3. Fundamentals of liquid-phase epitaxy (LPE)

This chapter is devoted to the method of liquid-phase epitaxy (LPE). After a historical overview of the method, the principles and the driving force of epitaxial growth are presented. Important experimental parameters governing the growth by LPE, like relative supersaturation, substrate misorientation, and lattice misfit are discussed quantitatively with respect to the LPE of KYW:RE layers on KYW substrates.

3.1 Introduction to LPE

Liquid-phase epitaxy is a process in which a single crystal layer is grown from a dilute molten solution onto a flat oriented single crystal substrate. The expression ‘epitaxy’, originates from the Greek ‘επι ταξις’, which means “over orderliness”. LPE can be classified into *homoepitaxy*, when layer and substrate have the same chemical composition and crystal structure, and *heteroepitaxy*, in which layer and substrate are different in their chemical compositions but similar in their crystallographic relations. In both cases, the substrate and layer materials must be chemically and thermally stable under the growth conditions.

Historically, LPE has been the pioneering technology for preparing epitaxial layers of compound semiconductors, mainly III–V materials, like GaAs, GaSb, InP, and their ternary alloys. The application of LPE to the growth of the III–V compounds has been introduced by Nelson *et al.* at RCA laboratories in 1963 [nel63]. Magnetic garnet materials have also been extensively grown by LPE for applications such as magnetic bubble devices or optical isolators [bla72]. In 1972, the first LPE experiments on transparent optical materials showed that high-quality layers can be successfully produced for applications such as waveguide lasers, amplifiers, and saturable absorbers [tie72, fer99].

The major advantages of LPE compared to other epitaxial techniques from the vapor phase (vapor-phase epitaxy (VPE), molecular beam epitaxy (MBE), metalorganic chemical vapor deposition (MOCVD), or pulsed laser deposition (PLD) are:

- LPE is a near-equilibrium process; supersaturations imposed for growth are very low, and μm -thick, single-crystalline thin films are feasible;
- LPE is a non-vacuum process, thus low-cost and simple apparatus is used;

- LPE has a high degree of safety because the raw materials and the waste products are, usually, not pyrophoric;
- deposition efficiency of epitaxial material and respective growth rates are relatively high, which allows thick layers up to 100 μm to be grown.

The most notable limitations of LPE are:

- problems to grow nanometer-thin layers, e.g., quantum wells;
- problems to grow a large number of uniform stacked layers;
- small substrate sizes;
- rather difficult thickness control.

Because of these limitations of LPE, epitaxial techniques from vapor phase have become more important for industrial growth of thin-layer semiconductors. However, many companies that are now gradually moving into MOCVD or MBE still rely on LPE as their stand-by technique. Especially, this holds true when thick layers are required or oxide materials with complex structure have to be grown. For instance, Atanasov *et al.* reported on the first thin film growth of a double tungstate by PLD in 2000 [ata00]. Laser ablation of a stoichiometric single-crystal target was used to obtain thin films of Nd-doped KGdW, which is a compound related to KYW. The films were polycrystalline with a thickness of about 0.7 μm . However, problems related to deviation from stoichiometry, formation of unwanted phases such as $\text{Gd}_2(\text{WO}_4)_3$ or a high-temperature β -KGdW modification, and amorphization of the films appeared. Subsequent PLD studies performed in the same group using different substrate materials and deposition regimes did not lead to any significant improvement of the layer quality and optical losses of as-obtained waveguiding layers were above 5 dB cm^{-1} [jel02], [ata02]. The poor layer quality can be explained by the fact that PLD operates at far-from equilibrium conditions. This complicates considerably the growth of oxide materials with a complex monoclinic structure, while it remains possible to grow some simpler oxides with hexagonal or cubic structures using PLD [jel98].

Therefore, LPE has been chosen as the suitable method for the growth of single-crystalline KYW:RE layers. Low supersaturations achievable in solution together with reasonable growth rates onto a single-crystal substrate, are the fundamental guaranties that ensure the production of high-quality KYW:RE layers with thicknesses of 5 to 50 μm , which are desirable for optical waveguide applications.

3.2 Phase diagrams

The thermodynamic driving force for LPE is generated by cooling the solution below the saturation temperature. The solution can be represented as a binary system shown schematically in Fig. 3.1. The solid arc represents the solubility curve; there is a non-saturated liquid solution above the curve, and a saturated solution coexisting with the solute deposit below the curve. In the case of “ideal” solutions without chemical interactions, the solubility curve obeys the Arrhenius-type equation

$$\ln\left(\frac{n_2}{n_1}\right) = -\frac{L_{\text{sol}}}{R}\left(\frac{1}{T_2} - \frac{1}{T_1}\right), \quad (3.1)$$

where n_1 and n_2 are the molar fractions of the solute in the saturated liquid solution kept at the temperatures T_1 and T_2 , respectively. L_{sol} is the heat of solution and R is the universal gas constant, $8.314 \text{ J K}^{-1} \text{ mol}^{-1}$.

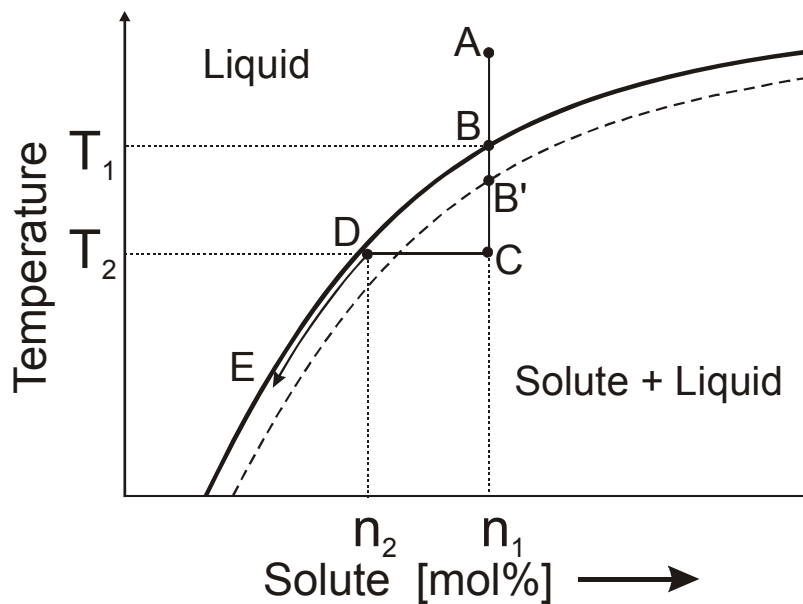


Fig. 3.1. Typical solubility curve showing a pass of the system composition during cooling.

We consider the initial liquid solution containing n_1 mol% of solute and the solution is kept at a certain initial temperature (point A). When cooling the system to temperature T_2 , the solution crosses the solubility (liquidus) curve at temperature T_1 (point B) and moves to point C located in the two-phase region. Hence, the solution becomes supersaturated with respect to the solute, and the driving force for the solute precipitation appears. The solute precipitation

continues until point D on the liquidus curve is reached and, consequently, the solute fraction in the liquid solution is decreased from n_1 to n_2 . During further cooling the solution moves from point D to point E.

It is necessary to point out that in the absence of a seed (substrate) crystal or any other centers of crystallization (crucible walls, impurities), the spontaneous precipitation will not start until the solution reaches point B' lying on the dashed line. The region between the liquidus line and the dashed line is called the metastable or *Ostwald-Miers* (OM) region. The solution is supersaturated in the OM region, however, the spontaneous crystallization cannot start because the dimensions of the existing atomic clusters are still below a certain critical size r^* , which is imperative to initiate bulk crystallization. The nucleation mechanisms and calculation of the critical nucleus size r^* will be described in Sect. 3.3. It is remarkable that in some systems, the OM region can be very large and, in the absence of any nucleation centers, the respective solution supercooling can be as high as 200 K [ivl88].

The situation is different when the seed crystal (substrate) is brought in contact with the supersaturated solution that still remains in the OM region. The substrate acts as a huge nucleation center, and the solute excess can be deposited onto the substrate. Thus, only a very small supercooling below the saturation temperature T_1 is sufficient to achieve a slow and well-controlled growth along the B–D–E liquidus curve. This is the key point in LPE.

3.3 Nucleation and epitaxy

The critical step in the nucleation of an epitaxial layer on the substrate surface is the formation of a cluster of atoms, which is sufficiently large to constitute a stable, growing nucleus. For a “two-dimensional” (2D) nucleation the radius of the critical nucleus is defined as

$$r^* = \frac{\gamma_m a}{kT\sigma}. \quad (3.2)$$

Here, γ_m is the free energy per growth unit, a is the lattice constant, and k is the Boltzmann constant. T is the absolute temperature and σ is the relative supersaturation. The free energy per growth unit, γ_m , represents the binding energy of the growth unit to the crystal substrate, and is approximately equal to

$$\gamma_m = \frac{L_{\text{sol}}}{6N_A}, \quad (3.3)$$

where L_{sol} is the heat of solution and N_A is Avogadro's number, $6.02 \times 10^{23} \text{ mol}^{-1}$.

However, the values of r^* and σ used in equation (3.2) hold true only for atomically "flat" ideal surfaces. One should take into account that the surface of real crystals contains many intrinsic imperfections, e.g., dislocations, which facilitate nucleation. In 1951, Burton, Cabrera, and Frank proposed the general theory of nucleation (BCF theory), in which nucleation mechanisms are discussed for the atomically "rough" surfaces [bur51]. As a model system, BCF considers a screw dislocation, which acts as a continuous source of steps on the surface of a crystal substrate. Fig. 3.2a shows the crystal face with a screw dislocation emerging at point P. The presence of a step associated with such a screw dislocation eliminates the need for 2D surface nucleation, resulting in the nucleation-free growth of an Archimedean-type spiral (Fig. 3.2b, c, d).

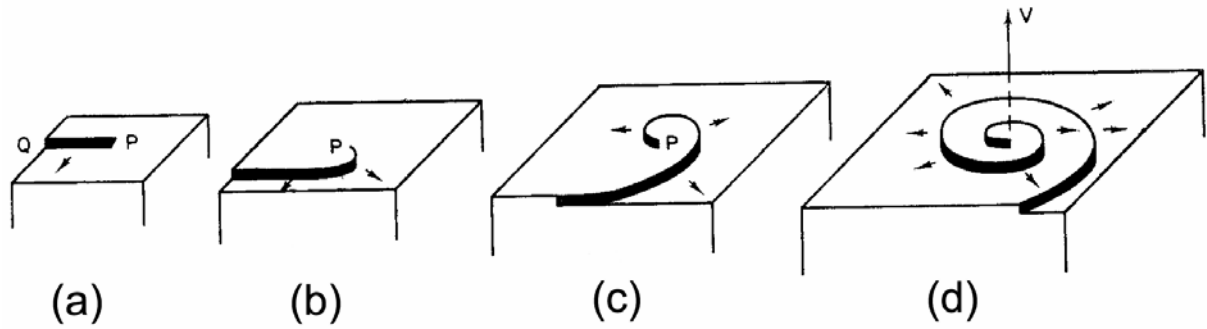


Fig. 3.2. Development of a growth spiral.

According to Cabrera and Levine [cab56], the interstep distance y_0 between the steps of the spiral is

$$y_0 \approx 19r^* = \frac{19\gamma_m a}{kT\sigma}. \quad (3.4)$$

Assuming that the growth spiral can originate simultaneously from several nearby dislocations and the growth step can be several lattice units in height, a more rigorous approach of the interstep distance is

$$y_0 = \frac{19\gamma_m h}{\varepsilon kT\sigma}. \quad (3.5)$$

Here, h is the step height ($h = ma$, where a is the lattice constant, m is the number of lattice units in the step), and ε is a factor, which can be as large as the number of dislocations forming the spiral.

Among numerous interdependent factors that govern the initial growth stages, one should consider three main parameters, which can be controlled experimentally during LPE: supersaturation, substrate misorientation, and lattice misfit. These parameters are used in this thesis based on the following relations and definitions:

A. The relative supersaturation determines the radius of the critical 2D nucleus in equation (3.2) and is defined as:

$$\sigma = (n - n_e) / n_e, \quad (3.6)$$

with n and n_e being the actual and equilibrium concentrations of the solute at a given temperature T . Since it is difficult to measure experimentally the real equilibrium concentration n_e to be used in equation (3.6), the relative supersaturation can be calculated from equation (3.5) by inserting mean values for the observed interstep distance and step height:

$$\sigma = \frac{19\gamma_m h}{y_0 \varepsilon k T} = \frac{19L_{\text{sol}} h}{6y_0 \varepsilon k T N_A}. \quad (3.7)$$

For example, applying equation (3.1) to the solubility curve of KYW in the $\text{K}_2\text{W}_2\text{O}_7$ solvent (Sect. 4.4.1), we obtain $L_{\text{sol}} = 127.5 \text{ kJ mol}^{-1}$. Consequently, if a b -oriented epitaxial layer of KYW grown from the $\text{K}_2\text{W}_2\text{O}_7$ solvent exhibits growth steps with $h = 20 \text{ nm}$ and $y_0 = 20 \text{ }\mu\text{m}$, which originate from a single dislocation center ($\varepsilon = 1$), the respective relative supersaturation $\sigma = 0.041$ at $T = 1173 \text{ K}$ from equation (3.7). This value is close to $\sigma = 0.03$ for the LPE of $\text{YBa}_2\text{Cu}_3\text{O}_{7-x}$ layers grown at 1273 K from the self-solvent $\text{BaCuO}_2/\text{CuO}$ [kle96].

Besides σ , the supersaturation can also be expressed via respective supercooling

$$\Delta T = T_{\text{sat}} - T \approx \frac{\sigma R T^2}{L_{\text{sol}}}. \quad (3.8)$$

Here, T_{sat} and T are the saturation and actual temperatures for a given solute concentration. The relative supersaturation $\sigma = 0.041$ corresponds to the supercooling $\Delta T = 3.7 \text{ K}$ at the growth temperature $T = 1173 \text{ K}$.

B. The substrate misorientation is a measure which expresses the angular deviation of the substrate surface from a selected crystallographic plane. The substrate misorientation assumes the presence of open steps on the substrate surface, and the interstep distance is related to the angle of misorientation, φ , by

$$y_0 = a_s / \tan \varphi, \quad (3.9)$$

with a_s being the substrate lattice parameter.

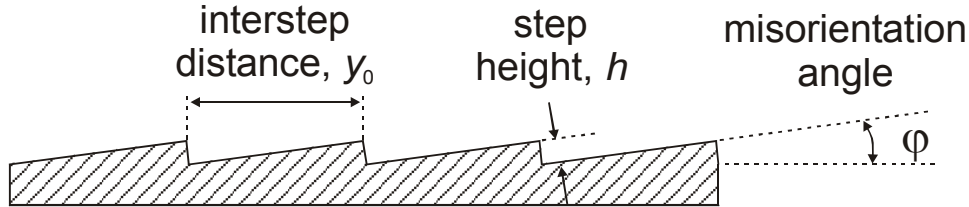


Fig. 3.3. Substrate misorientation.

The presence of already existing steps on the substrate surface, as shown in Fig. 3.3, considerably changes the nucleation and development of the epitaxial layer. For instance, Bauser [bau94] distinguished four different growth mechanisms in the LPE of semiconductors depending on the misorientation angle φ :

- 1) $\varphi \approx 0^\circ$ - Facet growth: the substrate surface does not exhibit any initial steps. In the presence of screw dislocations a spiral growth with monomolecular steps according to the BCF theory is observed; at higher supersaturations 2D nucleation is possible.
- 2) $0^\circ < \varphi \leq 0.1^\circ$ - Near-facet growth: the substrate surface exhibits initial steps with large interstep distances. Growth steps normally do not exceed the height of a few unit cells and the layer surface is relatively smooth.
- 3) $0.1^\circ < \varphi < 2^\circ$ - Terrace growth: the initial steps on the substrate surface are very numerous, and they bunch during the growth. The step-bunching increases the average height and distance of steps giving rise to the formation of macrosteps (up to 100-200 nm) with flat growth terraces in between.
- 4) $\varphi \geq 2^\circ$ - Terrace-free growth: the misorientation is too high to form flat growth terraces; the layer surface has a wavy, sinusoidal structure.

Obviously, the desirable misorientation of KYW substrates is in the range $0^\circ < \varphi \leq 0.1^\circ$ to ensure a very smooth layer surface on the one hand, and a sufficient number of initial steps to facilitate layer nucleation, on the other hand. The misorientation of available substrates depends on the precision of orientation and polishing of monoclinic KYW crystals. In some cases, the orientation errors for monoclinic crystals can be as high as 0.1° - 0.3° , which can lead to the pronounced step-bunching on the layer surface.

C. The substrate misfit shows the difference between crystallographic and thermal properties of the substrate and the epitaxial layer. The relative lattice misfit (hereafter lattice misfit) at the temperature T_1 can be expressed as

$$f_{\text{latt},T_1} = (a_{S,T_1} - a_{L,T_1}) / a_{L,T_1}, \quad (3.10)$$

where a_{S,T_1} and a_{L,T_1} are the lattice constants of the substrate and the layer at the temperature T_1 . In the case of ideal homoepitaxy, when $a_{S,T_1} = a_{L,T_1}$, the lattice misfit is zero. For heteroepitaxy, the lattice mismatch can be either tensile, $f_{\text{latt},T_1} > 0$, or compressive, $f_{\text{latt},T_1} < 0$.

The lattice constant of the KYW:RE layer, a_{L,T_1} depends on the type and concentration of the RE ion and can be found using Vegard's law:

$$a_{L,T_1} = x \times a_{\text{KREW},T_1} + (1-x) \times a_{\text{KYW},T_1}. \quad (3.11)$$

Here, a_{KREW,T_1} and a_{KYW,T_1} are the lattice constants at the temperature T_1 of KREW and KYW, respectively, and x is the molar fraction of the RE with respect to Y. The lattice constants of some KREW crystals are listed in Table 3.1, together with their relative lattice misfit with KYW.

Table 3.1. Lattice parameters of KREW crystals in the space group $C2/c$ and lattice misfit with KYW at room temperature [lb77].

Compound	a (nm) / misfit with KYW (%)	b (nm) / misfit with KYW (%)	c (nm) / misfit with KYW (%)	β ($^\circ$)
KYW	1.064 / -	1.035 / -	0.754 / -	130.50
KGdW	1.068 / -0.38	1.044 / -0.86	0.7602 / -0.82	130.78
KTbW	1.066 / -0.19	1.042 / -0.67	0.7568 / -0.37	130.63
KDyW	1.066 / -0.19	1.038 / -0.29	0.7577 / -0.49	130.78
KHoW	1.063 / 0.09	1.034 / 0.10	0.7553 / -0.17	130.75
KErW	1.062 / 0.19	1.032 / 0.29	0.7542 / -0.03	130.67
KTmW	1.060 / 0.38	1.029 / 0.58	0.7510 / 0.40	130.70
KYbW	1.060 / 0.38	1.027 / 0.78	0.7505 / 0.47	130.75
KLuW	1.060 / 0.38	1.024 / 1.07	0.7500 / 0.53	130.75

Whereas the monoclinic angle β is nearly constant, the lattice constants of KREW crystals gradually decrease from KGdW to KLuW. KHoW has the lowest lattice misfit with KYW.

Thus, the layers doped with Gd, Tb, or Dy possess a compressive strain on an undoped KYW substrate, and the layers doped with Er, Tm, Yb, or Lu are under a tensile strain. It is important to point out that the lattice mismatch between KREW and KYW is the highest for the b -axis, i.e. along the [010] direction.

Lattice constants of crystals vary with temperature according to the thermal dilatation equation:

$$a_{T_2} = a_{T_1}(1 + \alpha\Delta T), \quad (3.12)$$

where a_{T_1} and a_{T_2} are the lattice constants at temperatures T_1 and T_2 , and α is the linear thermal expansion coefficient. Table 3.2 shows the thermal expansion coefficients along different crystallographic directions for some KREW crystals.

Table 3.2. Linear thermal expansion coefficients of some KREW crystals [puj99].

Compound	$\alpha_{[100]}, 10^{-6} \text{ K}^{-1}$	$\alpha_{[010]}, 10^{-6} \text{ K}^{-1}$	$\alpha_{[001]}, 10^{-6} \text{ K}^{-1}$
KYW	11.0	1.9	17.8
KGdW	13.6	2.8	22.8
KErW	10.4	2.1	17.0
KYbW	10.5	2.6	16.3

For KYW:RE layers grown on KYW substrates, the lattice misfit at growth temperature is different from that at room temperature. The difference in the lattice misfits represents a strain component that appears during cooling RE-doped layers down from growth temperature T_2 , to room temperature T_1 :

$$f_{\text{latt},T_2} - f_{\text{latt},T_1} = \varepsilon_{\text{therm}}. \quad (3.13)$$

Here, f_{latt,T_1} and f_{latt,T_2} are the lattice misfits at the temperatures T_1 and T_2 , respectively. Inserting equations (3.10) and (3.12), one can rewrite equation (3.13) as

$$\varepsilon_{\text{therm}} \approx (\alpha_L - \alpha_S)\Delta T, \quad (3.14)$$

where α_L and α_S are the thermal expansion coefficients of the layer and the substrate, respectively, and ΔT is the temperature interval, $\Delta T = T_2 - T_1$. For example, for a KYbW layer on KYW substrate cooled from 900°C down to 25°C ($\Delta T = 875 \text{ K}$), the induced thermal expansion strain, $\varepsilon_{\text{therm}}$, is -4.7×10^{-4} (compressive), 6.1×10^{-4} (tensile), and -1.41×10^{-3} (compressive) for the a , b , and c -crystallographic axis, respectively.

Besides the layer strain induced by the lattice misfit f_{latt} , epitaxial layers can exhibit an additional strain which is determined by the growth mechanism. This strain, abbreviated as ε_{def} , includes different layer defects, like stacking faults, microvoids, gas inclusions, unwanted impurities, etc. The strain due to the defects, ε_{def} , is formed during the layer growth and present in the grown layer after cooling down to room temperature.

D. Accommodation of the lattice misfit. Generally, the misfit-induced strain in an epitaxial layer can be accommodated by elastic relaxation or can be relieved via formation of misfit dislocations.

The layer is said to be pseudomorphic if it is strained elastically in order to bring the lattices of the layer and the substrate into register at the interface. The elastic strain in the layer is then equal to the relative lattice misfit f_{latt} . However, the elastic relaxation is possible only if the lattice misfit is very small, e.g., $f_{\text{latt}} < 1 \times 10^{-4}$ for a 1- μm thin garnet layer [mat72]. At higher lattice mismatches, it is energetically more favorable to accumulate the strain locally at a layer–substrate interface by forming misfit dislocations during the layer growth. Fig. 3.4 shows the formation of misfit dislocations in an epitaxial layer under a tensile strain by inserting additional crystallographic planes. The misfit dislocations are characterized by the dislocation spacing

$$d = b / \varepsilon_{\text{disl}, T_2}, \quad (3.15)$$

where b is the Burgers vector that characterizes the dislocation, and $\varepsilon_{\text{disl}, T_2}$ is the layer strain accommodated by misfit dislocations at the growth temperature T_2 .

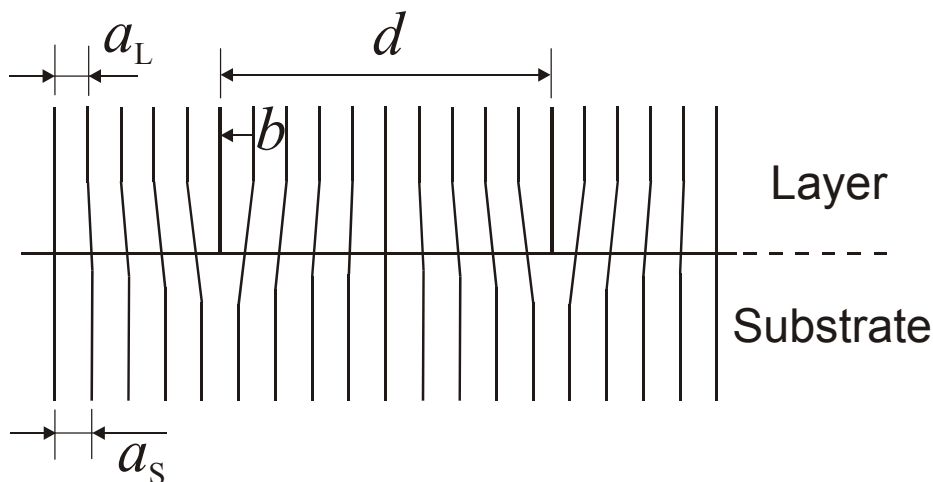


Fig. 3.4. Insertion of misfit dislocations at the layer/substrate interface.

The layer thickness, h_{disl} , at which it becomes energetically favorable for misfit dislocations to appear can be estimated from the transcendental equation [mat72]

$$h_{\text{disl}} = \frac{b}{8\pi f_{\text{latt},T2}(1+\nu)} \left(\ln \frac{h_{\text{disl}}}{b} + 1 \right), \quad (3.16)$$

where ν is the Poisson's ratio of the layer, $\nu = 0.290$ for $\text{KY}(\text{WO}_4)_2$ [kam01].

E. Critical layer thickness. Summarizing possible strain compensations described above, the actual strain in the grown layer at room temperature T_1 consists of the lattice misfit at room temperature, $f_{\text{latt},T1}$, the strain due to the defects, ε_{def} , and the layer strain accommodated by misfit dislocations during the growth, $\varepsilon_{\text{disl},T2}$:

$$\varepsilon = f_{\text{latt},T1} + \varepsilon_{\text{def}} - \varepsilon_{\text{disl},T2}. \quad (3.17)$$

The “minus” sign before term $\varepsilon_{\text{disl},T2}$ comes from the fact that the insertion of misfit dislocations reduces the layer strain at growth temperature. Using equation (3.13), expression (3.17) can be rewritten as

$$\varepsilon = f_{\text{latt},T2} - \varepsilon_{\text{therm}} + \varepsilon_{\text{def}} - \varepsilon_{\text{disl},T2}. \quad (3.18)$$

The actual layer strain ε should be accommodated by elastic relaxation; otherwise the strain must be released via cracking the layer. The critical layer strain for the crack formation, $\varepsilon_{\text{crit}}$, can be estimated from [mat72]:

$$\varepsilon_{\text{crit}} = \sqrt{\frac{a_{L,T1}(1-\nu)^2}{8\pi h}}. \quad (3.19)$$

Here, h is the layer thickness. Equation (3.19) can be rewritten in order to find the critical layers thickness, h_{crit} , above which the layer with a given actual strain will crack:

$$h_{\text{crit}} = \frac{a_{L,T1}(1-\nu)^2}{8\pi\varepsilon^2}. \quad (3.20)$$

Finally, when the actual strain (in particular tensile strain) exceeds the fracture strength of the layer material, the cracks are formed regardless of the layer thickness. The respective critical strain, $\varepsilon_{\text{fract}}$, for the spontaneous fracture was investigated for different epitaxial layers of garnets [mat72] and its approximate value was found to be

$$\varepsilon_{\text{fract}} = (1-\nu)/10. \quad (3.21)$$

All given equations for h_{disl} , h_{crit} , and $\varepsilon_{\text{fract}}$ assume elastically isotropic layers with a cubic structure. Although KYW has the monoclinic structure with non-equal crystallographic directions, the above equations are used in this thesis to obtain approximate values of the critical thicknesses without complex geometrical derivations. For instance, Fig. 3.5 shows predictions of the critical thickness for the insertion of misfit dislocations (line A calculated from equation (3.16), for the formation of cracks (line B calculated from equation (3.20), and for the spontaneous fracture (line C calculated from equation (3.21) of KYW:RE layers on KYW substrates.

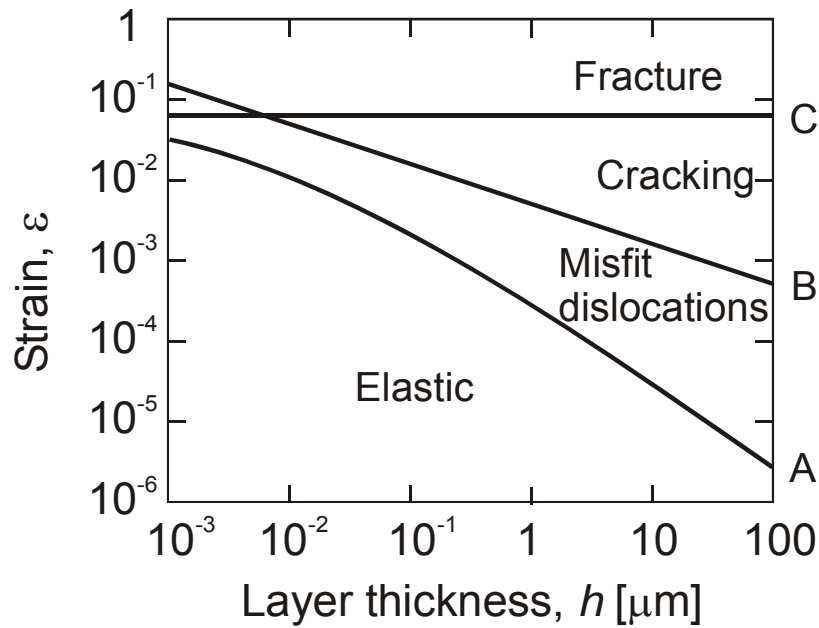


Fig. 3.5. Prediction of critical strain/thickness for different relaxation mechanisms in the KYW:RE layers.

Below line A it is energetically favorable for the film to strain elastically; above line B cracks propagate. The behavior of the layer structure between lines A and B depends on the density and mobility of the misfit dislocations formed at the layer-substrate interface at the growth temperature to compensate the lattice misfit $f_{\text{latt},T2}$:

- If during epitaxy the optimum number of misfit dislocations is generated, the layer is relaxed at the growth temperature and the lattice misfit is fully accommodated by the misfit dislocations, $f_{\text{latt},T2} = \varepsilon_{\text{disl},T2}$. When cooling down to room temperature, the induced thermal expansion misfit appears due to the difference in thermal expansion coefficients between the layer and the substrate. Consequently, the actual layer strain, which should be used for the vertical strain axis in Fig. 3.5, is obtained by simplifying equation (3.18), $\varepsilon = \varepsilon_{\text{def}} - \varepsilon_{\text{therm}}$.

- The density of misfit dislocations lies below the optimum value because of some difficulties associated with the creation of the misfit dislocations. The difficulties can arise in many different ways, e.g., too high Peierls-Nabarro stress for the dislocation nucleation, the insufficient number of threading dislocations in the substrate, the absence of suitable slip systems, or the blockage of the dislocation movement on grain boundaries or twins. As a result, thin layers of complex oxides, like garnets grown on garnet substrates, usually do not contain the misfit dislocations and, therefore, the lattice misfit strain has to be accumulated elastically or via the crack formation [mat72]. In this case, $f_{\text{latt},T1} \gg \varepsilon_{\text{disl},T2}$ and the actual layer strain used for the vertical axis in Fig. 3.5 can be calculated from equation (3.17) as $\varepsilon = f_{\text{latt},T1} + \varepsilon_{\text{def}}$.

In order to evaluate the density of misfit dislocations, we assume that for a high-quality KYW:RE layer the strain due to defects, ε_{def} , is negligible as compared to the lattice misfit $f_{\text{latt},T1}$ or thermal strain $\varepsilon_{\text{therm}}$. Hence, $\varepsilon \approx -\varepsilon_{\text{therm}}$ if the optimum number of misfit dislocations is generated or $\varepsilon \approx f_{\text{latt},T1}$ if no misfit dislocations are inserted. As predicted from line B in Fig. 3.5, for a *b*-oriented KYW:Yb layer with the thickness of 50 μm , the cracks should appear at the critical layer strain of about 7×10^{-4} . For instance, this strain along the *c*-crystallographic axis of a KYW:Yb layer corresponds to an Yb^{3+} concentration of 49.8 mol% if $\varepsilon \approx -\varepsilon_{\text{therm}}$, or 14.9 mol% if $\varepsilon \approx f_{\text{latt},T1}$. The value of 14.9 mol% is much closer to the maximum Yb^{3+} concentration of 20 mol% reported for a crack-free, 48- μm thick KYW:Yb layer in [azn04]. Therefore, one can assume that the formation of misfit dislocations in KYW:RE layers is hindered to a large extent and the lattice misfit at room temperature, $f_{\text{latt},T1}$, can to be taken into account when estimating approximately the critical thickness for cracks formation. Similarly, the maximum RE^{3+} concentration for a 50- μm crack-free layer is expected to be 18.9 mol% and 14.3 mol% for Tb^{3+} and Dy^{3+} , respectively.

3.4 Growth modes

The nucleation and subsequent development of the layer are governed by a number of parameters [cle98]: the surface energies of substrate, layer, and their interface, the solution supersaturation, the lattice misfit between the substrate and layer, the substrate misorientation, the surface diffusion at the growth temperatures, the stoichiometry of the deposited

compound, the presence of impurities condensing inside the layer, the partial pressure of reactive species, etc. There are two main approaches for the classification of epitaxial growth modes.

The first approach is based on the wetting behavior at the layer-substrate interface. Accordingly, three classical epitaxial growth modes are derived by considering the interfacial tensions of atomic clusters on a flat substrate surface [bau58]. Ordered by decreasing wettability, these modes are I) the Frank-van der Merwe (FVM) mode, which assumes the complete wetting of the substrate and layer-by-layer growth with macroscopic interstep distances [fra49]; II) the Volmer-Weber (VW) mode, which is characterized by the medium or low wetting leading to the 3D island formation [vol26]; III) the Stranski-Krastanov (SK) mode, which is an intermediate state between the FVM and VW modes; the SK mode first starts with the layer-by-layer growth and continues with the islands formation [str38]. The substrate wettability depends mainly on the composition of layer and substrate but also on the presence of impurities and lattice misfit, i.e. a large lattice mismatch normally causes a low wettability. These three growth modes are shown schematically in Fig. 3.6.

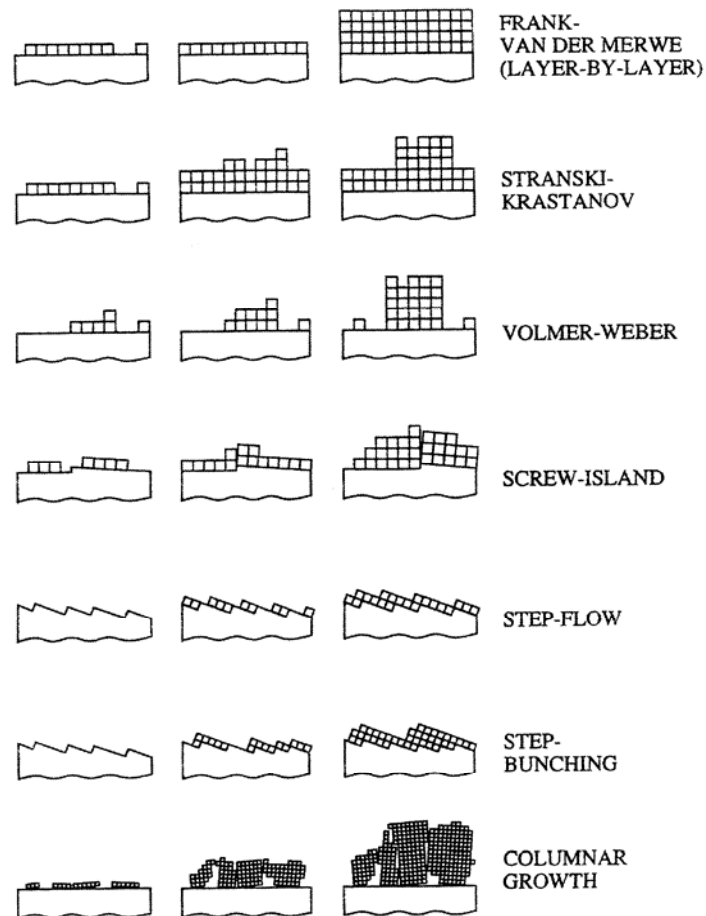


Fig.3.6. Growth modes.

The four other growth modes consider the initial state of the substrate surface, which is not atomically “flat”: IV) screw-island growth, where the presence of screw dislocations may lead to the growth of hillocks and their coalescence; V) the step-flow mode is very similar to the FVM mode and achievable by using slightly misoriented substrates; VI) step-bunching, where the growth steps are bunched to compensate a considerable substrate misorientation; VII) columnar growth is, in principal, a continuation of the VW growth mode without coalescence of the islands because of anti-phase grain boundaries.

Ideally, the layer-by-layer FVM mode is desirable to obtain high-quality KYW:RE layers. It requires perfectly oriented substrates with $\varphi \approx 0^\circ$, which is possible only for an ideal natural face of the KYW crystal. However, a bulk KYW crystal contains only a few suitable natural faces and, therefore, several oriented substrates are cut from one crystal in order not to waste the crystal material. During the cutting and polishing, a small substrate misorientation appears and the step-flow growth mode onto the existing substrate surface steps is possible. If the substrate misorientation is on the order of 0.1° , the step-flow mode is easily transformed into the step-bunching. There are several phenomena that could induce the appearance of step-bunches even on a slightly misoriented substrate: the variation in step source activity along the substrate surface, inhomogeneities in the solute supersaturation because of liquid flow, or the incorporation of step-stopping impurities. For a given substrate and solution composition, no rational way has been found so far to fully exclude the appearance of step bunches [che04]. They can be partially suppressed by using better-oriented substrates, lowering the supersaturation, and controlling the solution flow along the substrate surface. The as-grown layer surface with the step bunches (10-100 nm in height) has to be polished afterwards to avoid scattering losses in optical applications. A more severe problem is the VW or columnar growth, where grain boundaries and the coalescence of individual islands may induce strong scattering losses that cannot be eliminated by polishing or any other treatment.

3.5 Growth rate

When a substrate is immersed in the supersaturated solution, the solute material must be transported through the solution volume to reach the substrate surface. The solute transport can be conventionally divided into two stages: 1) solute transport to the proximity of the substrate due to natural or forced convection, and 2) diffusion of the solute particles through the diffusion boundary layer to the substrate surface. The driving force for the diffusion

through the boundary layer is the difference in solute concentrations. At the substrate-solution interface, the solute concentration approaches the equilibrium value, whereas in the bulk solution, the solute concentration is higher and nearly constant. If the solute concentration gradient is uniform over the boundary layer width, the linear growth rate is given by the Nernst equation [elw75]:

$$v = \frac{D}{\rho} \frac{(n - n_e)}{\delta}. \quad (3.22)$$

Here, n and n_e are the solution and the equilibrium solute concentrations, D is the diffusion coefficient, ρ is the crystal density, and δ is the width of the diffusion boundary layer. Assuming a laminar flow of the solution over the substrate surface, Carlson [car58] derived the expression for the boundary layer width

$$\delta = \left\{ 0.463 \left(\frac{\eta}{\rho_{sn} D} \right)^{1/3} \left(\frac{u \rho_{sn}}{\eta L} \right)^{1/2} \right\}^{-1}, \quad (3.23)$$

where ρ_{sn} is the solution density, η is the dynamic viscosity of the solution, u is the flow velocity, and L is the length of the substrate face. Burton, Prim, and Slichter [bur53] gave a similar formula for a substrate rotating in the solution

$$\delta \approx 2^{2/3} D^{1/3} \left(\frac{\eta}{\rho_{sn}} \right)^{1/6} \omega^{-1/2}, \quad (3.24)$$

where ω is the angular velocity of the crystal rotation. The thickness δ varies as $u^{-1/2}$ (or $\omega^{-1/2}$), and, generally, it is on the order of 0.05 cm for rotation rates of 10-100 rounds per minute (rpm). For instance, if a diluted solution of KYW in the $K_2W_2O_7$ solvent has $\eta = 4.5 \times 10^{-2}$ g $cm^{-1} s^{-1}$, $\rho_{sn} = 4.3$ g cm^{-3} , and $D \approx 1 \times 10^{-5}$ $cm^2 s^{-1}$, the diffusion layer thickness $\delta = 0.036$ cm for the rotation rate $\omega = 0.2$ s^{-1} (12 rpm).

During LPE, the solute flow is faster at the substrate edges, leading to the layer edges growing faster than the central parts. The rapid growth of layer edges may cause hopper growth or inclusion of the mother solution. Carlson derived empirically the maximum size of inclusion-free crystals taking into account the beneficial role of hydrodynamics. Using this concept, the maximum stable linear growth rate is calculated as

$$v_{\max} = \left(\frac{0.214 D u \sigma^2 n_e^2}{Sc^{1/3} \rho_{sn}^2 L} \right)^{1/2}. \quad (3.25)$$

Here, $Sc = \eta/\rho D$ is the Schmidt number, which is a dimensionless constant for every liquid at a given temperature. Taking into account that $u = \pi L \omega$, equation (3.25) can be rewritten for a rotating substrate

$$v_{\max} = \left(\frac{0.214 \pi D \omega \sigma^2 n_e^2}{Sc^{1/3} \rho_{sn}^2} \right)^{1/2}. \quad (3.26)$$

Equation (3.26) includes many parameters, which are difficult to measure directly: the diffusion coefficient D , the solution supersaturation σ , and the equilibrium solute concentration n_e . Nevertheless, we can evaluate v_{\max} for two different solvents employed for the LPE of KYW:RE layers using a few simple approximations. Initial calculation parameters for both the tungstate $K_2W_2O_7$ and the chloride NaCl–KCl–CsCl solvents are given in Table 3.3.

Table 3.3. Parameters for the calculation of the maximum stable growth rate, v_{\max} , for two different solvents employed for the LPE of KYW:RE thin layers.

Parameter (units)	Symbol	$K_2W_2O_7$ Solvent	NaCl–KCl– CsCl solvent
Temperature (K)	T	1173	823
Solution mass (g)	m_{sn}	30.0	50.0
Solution volume (cm ³)	V	7.0	22.7
Solute mass (g)	m_s	3.46	0.17
Initial solute concentration (g cm ⁻³)	n	0.494	0.0076
Supersaturation	σ	Variable	
Equilibrium solute concentration (g cm ⁻³)	n_e	$n_e = n / (\sigma + 1)$ from eq. (3.6)	
Solution density (g cm ⁻³)	ρ_{sn}	4.3	2.2
Solution viscosity (g cm ⁻¹ s ⁻¹)	η	4.5×10^{-2}	1.1×10^{-2}
Diffusion coefficient (cm ² s ⁻¹)	D	1×10^{-5}	3×10^{-5}
Angular rotation velocity (s ⁻¹)	ω	0.1, 0.2, or 0.3	
Boltzmann constant (J k ⁻¹)	k	1.38×10^{-23}	
Schmidt number	Sc	210	91

Values of T , m_{sn} , V , m_s , n , and ω are taken from a typical LPE experiment (Sections 4.5.1 and 4.6.1), the equilibrium solute concentration n_e is calculated from the given initial solute

concentration n and relative supersaturation σ using equation (3.6). The values ρ_{sn} and η are constant for each solvent (Sections 4.4.1 and 4.4.2). The diffusion coefficient D of different ions in the NaCl-KCl and NaCl-CsCl eutectic solvents lies in the range of $1.76\div 8.08\times 10^{-5}$ and $2.29\div 3.35\times 10^{-5}$ $\text{cm}^2 \text{s}^{-1}$, respectively, at temperatures about 70 K above the solvent melting point [jan82]. Therefore, $D = 3\times 10^{-5}$ $\text{cm}^2 \text{s}^{-1}$ is believed to be a realistic diffusion coefficient for the NaCl-KCl-CsCl solvent at 873 K (70 K above the melting point). The $\text{K}_2\text{W}_2\text{O}_7$ solvent is more dense and viscous, and, hence, the diffusion coefficient should be lower. The average diffusion coefficient $D = 1\times 10^{-5}$ $\text{cm}^2 \text{s}^{-1}$, which is typically accepted for various oxide melts [elw75], is taken for the $\text{K}_2\text{W}_2\text{O}_7$ solvent at 1173 K.

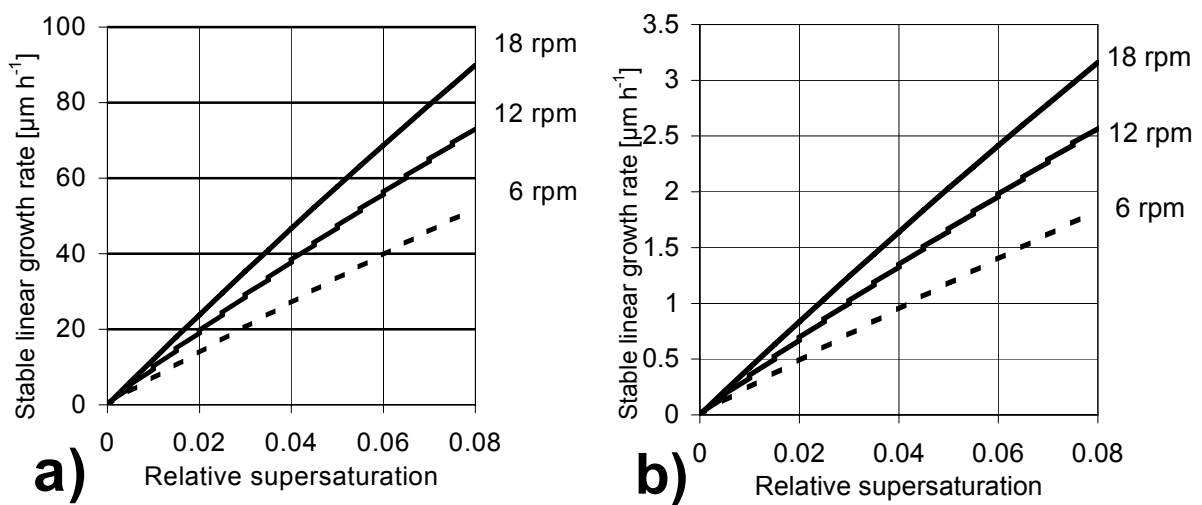


Fig. 3.7. Maximum stable growth rate as a function of supersaturation and rotation rate: (a) $\text{K}_2\text{W}_2\text{O}_7$ solvent and (b) NaCl-KCl-CsCl solvent.

Figure 3.7 shows the dependence of the maximum stable growth rate on the relative supersaturation for three different rotation rates of 0.1, 0.2, and 0.3 s^{-1} , which correspond to 6, 12, and 18 rpm, respectively. The growth rate rises linearly with the relative supersaturation and is proportional to $\omega^{1/2}$. For instance, for a typical rotation rate of 12 rpm and a relative supersaturation of 0.04, the maximum stable growth rate is 38 and $1.3 \mu\text{m h}^{-1}$ for the $\text{K}_2\text{W}_2\text{O}_7$ and NaCl-KCl-CsCl solvents, respectively. It is remarkable that v_{max} for the $\text{K}_2\text{W}_2\text{O}_7$ solvent is about 30 times higher than that for the NaCl-KCl-CsCl solvent, mainly because of the small solubility of KYW in the chloride solvent.

3.6 LPE techniques

According to the solubility diagram described in Sect. 3.2, each LPE process consists of five consecutive steps: heating up the solution above the saturation temperature, homogenizing the liquid, supersaturating the solution via cooling, introducing the substrate, and, finally, removing the substrate from the solution after a growth time t . The typical temperature-time profile applied during the LPE is given in Fig. 3.8.

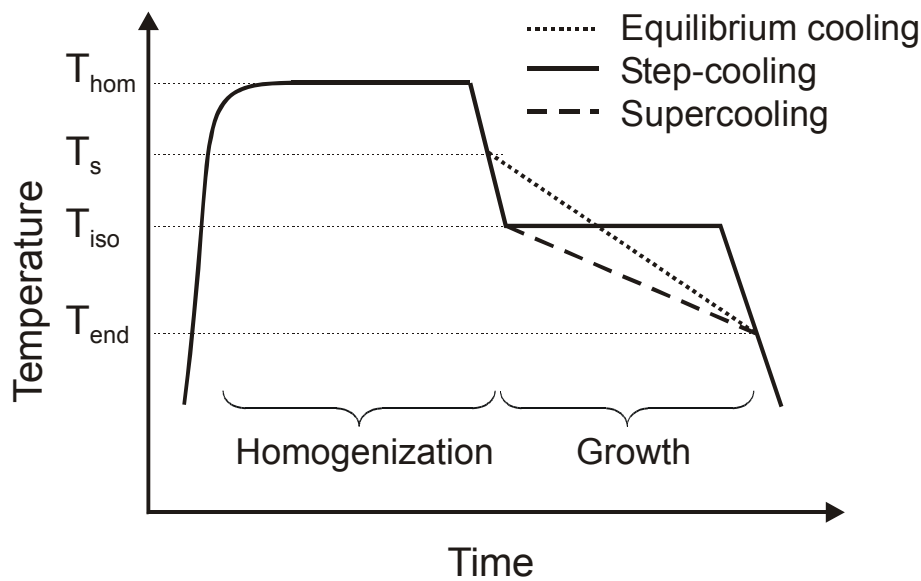


Fig. 3.8. Typical temperature-time profile during LPE

The system is heated up and homogenized at the temperature T_{hom} , which is above the saturation temperature T_s . Then the system is cooled below T_s to obtain the supersaturated solution. Four different types of cooling techniques can be used:

1. *Equilibrium cooling*. The substrate is brought in contact with the saturated solution exactly at the saturation temperature T_s . The system is linearly cooled down and the substrate with the grown layer are withdrawn from the solution at the temperature T_{end} .
2. *Step-cooling* or isothermal growth. After homogenization, the solution is cooled down to T_{iso} , which is below T_s but not low enough for the spontaneous precipitation. The epitaxy takes place from the supersaturated solution kept at the constant temperature T_{iso} .

3. *Supercooling*. The substrate is dipped in the supersaturated solution at T_{iso} but the growth continues under continuous cooling of the system down to T_{end} .
4. *Solid-liquid coexisting solution* (not shown in Fig. 3.8). This technique assumes the same cooling procedure as for the supercooling. However, the temperature is lowered well below T_s to allow the spontaneous solute precipitation to be initiated before dipping the substrate.

All four methods have been tested in this thesis for the growth of KYW:RE layers because each cooling technique has some advantages and disadvantages. The equilibrium cooling allows the layer growth to start at the equilibrium point of the saturated solution, and, hence, a very small supersaturation is achievable when cooling the solution down. However, it requires the precise determination of the saturation temperature T_s for each solute concentration. The step-cooling and supercooling do not require the knowledge of the exact T_s . Furthermore, the initial supercooling increases the driving force for nucleation, causing it to occur more uniformly over the substrate, which results in the growth of smoother layers [hsi74]. The growth from a solid-liquid coexisting solution assumes the presence of deposited solid phase on the bottom/walls of the growth crucible. Therefore, the solution is always saturated with respect to the solute, and a small, near-equilibrium supersaturation is achievable when cooling the solution down. However, the control of layer thickness is reduced for the solid-liquid coexisting solution because part of the “useful” solute material is deposited not on the substrate but on the existing precipitates, which vary in number, size, and location from run to run.

According to their geometrical arrangement, LPE techniques are divided into:

1. *Tipping*. A substrate and a saturated liquid solution lie on opposite ends of a boat-shaped crucible initially tilted with the solution at its lower end. When the growth temperature is reached, the crucible is tipped, causing the solution to flow over and immerse the substrate. Growth terminates when the crucible is tipped to its original position.
2. *Sliding boat*. A substrate is positioned in a machined graphite holder that can slide to contact, in sequence, several wells containing saturated solutions.
3. *Dipping*. A preheated substrate, held in the vertical or horizontal plane, is immersed into the solution for a certain growth time.

The tipping and sliding boat techniques have been extensively used for LPE of semiconductors, where multilayer semiconductor structures have to be grown under an

atmosphere control. The dipping was first introduced in the growth of garnets and further applied for LPE of various oxide layers [rob78]. The dipping technique is simpler and faster than the tipping or sliding. Here, the solution in the crucible is kept in a resistance-heated furnace and the substrate is directly immersed in the supersaturated solution under ambient atmosphere. Therefore, the dipping technique has been employed in this thesis for the LPE of KYW:RE thin layers.

4. LPE of the $\text{KY}(\text{WO}_4)_2\text{:RE}$ layers

This chapter presents experimental results on the LPE of KYW:RE thin layers. A short introduction of the available literature data about the LPE of KYW:RE precedes the main experimental sections. After a description of substrate preparation and experimental set-up, the properties of the ideal solvent for LPE are discussed. With this knowledge, two different solvents, the tungstate $\text{K}_2\text{W}_2\text{O}_7$ and the chloride NaCl-KCl-CsCl , are selected. The growth results are given separately for each solvent. The consideration of microchannel epitaxy from the $\text{K}_2\text{W}_2\text{O}_7$ solvent is given in a separate subchapter due to the novelty and importance of the proposed approach.

4.1 State of the art in LPE of the $\text{KY}(\text{WO}_4)_2\text{:RE}$ layers

Besides the well-established growth of bulk KYW:RE crystals by TSSG, only one reference, which appeared during this thesis work, could be found in the literature regarding the growth of KYW:RE thin layers. In 2004, the Grup de Física i Cristallografia de Materials from the Universitat Rovira i Virgili (Tarragona, Spain) published their work on LPE of the KYW:Yb layers [azn04].

An undoped TSSG-grown KYW single crystal was used as a substrate, and the epitaxial growth took place on all natural faces. The LPE experiments were performed in a vertical furnace with practically no axial gradient to obtain uniform epitaxial layer thickness on every crystal face. The solution was prepared by mixing about 70 g of K_2CO_3 , Y_2O_3 , WO_3 , and Yb_2O_3 in a cylindrical platinum crucible with a 30 mm diameter. The ratio between the solute, $\text{KY}_{0.8}\text{Yb}_{0.2}(\text{WO}_4)_2$, and the solvent, $\text{K}_2\text{W}_2\text{O}_7$, was decreased to 5 mol% as compared to the value for the TSSG (12 mol%) to perform the epitaxial growth at lower temperatures. Once the solution was homogeneous, the saturation temperature, T_{sat} , was accurately determined to be, on average, 820°C. The substrate was introduced slowly into the furnace and maintained above the solution surface for about 30 min in order to reach the thermal equilibrium with the solution. At the beginning of the epitaxial growth, the solution temperature was kept 1°C higher than T_{sat} with the objective to dissolve the outer layer of the crystal. Subsequently, the substrate was dipped into the solution at that temperature for 5 min

and then the temperature was decreased to 2°C below T_{sat} for 4 h in order to grow the epitaxial layer. The crystal rotation velocity was kept constant at 40 rpm. Finally, the crystal was removed from the solution and taken out slowly from the furnace to avoid cracks due to thermal shocks and differences of the thermal expansion coefficients between the layer and the substrate.

The thickness of the epitaxial layers was measured by a scanning electron microscope (SEM) with the sample cut and polished perpendicular to the c crystallographic direction. The growth rate of $12 \mu\text{m h}^{-1}$ resulted in a maximum layer thickness of $48 \mu\text{m}$ for the $\{010\}$ face. There was no essential difference in surface morphology between the different natural faces of the crystal, although the face (010) seemed to be the best. The typical defects were growth steps on all faces. Furthermore, some cracks could be identified on the $\{110\}$ and $\{310\}$ faces. Electron probe microanalyses showed that the Yb content in the layer ($11.96 \times 10^{20} \text{ Yb}^{3+} \text{ ions cm}^{-3}$) was approximately the same as in the solution, while the Yb content in the substrate was zero, even very close to the interface. Thus, the distribution coefficient of Yb^{3+} in these layers grown from the $\text{K}_2\text{W}_2\text{O}_7$ solvent is close to unity.

4.2 Substrate preparation

The substrate material should approximately match the material to be deposited both in lattice parameters and in linear thermal expansion coefficients, otherwise strains are introduced into the films and cracks occur if the mismatch is excessive. In this respect, single crystals of KYW seem to be the optimum substrates for the LPE of KYW:RE layers due to the following reasons. First, the lattice misfit between KYW substrate and KYW:RE layers is small (Table 3.1) and the growth by LPE can be considered as almost homoepitaxial, if a low doping concentration of 1-5 mol% of RE is used. Second, the thermal expansion strain is also relatively low, on the order of 1.4×10^{-5} – 7.0×10^{-5} along the c -crystallographic axis for KYW layers doped with 1-5 mol% of Yb (Sect. 3.3). Finally, the KYW single crystals are quite robust and hard (Sect. 2.1.2). They can be machined to a certain substrate shape and are optically inert, i.e. do not affect the optical properties of active RE-doped layers.

The KYW substrates were obtained mainly from Dr. Nikolay Kuleshov, International Laser Center (Minsk, Belarus). The KYW bulk single crystals were grown from the $\text{K}_2\text{W}_2\text{O}_7$ solvent in a platinum crucible using the TSSG or modified Czochralski method. A pulling rate of 2.8 mm per day resulted in crystals with dimensions up to $15 \times 15 \times 30 \text{ mm}^3$. The crystals were cut with a wire saw into thin rectangular plates oriented perpendicular to the b -

crystallographic axis. The edges were parallel to the crystallographic [001] and [101] directions and formed the characteristic angle of 86° (Fig. 4.1).

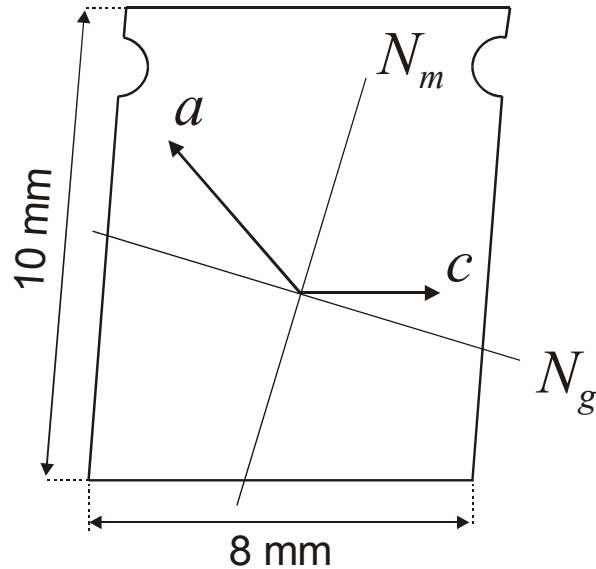


Fig. 4.1. Schematic of the typical KYW substrate used for the LPE of KYW:RE layers.

The selection of the (010) substrate orientation has been conditioned by three main reasons:

1. The highest lattice constant misfit between RE-doped layer and undoped KYW substrate is expected along the b -crystallographic axis (the [010] direction) for almost all RE^{3+} ions, as one can see from Table 3.1. The presence of the [010] direction in the layer plane induces a strong misfit strain, which may lead to fracturing of those KYW layers having high RE concentrations. Therefore, a better choice is to have the [010] direction normal to the substrate surface, whereas the [100] and [001] directions are in the substrate plane. This is possible by using (010) KYW substrates, which also assumes the growth of (010) KYW:RE epitaxial layers.
2. The growth rate for the (010) crystal face is lower and more stable than for the (101) or (001) faces. This ensures lower probability of defect formation in the (010) grown layers.
3. The presence of the a - and c -axes in the (010) layer plane allows us to identify visually the crystallographic and optical directions with respect to the substrate edges.

One side of the (010) substrates was polished to laser grade quality. The laser grade had scratch/dig specification 10/5, which permits a maximum scratch width of $10\ \mu\text{m}$ and a dig/bubble diameter of $50\ \mu\text{m}$. Actually, when inspecting the substrates surface with a

differential-contrast (DIC) microscope, we observed no surface defects but only tiny abrasion traces, which gave a root-mean-square (rms) value of < 1 nm for the surface roughness. The other substrate face was polished only to optical grade quality with a residual rms value of < 30 nm. Obviously, the layer growth took place on both substrate faces. However, only the laser grade polished face was considered to produce high-quality KYW:RE layers.

According to provided specifications, the precision of the (010) substrate orientation was 4 arc minutes. However, the real substrate misorientation could be as high as 20 arc minutes (0.3°), as was observed experimentally by measuring the inclination of the grown (010) terraces with respect to the initial substrate surface.

Two grooves were drilled in the upper part of the substrate using a drill “Micro-Cut” to enable the substrate fixation with a Pt wire clamp (not shown in Fig. 4.1). Afterwards, the substrate was cleaned from dust particles by sonicating it in pure 2-propanol and wiping with lens cleaning paper wetted in dry methanol. Finally, traces of the organic solvents were removed by oxygen plasma treatment (charge power 75-100 W, O_2 pressure 0.3 Torr, duration 20-30 min).

4.3 LPE set-up

Figure 4.2 shows schematically the experimental LPE set-up, modified from a commercial furnace “Carbolite VCF 12/5”. The furnace has a chamber with top-loading, while heating elements are mounted inside the four heat-insulating ceramic walls. The furnace chamber is closed from the bottom and from the top by thick porous alumina ceramics. A ceramic pedestal is constructed from separate pieces on the chamber bottom to raise the crucible position and to diminish thermal losses via the non-heated bottom region. A zirconia (ZrO_2) cup is used to further homogenize the temperature and protect the heating elements from being damaged in case the crucible with molten solution tips over.

The substrate is mounted with 0.3 mm Pt wires attached to an alumina rod. The alumina rod is connected to lifting and rotation motors, which provide the substrate with vertical and axial movements. The length of the Pt wire extension is about 20 cm so that only a small part of the alumina rod penetrates the oven when the substrate is immersed in the solution. This reduces heat losses and does not affect strongly the temperature profile while lowering the substrate towards the solution surface. By illuminating the growth chamber through a quartz rod and observing a typical splash on the liquid surface, one can readily control the exact moment when the substrate is dipped in the solution.

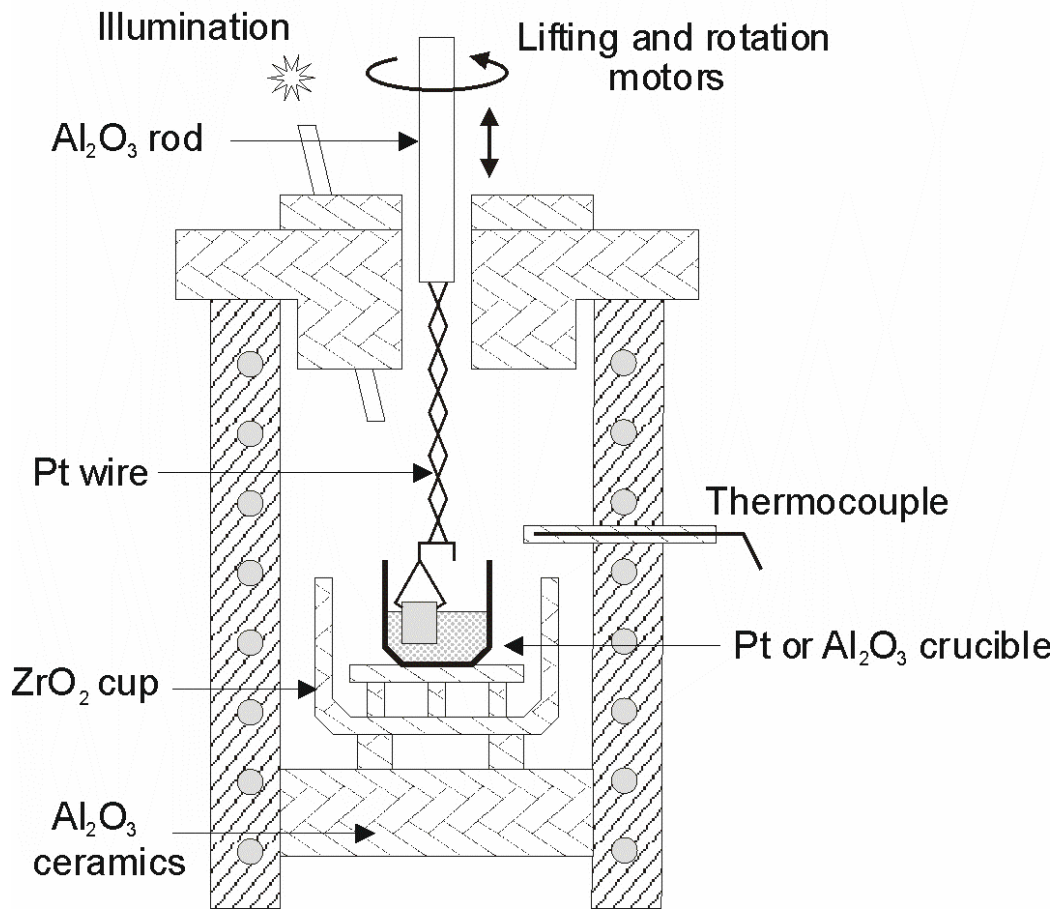


Fig. 4.2. LPE set-up.

The heating elements form a single-zone vertical temperature profile inside the furnace chamber. The height of the ceramic pedestal has been adjusted in order to achieve a small axial thermal gradient in the solution, keeping the bottom at about 1 K hotter than the surface. The radial gradient in the solution is negligible (< 1 K), because the crucible is located in the middle of the oven. The temperature inside the furnace is measured with a R-type thermocouple connected to a temperature controller “Eurotherm 902”. It allows us to control the temperature with the precision of 0.1 K. However, the displayed temperature does not represent the actual temperature inside the liquid solution but only shows the temperature close to the thermocouple tip. Additional temperature measurements with an independent portable thermocouple “Testo 925” having a long probing rod showed that the actual solution temperature differs from that measured by the controller by less than 3 K. To avoid the temperature recalibration for each LPE run, all growth temperatures, which appear in this thesis, represent values given by the furnace temperature controller.

4.4 Choice of solvent

Finding the suitable solvent for a given crystal growth may in some cases represent a real challenge. The optimum choice is a solvent, which is chemically similar (in the type of bonding) to the solute. On the other hand, a suitable solvent should have sufficient crystal-chemical differences with the solute constituents in order to prevent incorporation of inappropriate solvent species into the growing crystal (layer). Ideally, the solvent contains the same cations and anions as the crystal, for example in the growth of the magnetic semiconductor NaCrS_2 from Na_2S_x melts [sch74] or TSSG of KYW from the K_2WO_4 melt [wan90]. The desirable properties of the solvent to be applied in high-temperature solution growth have been summarized in [elw75] and may apply to low temperature processes as well:

1. High solubility for the solute constituents.
2. The crystal phase required should be the only stable solid phase.
3. Appreciable change of solubility with temperature.
4. Low melting point.
5. Low volatility at the highest applied temperatures (except when the solvent evaporation technique is used).
6. Viscosity in the range 1-10 centipoises.
7. Low reactivity with the crucible material.
8. Absence of unwanted elements that might be incorporated into the solute.
9. Ready availability in high purity at low cost.
10. Density appropriate for the mode of growth.
11. Easy separation from the grown crystal by chemical or physical means.
12. Low tendency of the solvent to “creep” out of the crucible.
13. Low toxicity.

There is no solvent that can fulfill all these requirements and a compromise is always necessary. The majority of common solvents employed in the growth of oxides can be divided into the following groups: lead- and bismuth containing compounds (PbO , PbO-PbF_2 , $\text{Bi}_2\text{O}_3, \dots$); borates (B_2O_3 , $\text{Na}_2\text{B}_4\text{O}_7$, $\text{BaB}_2\text{O}_4, \dots$); vanadates (V_2O_5 , NaVO_3, \dots); molybdates and tungstates (Na_2MoO_4 , $\text{K}_2\text{W}_2\text{O}_7, \dots$); halides (LiCl , NaCl , KCl , BaCl_2, \dots); sulphates, phosphates, hydroxides and others (Na_2SO_4 , $\text{Zn}_3(\text{PO}_4)_2$, KOH, \dots).

In this thesis work, two solvents have been selected for the growth of KYW:RE layers: the tungstate $\text{K}_2\text{W}_2\text{O}_7$ and the chloride NaCl-KCl-CsCl solvents. The former solvent

satisfies almost all main requirements for the “ideal” solvent and, therefore, is widely used for the TSSG growth of bulk KYW:RE crystals. First, $K_2W_2O_7$ contains no other ions than required for the KYW crystal growth, which excludes incorporation of any unwanted impurities. Second, it provides a considerably high change in the solubility of KYW with temperature decrease, whereas KYW is the only stable phase to be crystallized from the solution. Finally, the distribution coefficients of the RE^{3+} ions during the KYW:RE crystal growth from $K_2W_2O_7$ are close to unity, which ensures the homogeneous distribution of RE^{3+} ions in the grown KYW:RE layers.

On the other hand, growth temperatures for the tungstate solvent are in the range of 900–1000°C. The high growth temperatures can induce thermal stresses and cracking of heavily RE-doped KYW layers during cooling down because of the thermal expansion mismatch between the active layer and the undoped KYW substrate. This disadvantage may be overcome by using the chloride NaCl–KCl–CsCl solvent, which has a melting point of only 480°C and, thus, offers much lower growth temperatures. The chloride solvent was previously used for the LPE of Mn^{6+} -doped sulfates, molybdates, and tungstates of Ca, Sr, and Ba [roma03, roma04], where the low growth temperatures, below 600°C, were necessary to stabilize the oxidation state of the Mn^{6+} ion. In this work, the NaCl–KCl–CsCl solvent is tested for the growth of heavily-doped KYW:RE thin layers at growth temperatures as low as 520°C, which is favorable in order to decrease the thermal stresses in the layers.

4.4.1 Properties of the $K_2W_2O_7$ solvent

The $K_2W_2O_7$ solvent was used for the first time by Van Uitert and Soden in 1961 to produce KYW:RE crystals for different resonance and emission studies [uit61]. Later on, Klevtsov and Kozeeva [kle69] grew the complete series of KREW (RE = Ce...Lu, and Y) from a stoichiometric mixture of K_2WO_4 and WO_3 corresponding to the $K_2W_2O_7$ composition. Nowadays, the tungstate solvent is widely employed for TSSG of the RE-doped KYW and KGdW laser crystals.

The $K_2W_2O_7$ compound is formed on the K_2O – WO_3 side of the ternary K_2O – Y_2O_3 – WO_3 system. Fig. 4.3 represents the phase diagram of the K_2WO_4 – WO_3 section, which was investigated in [gue70]. Among the four intermediate ternary tungstates that are formed in the binary K_2WO_4 – WO_3 system, $K_2W_2O_7$ has the lowest melting point. $K_2W_2O_7$ melts according to a peritectic reaction at 619°C, which is substantially lower than the melting temperature of 921°C for K_2WO_4 , another solvent employed for the TSSG of KYW crystals (see Sect. 2.1.4).

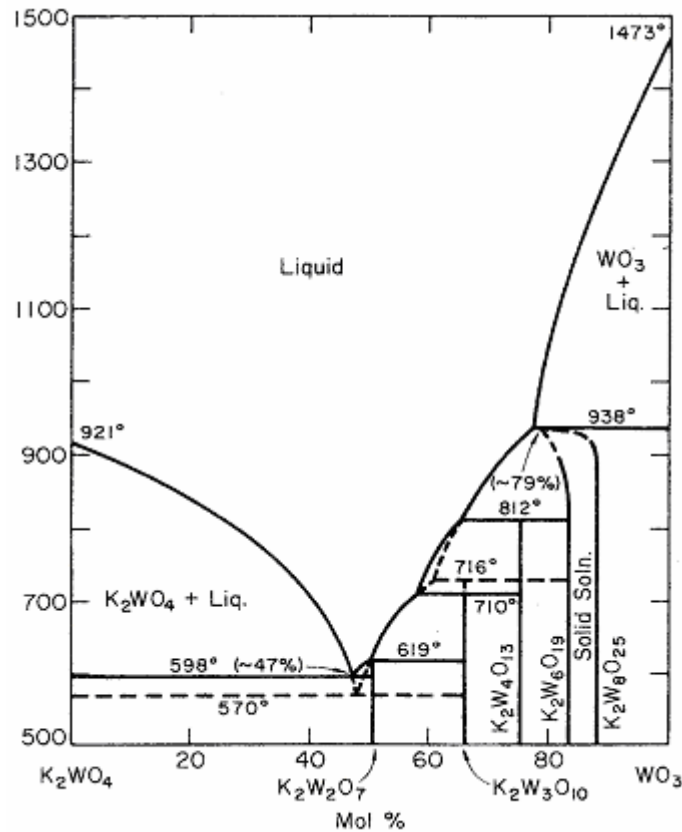


Fig.4.3. Phase diagram of the K_2WO_4 - WO_3 system [gue70].

The solubility of KYW in $K_2W_2O_7$ was examined in [puj99] and the solubility curve can be considered as the liquidus line of the respective binary $K_2W_2O_7$ - $KY(WO_4)_2$ system [gal98]. The solubility increases with increasing temperature and reaches about 25 mol% of KYW at 950°C (Fig. 4.4).

The average crystallization rate calculated from the slope of the solubility curve is about $1.2 \times 10^{-3} \text{ g K}^{-1}$ per g solution for a KYW content of 5–15 mol%, while in the range above 20 mol% of KYW, the crystallization rate increases to about $1.0 \times 10^{-2} \text{ g K}^{-1}$ per g solution. In this work, the KYW concentration in the $K_2W_2O_7$ solvent was 10.5 mol% for most LPE experiments. The selected concentration ensures well-controlled growth conditions together with a reasonable crystallization rate of $3.6 \times 10^{-2} \text{ g K}^{-1}$ for 30 grams of solution. This crystallization rate results in the expected linear growth rate of about $21 \mu\text{m h}^{-1}$ when a $8 \times 8 \times 1 \text{ mm}^3$ substrate is immersed in 30 grams of the saturated solution being cooled down at a speed of 0.6 K h^{-1} . The expected linear growth rate is well below the maximum stable growth rate calculated in Sect. 3.5, and, therefore, inclusion-free growth can be achieved.

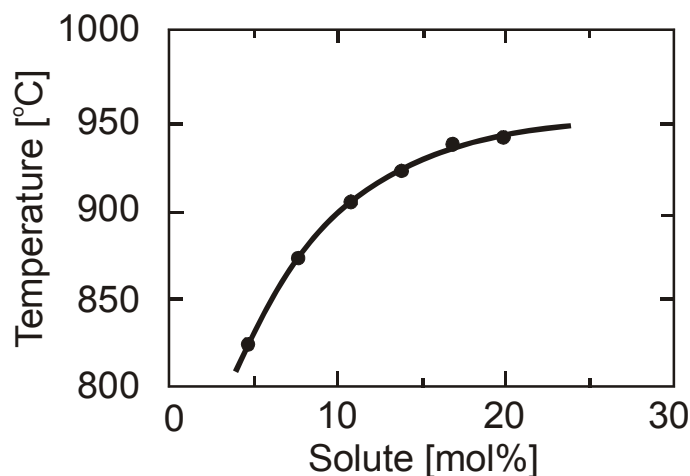


Fig. 4.4. Solubility curve of KYW in the $K_2W_2O_7$ solvent [puj99].

The growth rate is inversely proportional to the solution viscosity. The dynamic viscosity of $K_2W_2O_7$ is $4.5 \text{ cP} = 4.5 \times 10^{-2} \text{ g cm}^{-1} \text{ s}^{-1}$ at 900°C , which is higher than the viscosity of 3.0 cP for the K_2WO_4 solvent at 950°C [elw75]. This is because the viscosity of the molten compound generally increases with the anion (WO_4^{2-}) content. Accordingly, the smaller sizes of the crystals grown by the Bridgeman-Stockbarger method from the $K_2W_2O_7$ solvent compared to those grown from the K_2WO_4 solvent have been explained in [gal00]. From this point of view, the K_2WO_4 seems to be a better choice for the Bridgeman method. Nevertheless, lower growth temperatures and better quality of the grown crystals still favor using the $K_2W_2O_7$ solvent for TSSG and LPE [puj96, azn04].

Since one of the solution components is WO_3 , which is quite volatile above 800°C , there are some evaporation losses of the $K_2W_2O_7$ solvent at the growth temperature. After 4 days of growth at 900°C , the weight loss from 100 g solution was only 1.3 g , which could be neglected [puj96]. However, the losses rapidly increase with increasing temperature and, hence, they can change the initial solute/solvent ratio before the crystal growth is initiated. In order to avoid excessive evaporation, the solution homogenization at the maximum temperature of 50°C above the expected saturation temperature should not last longer than a few hours.

The solvent constituents, K_2CO_3 and WO_3 , are available with purities better than $99.998 \text{ wt}\%$. This reduces incorporation of impurity ions that can affect the structural and optical properties of $KYW:RE$. The WO_3 powder is harmful by inhalation, if swallowed, or in contact with skin (EC Risk and Safety Instructions, R20/21/22-36/37/38, S26-36/37 [jm04]). Therefore, it is imperative to use a ventilation system above the furnace in order to evacuate the WO_3 -containing vapor coming from the solution. The liquid tungstate solvent is quite reactive with respect to a number of crucible materials; it may attack crucibles made of

refractory oxides, like alumina or zirconia, and dissolve the crucible material by forming binary oxide mixtures. Therefore, noble-metal crucibles appear to be the best choice. The solvent “creeping” out of the Pt or Ir crucible is negligible [puj96]. The density of liquid $\text{K}_2\text{W}_2\text{O}_7$ is about 4.3 g cm^{-3} at 900°C .

4.4.2 Properties of the NaCl–KCl–CsCl solvent

The composition of the chloride solvent corresponds to the eutectic point of the respective quasi-ternary NaCl–KCl–CsCl system. Its phase diagram, shown in Fig. 4.5, was investigated using the visual-polythermal method by Il'yasov and Bergman [ily62].

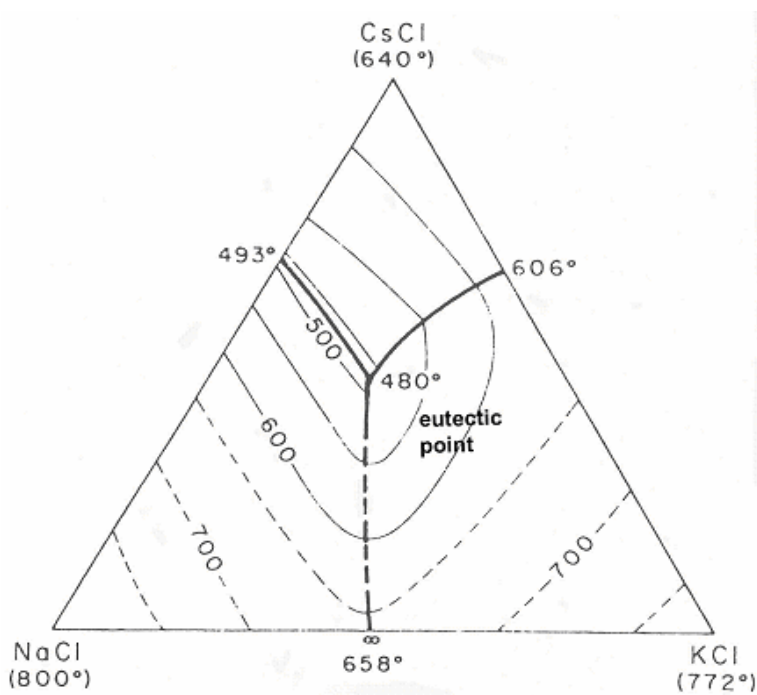


Fig. 4.5. Liquidus surface of the ternary NaCl–KCl–CsCl system [ily62].

The mixture of 30.0 mol% NaCl, 24.5 mol% KCl, and 45.5 mol% CsCl corresponds to the ternary eutectic point with a melting point of 480°C . It is significantly lower than the melting points of the individual chlorides contained in the composition (801°C for NaCl, 771°C for KCl, or 646°C for CsCl [cre00]). Contrary to different LiCl-containing solvents that have even lower crystallization temperatures [ehr02], the NaCl–KCl–CsCl mixture is not hygroscopic and, therefore, can be used in ambient atmosphere. Under the condition of reasonable solubility for a given material, the chloride mixture allows the solute to be crystallized at temperatures of $500\text{--}600^\circ\text{C}$.

The NaCl–KCl–CsCl solvent was first used for an electrolytic investigation of the solubility of Mg, Ba, Ca, Sr, Ni, and Zn oxides [che91]. Later on, Brunold *et al.* successfully employed the chloride solvent for the growth of Mn^{6+} -doped $BaSO_4$ crystals [bru97], where growth temperatures below 620°C were required in order to prevent the formation of MnO_4^{3-} in the solution. The chloride solvent was then thoroughly investigated by Dirk Ehrentraut, who performed his PhD work on the epitaxial growth and optical characterization of $BaSO_4:Mn^{6+}$ at the Institute of Imaging and Applied Optics (EPF Lausanne) [ehr03].

The NaCl–KCl–CsCl solvent was also tested for the growth of Mn^{6+} -doped molybdates and tungstates of Ca, Sr, and Ba [rom04]. Small crystals of tungstates up to 2 mm long were produced by the slow-cooling method with spontaneous nucleation. Furthermore, the first LPE of Mn^{6+} -doped AWO_4 thin layers ($A=Ca, Sr, \text{ or } Ba$) was reported in [roma03], [roma04]. Undoped AXO_4 single crystals served as substrates. Growth velocities of $3\text{--}5\ \mu\text{m/h}$ in the temperature interval from $490\text{--}540^\circ\text{C}$ from the chloride solvent delivered AWO_4 layers up to $200\ \mu\text{m}$ in thickness. Although the layers surface was quite rough due to pronounced step-bunching (Fig. 4.6), the demonstrated possibility to grow thin layers of the tungstate material from the chloride NaCl–KCl–CsCl solvent is a very good prerequisite for the successful growth of $KYW:RE$ layers.

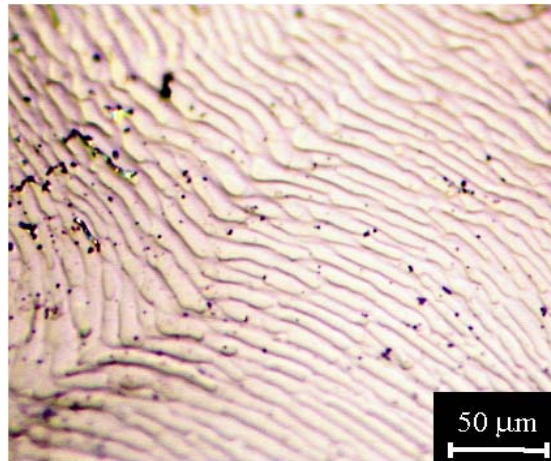


Fig. 4.6. Surface of a $BaWO_4:Mn^{6+}$ thin layer grown from the NaCl–KCl–CsCl solvent by LPE [roma03].

The solubility of KYW in the NaCl–KCl–CsCl solvent is expected to be below 1 mol% at 600°C , in analogy with the solubility of the alkali-earth metal tungstates [rom04]. However, no quantitative data could be found for KYW . In order to establish optimum growth conditions, we investigated the solubility and stability of KYW in the chloride solvent using the dissolution-extraction method.

Chlorides with purities better than 99.997 wt% were dried at 200°C for 20 h and the composition of 30.4, 24.4, and 45.2 mol% of NaCl, KCl, and CsCl, respectively, was thoroughly mixed to be used as the solvent. 50 g of the mixture were filled into an alumina crucible and placed without lid in a resistance-heated furnace. The solvent was heated above the melting point and then kept at a constant temperature of 550°C. Small KYW pieces of 1–5 mm in size were cut from a single-crystal KYW boule, placed onto an alumina holder, and immersed into the solvent. The holder was rotated at slow speed for better homogenization of the solution. The temperature field inside the solution was homogeneous within 1 K. The crystals were removed from the solvent after every 12 h, weighed, and then immersed back.

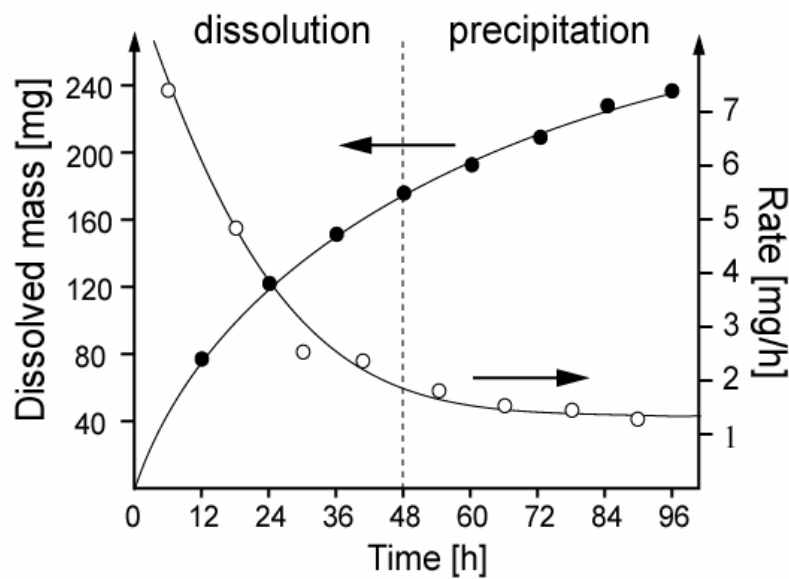
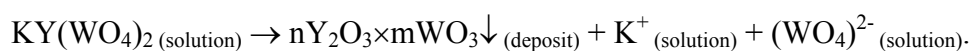


Fig. 4.7. Dissolution of KYW crystals in the NaCl–KCl–CsCl solvent at 550°C.

The temporal evolution of the dissolved crystal mass is shown in Fig. 4.7 together with the calculated average dissolution rate. The total dissolved mass increases gradually with time and the dissolution rate decreases. However, the dissolution rate did not decrease to zero even after 96 h, i.e., dissolution continued. This unusual behavior was provoked by the deposition of dissolved material on the crucible bottom. After quenching the solution, a polycrystalline deposit was found on the bottom, which was identified using powder X-ray diffraction (XRD) as a mixture of yttrium-tungsten oxides, $nY_2O_3 \times mWO_3$, with Y_2WO_6 and $Y_6W_2O_{15}$ as predominant phases. Thus, there is a dynamic equilibrium in the solution, which can be expressed by the following scheme:



The continuous precipitation of yttrium- and tungsten-containing oxides on the bottom of the crucible shifts the equilibrium to the right-hand side in the above scheme, and the conventional determination of KYW solubility versus temperature is, therefore, impossible. The dependence of the dissolution rate versus time presented in Fig. 4.7 can be described by two components. During the initial part (approximately 48 h), an exponential decay of the dissolution rate is dominant, because the solution gradually saturates with KYW. After approximately 48 h, the dissolution rate tends to stabilize at a rate $> 1 \text{ mg h}^{-1}$, because the continuing formation and precipitation of secondary phases removes ions from the saturated solution and, thus, triggers the dissolution of new portions of KYW. Under the assumption that the solution was saturated with respect to KYW after approximately 48 h, the solubility is about 0.34 wt% (0.06 mol%) at 550°C. Since the precipitation of yttrium- and tungsten-containing oxides on the crucible bottom continuously decreases the amount of KYW in the liquid solution, a sufficient concentration of KYW has to be enforced during the whole epitaxial growth. This can be achieved by using LPE from the solid-liquid coexisting solution, which is described in Sect. 3.6.

The chloride solvent has a rather low viscosity at 550°C, which is comparable to the viscosity of $1.1 \text{ cP} = 1.1 \times 10^{-2} \text{ g cm}^{-1} \text{ s}^{-1}$ for the KCl-CsCl eutectic at 775°C [zuc74]. The low dynamic viscosity facilitates bulk convection in the solution and leads to homogeneous distribution of the solute constituents. Individual chlorides of the NaCl-KCl-CsCl solvent possess a low vapor pressure in the temperature interval of 550–600°C. Therefore, the volatility of the ternary mixture is also low, and mass losses of ≈ 0 and $\leq 1 \text{ wt\%}$ at 550 and 600°C, respectively, have been reported [ehr03]. However, the solvent evaporation increases at higher temperatures, which can change the solute/solvent ratio. The density of the liquid solvent is 2.2 g cm^{-3} .

A great advantage of the NaCl-KCl-CsCl solvent is its high solubility in water. The solubility in cold water is 35.7, 34.4, and 162.22 g per 100 ml water for NaCl, KCl, and CsCl, respectively [crc00]. Thus, the solvent residuals remaining on the grown layer surface can be easily removed just by rinsing the surface with cold water. On the other hand, the high solubility implies that chloride powders absorb water from the air. Therefore, the initial chloride powders have to be dried at 150–200°C before preparing the solution charge in order to diminish weighing errors and to avoid unwanted hydrolysis reactions. The molten chlorides are quite reactive at elevated temperatures. In particular, they can corrode metal crucibles with the formation of stable anion complexes, e.g. $[\text{PtCl}_6]^{2-}$. In this sense, alumina or zirconia crucibles seem to be the optimum choice. The molten chlorides or their water solutions are not as harmful to human health and environment as the tungstate compound (EC Risk and

Safety Instructions, R36/37/38, S26-36 [jm04]). Still, a ventilation system to evacuate the chloride vapors is required, because the chlorides are irritative to eyes, respiratory system, and skin. The chlorides are available in purities better than 99.997 wt%.

4.5 LPE from the $K_2W_2O_7$ solvent

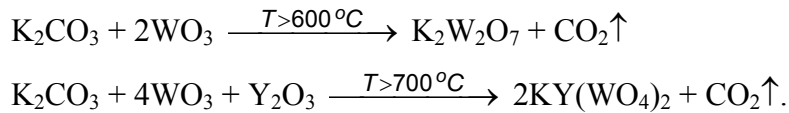
4.5.1 Experimental conditions

For the LPE of KYW:RE layers from the $K_2W_2O_7$ solvent, we employed the vertical dipping technique keeping the substrate only partially immersed in the liquid solution. This approach has been chosen because of two main reasons. First, preliminary test experiments showed that if a Pt clamp fixing the substrate is immersed in the liquid, the substrate always cracks in the places that are in contact with the Pt wire. This occurs because of thermal shocks induced by the huge difference in thermal conductivities of KYW and Pt. When dipping the substrate only partially, the Pt wires stay above the liquid level and no substrate cracking is observed. Second, the non-immersed part of the substrate does not exhibit any layer growth but only local surface contamination due to the solution evaporation. Therefore, the uncovered surface can be used as a reference plane to measure precisely the layer thickness, and, what is most important, to orient the substrate during the surface polishing (Sect. 6.2).

Fine powders of K_2CO_3 , WO_3 , Y_2O_3 and RE_2O_3 from Alfa Aesar [jm04] were used to prepare the initial solution. The purity of chemicals has been chosen as a compromise between the high cost for extremely pure substances and the minimum required quality. For the preparation of the high-quality KYW:RE layers for optical applications, the purity was always better than 4N: K_2CO_3 – 99.997 wt%, WO_3 – 99.998 wt%, Y_2O_3 – 99.999 wt%, and RE_2O_3 – 99.999 wt%. The main impurities were: Na (6 ppm) in K_2CO_3 as detected by inductively coupled plasma/atomic absorption, and Mo (100 ppm), Al (0.2 ppm), Ca (0.5 ppm), Fe (2 ppm) and Mg (0.2 ppm) in WO_3 as detected by d.c. arc emission spectroscopy. To establish optimum growth conditions or to observe growth stages, the highest purity was not necessary and reagent (ACS) grade chemicals could be used: K_2CO_3 – 99.0 wt% and WO_3 – 99.8 wt%.

The main solution components, K_2CO_3 , WO_3 , and Y_2O_3 , were weighed using “Mettler PM” balances with the precision of ± 1 mg, and the dopant RE_2O_3 was weighed using “Mettler AT” balances with the precision of $\pm 1 \times 10^{-2}$ mg. The weighed powders constituted the solution containing 10.5 mol% KYW and 89.5 mol% $K_2W_2O_7$. The concentration of RE with respect to Y varied from 0.2 to 3 mol% for Yb, 0.2-2.5 mol% for Er, or 0.7-1.2 mol% for

Tm. The powders, weighting about 30 g, were thoroughly mixed in a plastic box and transferred to a conical Pt crucible, 27 cm³ in volume, with 0.2-mm thick walls. The charged crucible was placed in the furnace and immediately heated up at a rate of 120 K h⁻¹. The heating ramp included 30-minute dwelling steps at 700 and 850°C to complete the solid-state reactions:



The melting process was completed at the maximum temperature of 950°C and the level of the formed liquid solution was about 13 mm above the crucible bottom. The liquid was homogenized for 6 hours by maintaining the temperature of 950°C, which is about 50 K above the expected saturation temperature. The saturation temperature was accurately determined by dipping a dummy KYW crystal in the solution kept at constant temperature and by observing growth/dissolution of the crystal surface at different temperatures. The obtained value of T_{sat} was about 898°C for the solute concentration of 10.5 mol%, which is in agreement with the solubility curve of KYW in K₂W₂O₇, depicted in Fig. 4.4. After the homogenization, the solution was cooled down at a rate of 15 K h⁻¹ to 910°C and then at a rate of 4.2 K h⁻¹ to 898°C without any dwelling steps. The substrate, clamped in the vertical position with the Pt wires on the alumina rod, was introduced in the furnace about 30 minutes before the solution reached the saturation temperature and was slowly (1-2 cm min⁻¹) moved down to approach the solution surface. Thus, the substrate remained less than 30 minutes above the solution, which reduced the exposure of the substrate surface to harmful vapors. In some test experiments, while the substrate was kept above the solution during the whole heating/homogenization period (24 hours), the laser-grade surface quality degraded because of the long-term exposure to the solution vapors. In that case, we observed some trapped etching defects at the substrate/layer interface.

After reaching the thermal equilibrium with the solution, the substrate was partially immersed in the liquid without dipping the Pt clamp. The equilibrium dipping technique described in Sect. 3.6 was employed for the growth of high-quality KYW:RE layers. The substrate was put in contact with the solution exactly at the saturation temperature or 0.3-0.5 K above the expected saturation. This led to the dissolution of the outer layer of the substrate surface and to the elimination of surface defects introduced during substrate polishing. The solution was then cooled down at a rate of 0.6 K h⁻¹ and the KYW:RE layer

growth lasted for 2–5 hours. The substrate was continuously rotated around the crucible axis at a rate of 10–12 rpm, keeping the laser-grade polished face as the “front” side. Afterwards, the substrate was slowly (5 mm min^{-1}) withdrawn from the solution and was parked at 10 mm above the liquid level. Finally, the whole system was cooled at a rate of $25\text{--}50 \text{ K h}^{-1}$ to room temperature.

All grown layers were catalogued, containing the surface picture and the thickness measured with a profilometer “Alfa-Step”. Fig. 4.8 shows a typical composite differential-interference contrast (DIC) photograph of an as-grown 1.8 mol%Yb:KYW layer.

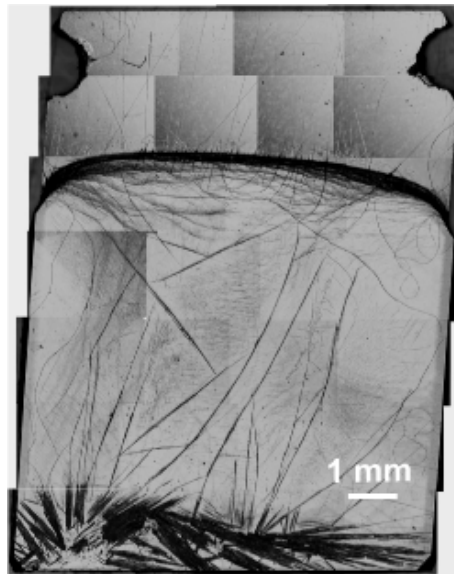


Fig. 4.8. DIC mapping of a 35- μm thick 1.8 mol% Yb^{3+} :KYW layer on a KYW substrate.

The layer has sharp edges matching the initial substrate edges parallel to the crystallographic directions. The black lines on the layer surface are solution residuals that got stuck to the surface when the substrate was being slowly removed from the solution. Their density increases at the substrate bottom, where the last droplet of the liquid solution remained because of surface tension. However, these solution residuals can be easily removed from the surface after a few laps on the polishing tissue.

4.5.2 Growth mode

The KYW:RE growth starts with the layer nucleation on the KYW surface. As discussed in Sect. 4.2, the KYW substrate is slightly misoriented after cutting and polishing. Thus, the

substrate surface contains initial steps and polishing traces, which serve as growth kinks and facilitate the nucleation.

In order to study the layer nucleation in detail, a very thin 1.8 mol%Yb:KYW layer was grown using the step-cooling technique. The substrate was dipped at 897°C , which is below T_{sat} , and the temperature was kept constant during growth. The small initial supercooling assured immediate growth of the layer and avoided any surface dissolution. After 1 minute of the growth, the layer thickness was only $0.5\text{--}1\ \mu\text{m}$, which allowed initial stages of the layer growth to be observed.

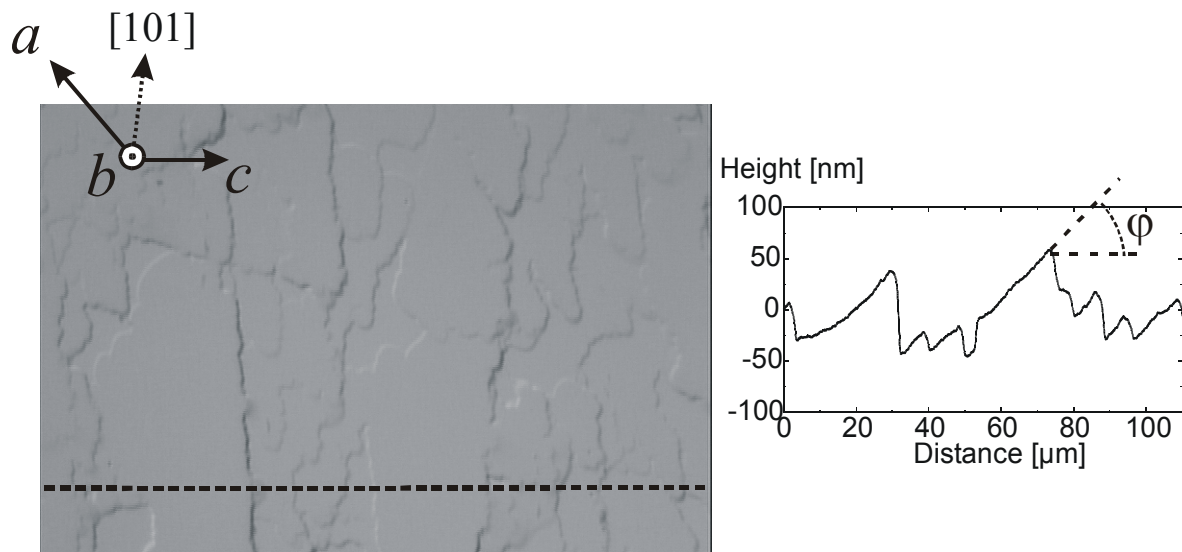


Fig. 4.9. Nucleation of a KYW:Yb layer on the misoriented KYW substrate.

The surface was investigated using a ZEISS microscope with a differential-interference contrast (DIC) attachment. Fig. 4.9 shows the DIC photo of the $0.5\text{-}\mu\text{m}$ thin KYW:Yb layer. Growth steps of typically $20\text{--}100\ \text{nm}$ in height, which alternate with almost atomically flat terraces, cover the surface. The plane terraces are inclined with respect to the substrate surface at $\varphi = 0.20^\circ$. This unambiguously indicates the step-bunching mechanism, in which the growth steps are bunched to compensate the considerable substrate misorientation. On the other hand, the layer nucleation takes place simultaneously on the entire substrate surface immersed in the solution. This suggests high wettability of the KYW:RE layer on the KYW substrate in the $K_2W_2O_7$ solution, and indicates that, in principle, the Frank-van der Merwe (FVM) mode is achievable on perfectly oriented substrates.

The layer grows normally to the substrate surface because of continuous movement of the step bunches along the surface and because of slow rise of the interstep terraces. Some terraces are a few hundreds μm in width, with almost atomically flat surfaces (Fig. 4.10).

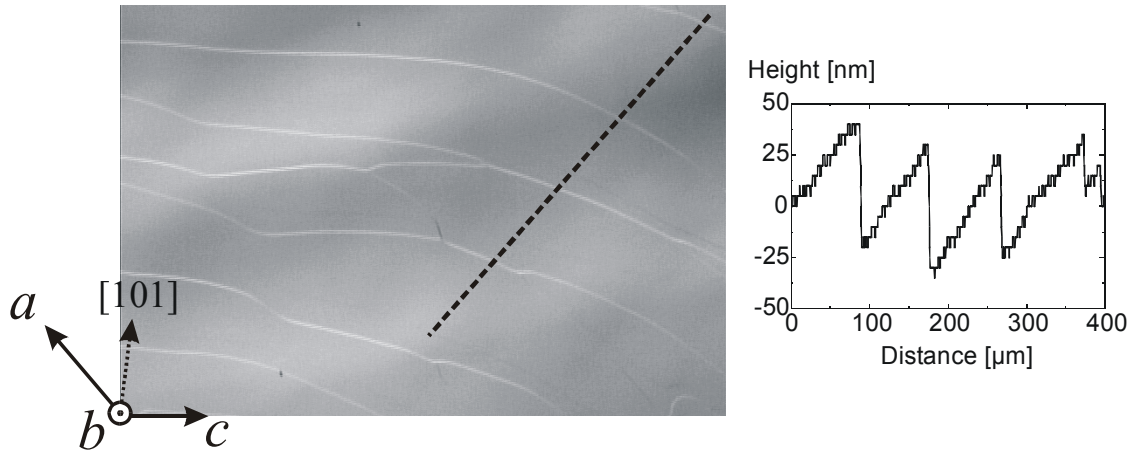


Fig. 4.10. Step bunches alternating with wide flat terraces on the surface of a 1.8 mol% Yb: KYW layer.

The initial steps on the misoriented substrate surface are not the only possible nucleation centers. Screw dislocations and twin planes present in the KYW substrate can also serve as the dominant nucleation centers. Fig. 4.11 shows a semi-conical growth hillock originating from the dislocation step source located at the hillock apex.

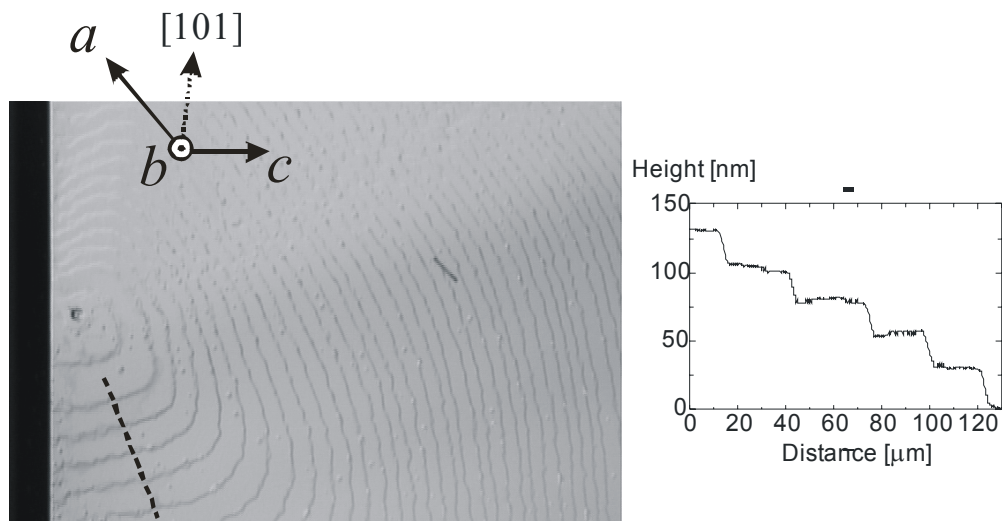


Fig. 4.11. Growth hillock originating from the dislocation source at the edge of a 1.8 mol% Yb:KYW layer

The hillock is covered by macrosteps, which are located more densely in the direction of the highest substrate misorientation. The formation of the growth hillocks is particularly typical for the corners and edges of the substrate, where the solution flow is enriched with solute material, as will be discussed in Sect. 4.5.3.

Assuming that the growth hillock in Fig. 4.11 is a macrospiral originating from a single screw dislocation, one can calculate the approximate solution supersaturation. The mean interstep distance is about 26 μm and the mean step height is 27 nm. The interstep distance is calculated along the direction which is perpendicular to the maximum substrate misorientation. Thus, we exclude the reduction of interstep distances, which is necessary to compensate the substrate misorientation. Inserting $L_{\text{sol}} = 127.5 \text{ kJ mol}^{-1}$, $y_0 = 26 \mu\text{m}$, $h = 27 \text{ nm}$, $\varepsilon = 1$, and $T = 1173$ into equation (3.7), the respective relative supersaturation $\sigma = 0.042$.

The observed linear growth rate was $18.5 \mu\text{m h}^{-1}$ for the rotation rate of 12 rpm and the equilibrium cooling rate of 0.6 K h^{-1} . This resulted in a layer thickness of 20–100 μm after 2–5 hours of growth. The observed growth rate is close to the expected value of $21 \mu\text{m h}^{-1}$ calculated from the slope of the KYW solubility curve in $\text{K}_2\text{W}_2\text{O}_7$ (Sect.3.2). Furthermore, the value of $18.5 \mu\text{m h}^{-1}$ is well below the maximum stable growth rate of $38 \mu\text{m h}^{-1}$ estimated from Fig. 3.7 for the rotation rate of 12 rpm. Therefore, the layer growth is stable and uniform, without inclusions of the mother solution.

The observed growth rates were similar for all investigated KYW:RE layers, because the presence of a small amount of dopant (e.g. 0.2-3 mol% Yb with respect to Y) does not change the nucleation and development of the layers. The maximum Yb concentration of 3 mol% in the KYW:Yb layer corresponds to a lattice misfit of 2×10^{-4} . This value does not exceed the critical lattice misfit $f = 7 \times 10^{-4}$ estimated for a crack-free, 50- μm thick layer from Fig. 3.5. Therefore, most of the grown KYW:RE layers having a thickness of 30–80 μm were crack-free. However, for very thick ($> 80 \mu\text{m}$) layers, some cracks could be detected at the near-edge regions. It is likely that the cracks appeared because the substrate edges were not polished and the growth was generally more rapid and less stable along the edges.

Several KYW:RE layers were overgrown by undoped KYW overlays in order to obtain buried active structures. For doing so, the surface of KYW:RE layers was polished to remove solution residuals and growth steps, as will be described in Sect. 6.2. The undoped overlay was grown using the equilibrium or supercooling technique in order to avoid the partial dissolution of the active layer. The experimental conditions were the same as for the LPE of RE-doped layers, except that the substrate was immersed in the solution so that 0.5 mm of the RE-doped layer was not covered with the overlay. That facilitated the determination of the overlay thickness, which was typically 20-30 μm .

4.5.3 Simulation of liquid flow

Besides the step bunches that are hardly visible in Fig. 4.8, large-area growth hillocks can be seen on the layer surface. As measured with a profilometer, they were sometimes 10-20 μm higher than the average layer thickness. Moreover, the position of hillocks on the layer surface depend on the substrate rotation rate. This observation could be reproduced for a series of layers grown at the same rotation rate.

In order to investigate how the substrate rotation influences the layer thickness profile and to predict the optimum rotation rate, a simulation of liquid flow in proximity to the substrate surface has been performed. The numerical simulation was done by Dr. Lev Kuandykov from Ioffe Physico-Technical Institute (Russia) using the CFD-ACE+ software package.

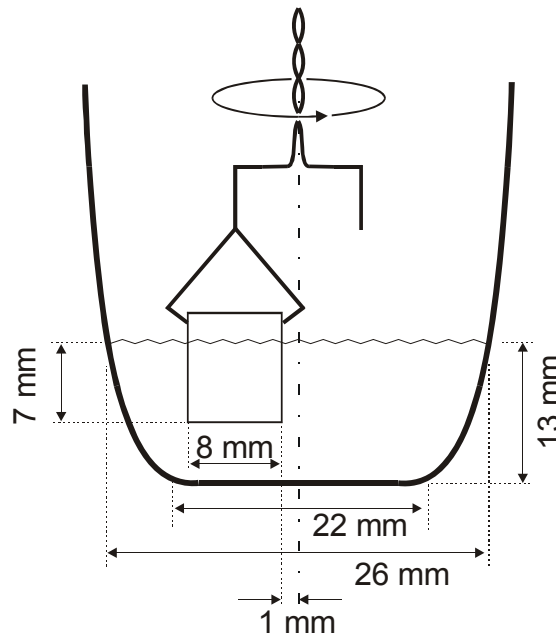


Fig. 4.12. Model of the LPE experiment: crucible filled with liquid solution, and substrate partially immersed in the liquid. The substrate rotation is off-axis.

A crucible filled with the liquid solution, and a substrate partially immersed in the liquid, are considered as a model system. (Fig. 4.12). The system dimensions are as close as possible to those in the real LPE experiment: inner crucible diameter at the bottom – 22 mm, the diameter of the liquid surface – 26 mm, and the level of the liquid is at 13 mm. The immersed part of the substrate is assumed to be rectangular with dimensions $7 \times 8 \times 1 \text{ mm}^3$. The substrate is shifted from the center and its inner edge is located at 1 mm from the central crucible axis; the

substrate is rotated around the central axis so that the laser-grade polished face is always parallel to the crucible radius; the substrate always remains in the vertical position when rotating; and an isothermal system is assumed.

The flow of liquid can be either laminar (the viscous effect is more significant than the inertia effect) or turbulent (the inertia effect is larger). The flow type can be evaluated by calculating the Reynolds number, which is proportional to inertial force divided by viscous force:

$$N_{\text{Re}} = \frac{uL\rho}{\eta}. \quad (4.1)$$

Here, u is the linear flow velocity, L is the substrate length, ρ is the liquid density, and η is the dynamic liquid viscosity. The flow is assumed to be laminar if $N_{\text{Re}} < 10^4$ and turbulent if $N_{\text{Re}} > 10^4$ [ros79]. Using $u \approx 0.5 \text{ cm s}^{-1}$ ($\omega = 0.2 \text{ s}^{-1}$), $L = 0.8 \text{ cm}$, $\rho_{\text{sn}} = 4.3 \text{ g cm}^{-3}$, and $\eta = 4.5 \times 10^{-2} \text{ g cm}^{-1} \text{ s}^{-1}$ for the diluted solution of KYW in K₂W₂O₇, the calculated Reynolds number $N_{\text{Re}} = 38 < 10^4$. Therefore, the laminar flow approximation can be applied to our solution. The laminar flow is stationary, i.e., the flow velocity and its direction are constant for a given point near the substrate surface.

The liquid flow in proximity to the substrate surface has been visualized by projecting the direction and velocity of the fluid on a vertical plane, which is located at 0.01 cm away from the front face towards the observer. The distance of 0.01 cm is within the thickness of the stationary boundary layer, which is about 0.036 cm for a rotation rate of 12 rpm (Sect. 3.5). The projection of the liquid flow is illustrated in the left column of Fig. 4.13 for three different rotation rates: 5, 10, and 20 rpm. Only the immersed part of the substrate is shown with the left side being the outer edge of the rotating substrate.

The simulated flow patterns were compared with thickness profiles of the grown layers. For doing so, a series of three undoped KYW layers was grown at three different rotation rates of 5, 10, and 20 rpm, keeping the other growth parameters unchanged. The supercooling technique with a dipping temperature of 897.0°C and a cooling rate of 0.6 K h⁻¹ was employed to ensure the immediate layer growth and obtain comparable layer thicknesses for different rotation rates. The thickness of as-grown layers was measured with a profilometer and plotted as contoured 3D profiles in the right column of Fig. 4.13.

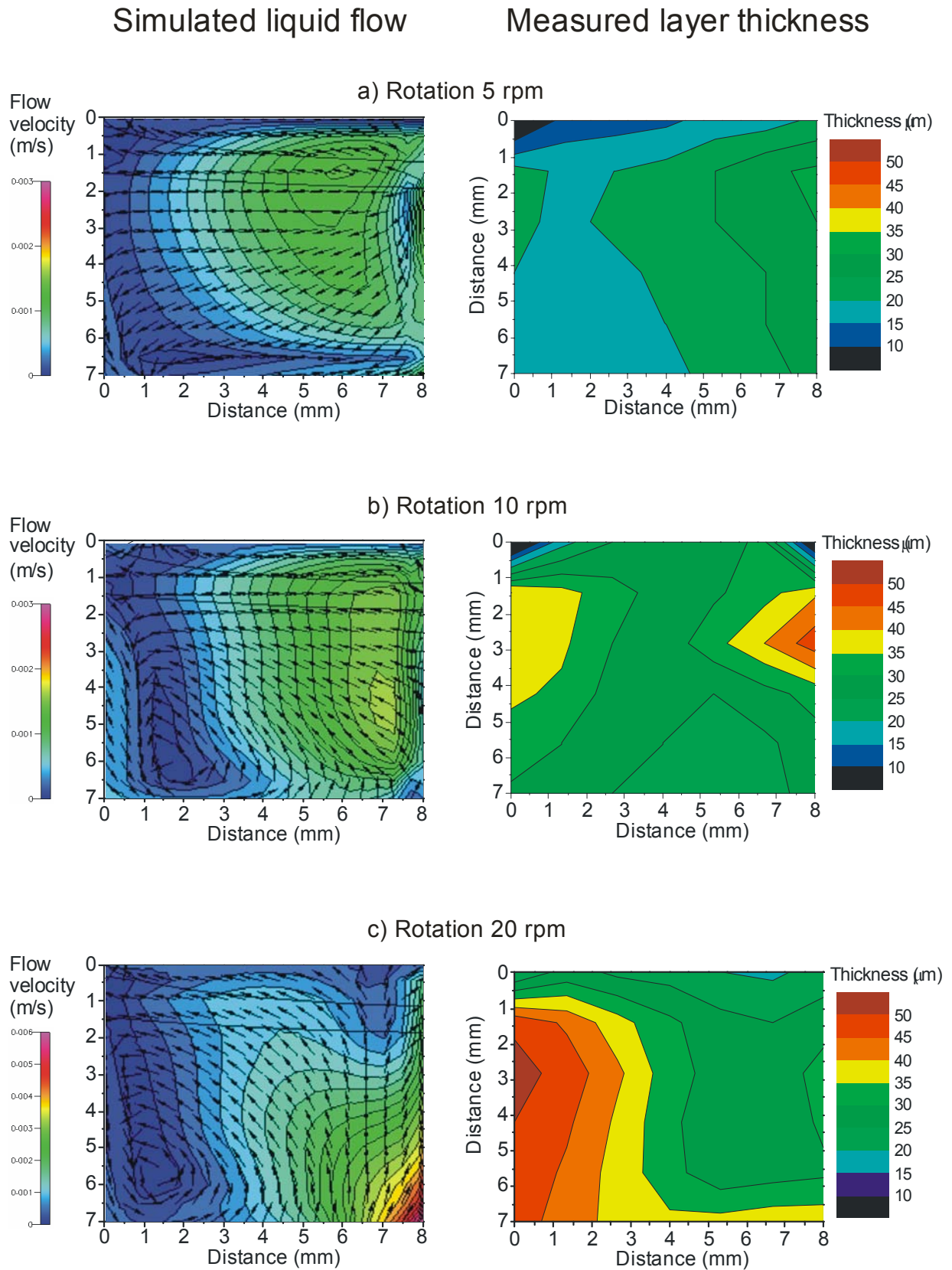


Fig. 4.13. Simulated liquid flows (left column) and observed layer thicknesses (right column) for rotation rates of a) 5 rpm, b) 10 rpm, and c) 20 rpm.

Comparing simulated flow patterns and corresponding thickness profiles in Fig. 4.13, we can see that the positions of the thickness maxima do not correlate with areas of the maximal flow velocity. In turn, the thickness maxima appear exactly in the places where the solution flow enters the substrate surface, i.e., they depend on the liquid flow direction:

- at 5 rpm, the flow enters the substrate surface at the upper right corner and then passes uniformly to the outer edge. On the corresponding layer thickness profile, there is a maximum in the upper right corner and then the thickness decreases gradually towards the left side;
- at 10 rpm, the flow enters the surface at the middle of the inner substrate edge as well as at the middle of the opposite edge. This gives rise to the existence of two maxima on the thickness profile: one on the right side and the other on the left;
- at 20 rpm, the main flow enters the surface from the bottom, creating a pronounced circular flow at the left edge of the substrate. Consequently, the layer is thicker near the bottom and outer substrate edge.

The above relationship can be explained in the following way. The maximum growth rates are observed in places where the fresh solution flow, enriched with the KYW solute, touches the substrate surface. A suitable dislocation step source located at the edge of the substrate receives the solute excess and develops into the large hillock. The hillock slope is covered by trains of step bunches propagating away from the hillock apex. This is in good agreement with observations made by Chernov [che04]: if the flow direction coincides with the direction of growth step propagation on a slightly misoriented substrate, pronounced step bunching is observed. Passing along the hillock slope, the solution loses the KYW solute and becomes depleted. Consequently, the growth rate is reduced at the foot of the hillock, which results in a thinner layer in the center of the substrate.

The thickness nonuniformity is an intrinsic problem of the vertical dipping technique with rotating substrate. However, the substrate rotation cannot be avoided because in the case of a motionless substrate the growth takes places mainly on the substrate edges and a big hopper is usually observed at the center of the layer. Therefore, the rotation rate of 10-12 rpm was used for most LPE experiments as the best compromise between the acceptable layer uniformity on the one hand, and the effective solution homogenization, on the other.

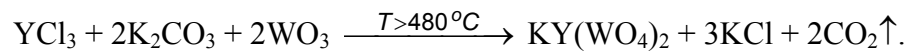
4.6 LPE from the NaCl–KCl–CsCl solvent

4.6.1 Experimental conditions

Since the precipitation of yttrium- and tungsten-containing oxides on the crucible bottom continuously decreases the amount of KYW dissolved in the NaCl–KCl–CsCl solvent, a sufficient concentration of KYW has to be enforced during the whole epitaxial growth. That was achieved by LPE from a solid-liquid coexisting solution. The solid KYW phase on the crucible bottom was formed by adding an excess of the solute to the growth solution.

High-purity chemicals from Alfa Aesar [jm04] were used to prepare the chloride solvent: NaCl – 99.999 wt%, KCl – 99.997 wt%, and CsCl – 99.999 wt%. As detected by d.c. arc emission spectroscopy, the main impurities were: Ba (1 ppm), K (4 ppm), and Zn (< 1 ppm) in NaCl and Na (1 ppm) in KCl. The chlorides were dried at 200°C for 20 hours and the eutectic composition of 30.4, 24.4, and 45.2 mol% of NaCl, KCl, and CsCl, respectively, was thoroughly mixed to be used as a solvent.

KYW was introduced as a stoichiometric mixture of YCl₃, K₂CO₃, and WO₃, which form KYW in the liquid solution according to the chemical reaction



The purity of the solute components was: YCl₃ – 99.99 wt%, K₂CO₃ – 99.997 wt%, and WO₃ – 99.998 wt%. The weight of the solute components was equivalent to 1-5 wt% of KYW with respect to the solution mass.

Doping ions Tb³⁺, Dy³⁺, and/or Yb³⁺ were introduced as respective chlorides with the purity of 4N: TbCl₃ – 99.98 wt% (REO), DyCl₃ – 99.98 wt% (REO), and YbCl₃ – 99.99 wt% (REO). The dopant concentration varied from 0.5 to 10 mol% for Tb or Dy, and from 2 to 100 mol% for Yb with respect to the Y content.

The solute components were thoroughly mixed in nitrogen atmosphere with the dried eutectic mixture of chlorides to prepare an initial charge of 50 g. The charge was heated in an alumina crucible under ambient atmosphere at a rate of 90 K h⁻¹ to 550°C. At that temperature, the solution was homogenized for 6 h. Naturally, not the whole amount of KYW could be dissolved in the solvent at 550°C, and an undissolved crystalline deposit was present on the crucible bottom. The deposit contained KYW as a primary phase with an admixture of the above described yttrium-tungsten oxides. Therefore, the solid-liquid co-existing solution

was always saturated with respect to KYW because of continuous feeding of the solution with the solute material due to the presence of solid KYW deposit on the bottom.

A *b*-oriented KYW substrate of $10 \times 5 \times 2 \text{ mm}^3$ had both sides polished to laser grade quality. The substrate was mounted in a vertical position with Pt-wires on an alumina rod and placed above the crucible. After homogenizing the solution, a continuous cooling rate of 0.67 K h^{-1} was applied and the substrate was immediately immersed into the liquid. The LPE growth lasted for 24-30 h and the substrate was rotated at 15-20 rpm. By applying a cooling ramp, a supersaturation was achieved and KYW:RE layers could be grown from the solid-liquid coexisting solution. The presence of the secondary phases $nY_2O_3 \times mWO_3$ certainly complicates the equilibrium in the solution. Nevertheless, the layer growth is possible, because a close-to-homoepitaxial growth of KYW:RE layers on KYW substrates is energetically favored due to close lattice fit.

After the growth, the layers were slowly withdrawn from the solution but kept inside the furnace. The system was cooled down to room temperature within 24 h. Since the chloride solvent is highly soluble in water, solvent droplets were easily removed from the layer surface by rinsing with distilled water.

4.6.2 Growth mode

Typically, the growth starts with the nucleation of 3-dimensional (3D) islands on the substrate surface. The islands possess a habit of rectangular platelets as shown in Fig. 4.14. Sharp edges are parallel to the *c*-crystallographic axis and the $[101]$ direction and they form the characteristic angle of 86° .

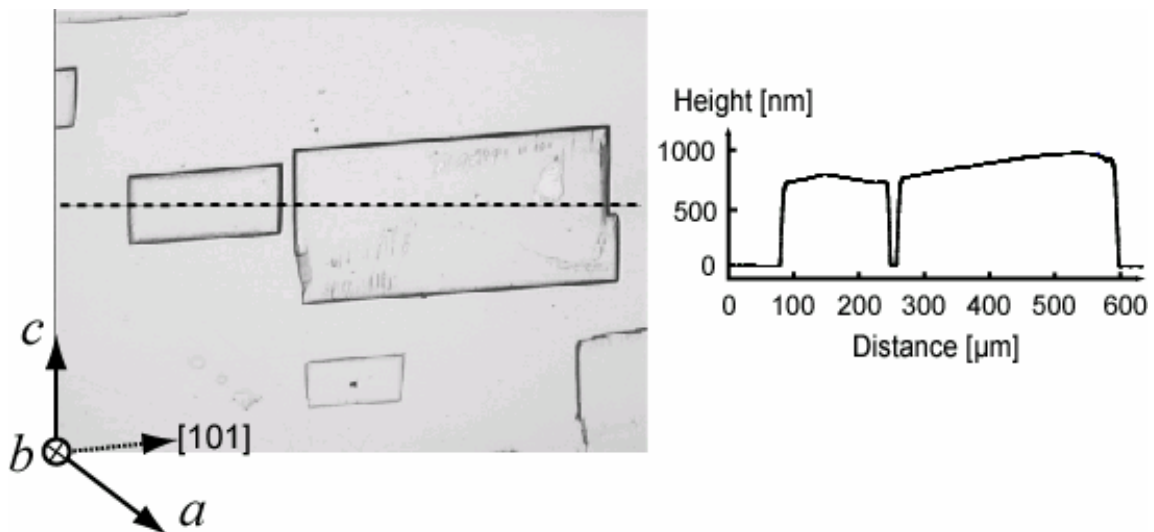


Fig. 4.14. Nucleation and growth of individual 3D islands for 10 mol%Yb:KYW.

The observed 3D nucleation is also known as the Volmer-Weber growth mode described in Sect. 3.4. This mechanism occurs typically when the interfacial energy between layer and substrate is considerable, i.e. for large lattice misfit, and when the substrate surface energy is lower than the layer surface energy. Both arguments do not apply to our epitaxy, because the 3D nucleation is observed for RE-ion concentrations even lower than 10 mol% with respect to Y (misfit $\leq 1 \times 10^{-3}$), although we considered the growth as almost homoepitaxial.

The pronounced 3D nucleation is attributed to the low concentration of active nucleation centers, to the formation of parasitic phases, and to the low volume diffusion of the solute:

- Although misorientation steps and tiny polishing traces cover the whole substrate surface and can serve as suitable nucleation centers, only a few layer islands are nucleated. This indicates that the substrate surface is deactivated, and most of the initial steps are blocked from continuing their development. A possible explanation of the surface deactivation is the presence of impurity ions coming from the solvent. Thus, Na^+ , Cs^+ , Cl^+ , and probably CO_3^{2-} ions bind to the substrate surface and inhibit the attachment of solute particles. Therefore, the nucleation of the KYW:RE layer takes place only on the most energetically favorable sites, e.g. along deep polishing traces, as was observed experimentally.
- Existing small nuclei can be dissolved and transformed into parasitic tungstate phases, because KYW is not the only stable phase in the NaCl–KCl–CsCl solution.
- The solubility of KYW in the NaCl–KCl–CsCl solvent is about 0.06 mol%, and, hence, the volume diffusion of the solute material to the substrate surface is low. Naturally, a few already existing 3D islands assimilate most of the fresh solute material and delay the development of new nuclei.

The islands gradually increase in size and after a certain growth time start to coalesce into a continuous layer (Fig. 4.15). Since the islands are up to 1 μm in height, their coalescence is accompanied by the insertion of defects at the island-island edges. Obviously, these insertion defects increase the probability of crack formation and induce additional scattering centers in the active layer.

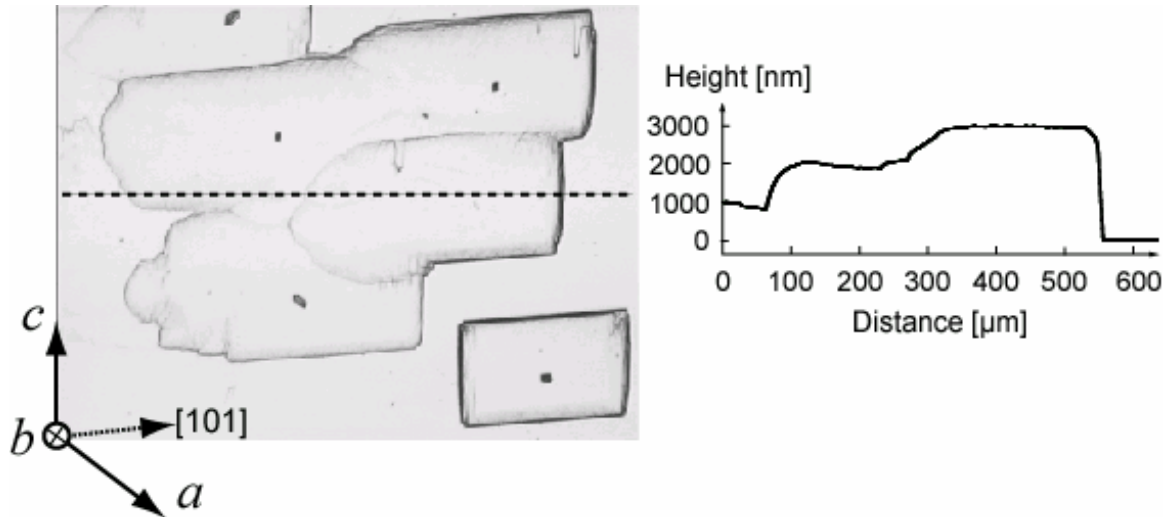


Fig. 4.15. Coalescence of the islands for 2 mol% Dy:KYW.

After island coalescence, the layer continues to grow with a tendency to facet formation, as can be recognized in Fig. 4.16. Well-developed pyramids alternate with macro-steps, which are distributed over the whole area of the layer as a consequence of the step-bunching process. The interstep terraces are inclined with respect to the substrate surface at the misorientation angle $\varphi = 0.18^\circ$, which corresponds to the precision of substrate orientation.

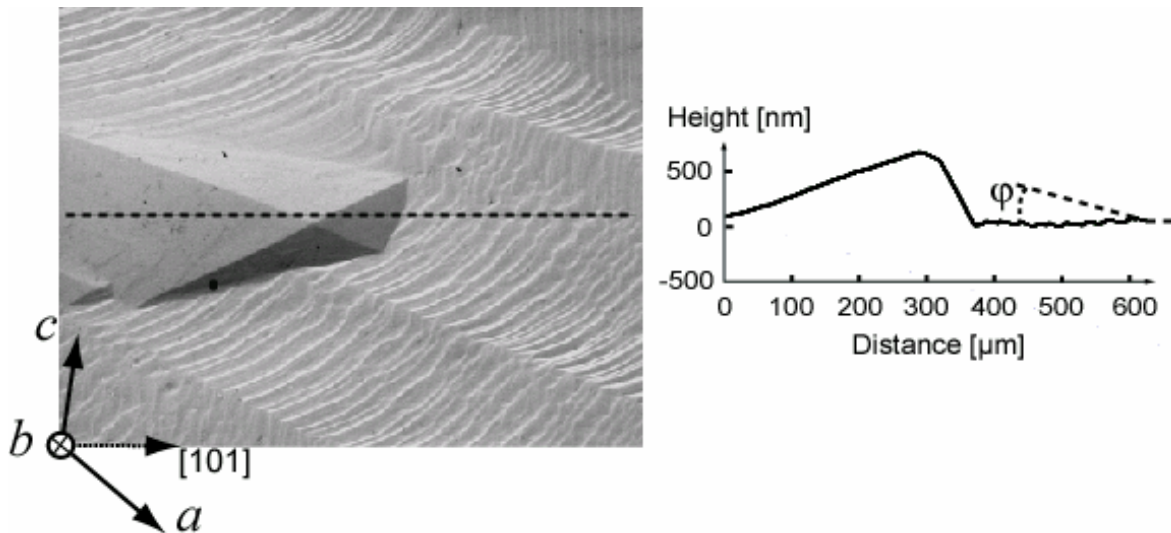


Fig. 4.16. A faceted pyramid coexists with macrosteps on the surface of a 15- μm thick KYW layer.

The observation of growth steps in the direction perpendicular to the maximum substrate misorientation provides an average step height $h = 30$ nm and an interstep distance $y_0 = 9$ μm . Using equation (3.7), the relative solution supersaturation $\sigma = 0.076$ at $T = 550^\circ\text{C}$. Here, the

heat of solution $L_{\text{sol}} = 48.3 \text{ kJ mol}^{-1}$ is assumed to be the same as for the solution of BaSO_4 in NaCl-KCl-CsCl [ehr03]. The calculated relative supersaturation $\sigma = 0.076$ for the chloride solvent is higher than $\sigma = 0.042$ for the tungstate solvent (Sect. 4.5.2). The higher supersaturation is needed to overcome the hindered nucleation and to prevent dissolution of the KYW:RE layer.

The layer thickness was typically 5-10 μm after 24 h of growth, which gives a mean linear growth rate of 0.2-0.4 $\mu\text{m h}^{-1}$, or approximately 4-8 unit cells min^{-1} . The observed low growth rates do not exceed the maximum stable growth rate of 1.3 $\mu\text{m h}^{-1}$ estimated in Sect. 3.5.

At dopant concentrations above 2 mol% of Yb or 5 mol% of Tb or Dy, the formation of a crack network was often observed, especially on the edges of the substrate. Since the lattice misfit between the low RE-doped layer and the substrate is far below the critical layer strain for crack formation (Sect. 3.3), we attribute the appearance of cracks to numerous insertion defects due to the specific 3D nucleation mechanism. These insertion defects result in the considerable layer strain ε_{def} persisting in the grown layer after cooling to room temperature. Consequently, the value of ε_{def} , which is difficult to calculate, cannot be neglected when inserting equation (3.17) into equation (3.20) and, therefore, the prediction of the critical thickness becomes problematic. Still, very thin layers (3-5 μm) were crack free even at RE concentration of 10 mol%.

Besides characteristic morphological features of the KYW:RE layers like growth steps and hillocks, tiny crystals of secondary phases $n\text{Y}_2\text{O}_3 \times m\text{WO}_3$ were also observed on the surface of almost all grown layers. Those parasitic phases, which were continuously formed in the chloride solution, precipitated both on the crucible walls and bottom, and, occasionally, on the KYW substrate. The parasitic crystals had an elongated prismatic or circular shape; sometimes they were arranged in bundles. Fig. 4.17 shows a parasitic whisker-like crystal found on the surface of a grown layer.

The quantitative energy-dispersive X-ray analysis (EDX) of the crystal gave an approximate composition of Y_2WO_6 , which is the same as the composition of parasitic phases found on the crucible bottom during the solubility investigation (Sect. 4.4.2). Fortunately, most of the parasitic crystals stayed on the layer surface, and could be easily removed after a few laps on the polishing tissue.

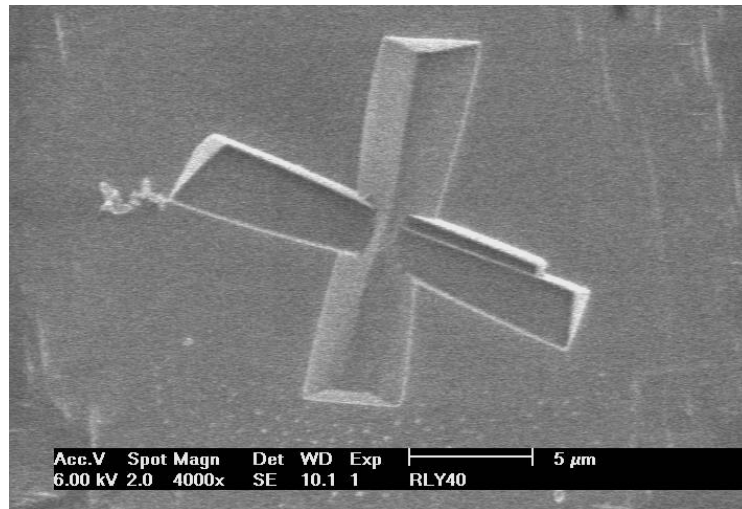


Fig. 4.17. SEM photograph of a parasitic Y_2WO_6 whisker crystal, formed on the surface of a 0.5 mol%Dy:KYW layer.

Because of an increasing interest in heavily Yb-doped KYW layers due to their possible application in the thin-disk laser concept [bru02], we attempted to grow a series of thin layers with 50 and 100 mol% of Yb. Regardless of the growth conditions, all layers exhibited a dense crack network except one 20- μ m thick KYbW layer, which was, surprisingly, almost crack-free [rom03]. However, when inspecting the layer-substrate interface with the ZYGO interferometer, we observed defects which looked like residual polishing scratches. Those defects gave rise to absorption losses of 3% in a single pass under perpendicular pumping and the layer was, therefore, not suitable for the laser experiments. Unfortunately, the growth of such a crack-free KYbW layer could not be repeated in any of the following experiments.

4.7 Microchannel epitaxy

Besides planar active layers which cover the whole substrate surface, channel active structures are highly desirable for applications in integrated optics. The channel structure allows the guided light to be confined in both the vertical and horizontal directions, which is especially important for the implementation of integrated waveguide lasers and amplifiers. Actual methods of channel fabrication imply either structuring of previously prepared planar active layers (wet and dry reactive ion etching, ion milling, light ion implantation, UV/femtosecond laser writing, etc.) or selective doping of the inert substrate with an active ion (ion diffusion and ion exchange).

The original method of microchannel epitaxy (MCE) has been employed in this thesis to produce ribs of KYW:RE directly during the LPE growth. The idea is to use an undoped KYW substrate with a patterned metal mask on the substrate surface. If such a treated substrate is immersed into the supersaturated solution, the KYW:RE layer will grow only on metal-free areas designed, e.g., in the form of long channels. To our knowledge, this is the first time that MCE is applied to grow an oxide material, and moreover, to produce optical waveguide channels.

The idea of MCE stems from the epitaxial lateral overgrowth (ELO) concept, which was introduced by Jastzebski *et al.* in 1983 for the fabrication of a semiconductor layer on an isolator structure [jas83]. Later, Ujiie and Nishinaga demonstrated that the dislocation density in the III-V semiconductor layer on different substrates could be significantly reduced when the layer is nucleated through narrow mask-free opening windows on the substrate surface [uji89]. Finally, the abbreviation of MCE was proposed by Nishinaga and Scheel [nish96] to denote any epitaxial process in which the substrate lattice information is transferred to the epitaxial layer through the narrow window (microchannel) of the substrate surface.

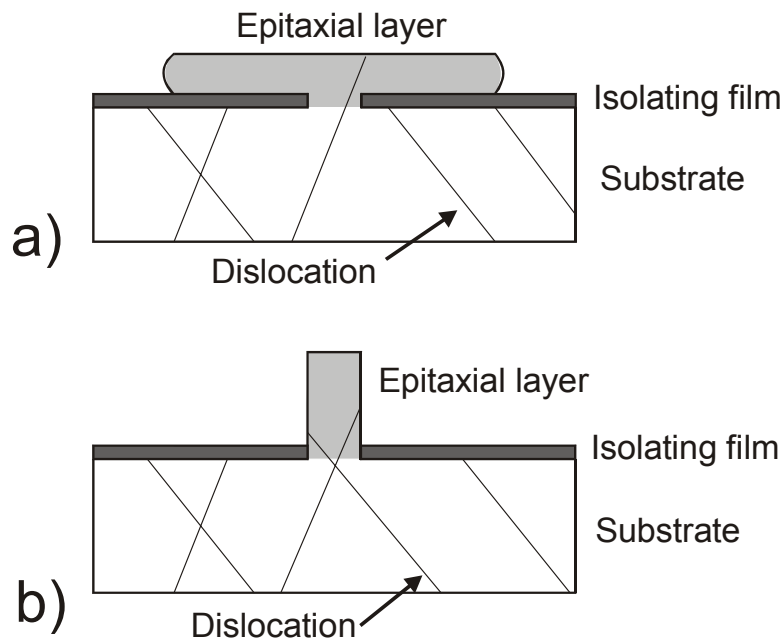


Fig. 4.18. Concept of microchannel epitaxy (MCE): horizontal (a) and vertical (b) MCE.

There are two possible versions of MCE, which are shown schematically in Fig. 4.18. In the horizontal MCE (Fig. 4.18a), the nucleation takes place through a microchannel and then the layer grows in lateral direction forming a planar layer. The reason of pronounced lateral overgrowth is a large anisotropy of growth rates. If the substrate surface coincides with a natural facet, the growth rate in vertical direction is normally much lower than that in lateral

direction (horizontal MCE). On the contrary, if the substrate is oriented perpendicular to a natural facet, the layer grows mainly in the vertical direction forming a shaped rib (vertical MCE). In both cases, most of the substrate defects, like dislocations, are stopped at the isolating layer.

4.7.1 Mask fabrication

The isolating mask should be resistant against chemical and physical corrosion in the high-temperature solution. In this sense, inert precious metals, like Pt or Au, appear to be the optimum material for the insulating mask. We tested two different approaches to prepare a patterned metal mask for the undoped KYW substrate.

A. Platinum foil mechanically fixed on the substrate surface. The mask was cut from a thin 25 μm -thick Pt foil using the laser cutting setup installed at the Institute of Imaging and Applied Optics (EPF Lausanne). A pulsed Nd:YAG slab laser in the fundamental mode ($M^2 < 1.3$) with pulse length 1 ms, repetition rate 300 Hz, and a peak pulse power up to 2 kW at 1064 nm was used. The minimum beam diameter at the focus was about 20 μm and the cutting speed was 1.6 mm/s.

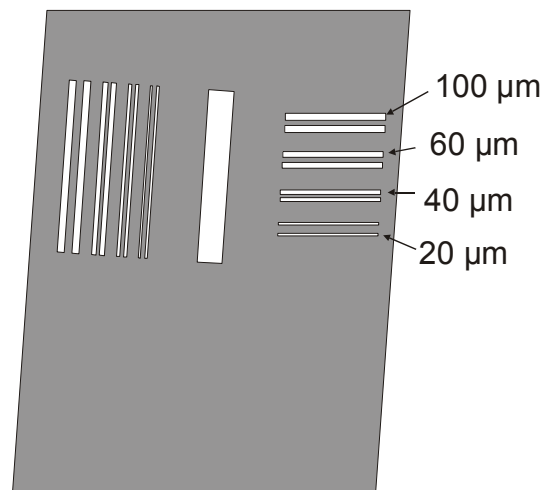


Fig. 4.19. Design of the isolating mask made from a 25- μm thick Pt foil.

The test mask was designed to cover the whole substrate face as shown in Fig. 4.19. Several parallel slits 20-100 μm in width were cut in the Pt foil. The minimum slit width of 20 μm was limited by the minimum focus diameter of the laser beam. The mask was fixed directly

on the substrate with a Pt clamp (not shown in Fig. 4.19), so that the slits were parallel to the crystallographic directions of the KYW substrate. Thus, the ribs' facets were expected to be straight and flat because they coincided with the $\{\bar{1}11\}$ or $\{310\}$ crystal faces.

B. Platinum or Gold mask deposited onto the substrate surface. The deposition of a metal mask onto the substrate surface includes two basic steps: 1) fabrication of a shielding mask and 2) deposition of a Pt or Au isolating layer through the shielding mask using plasma vapor deposition (PVD).

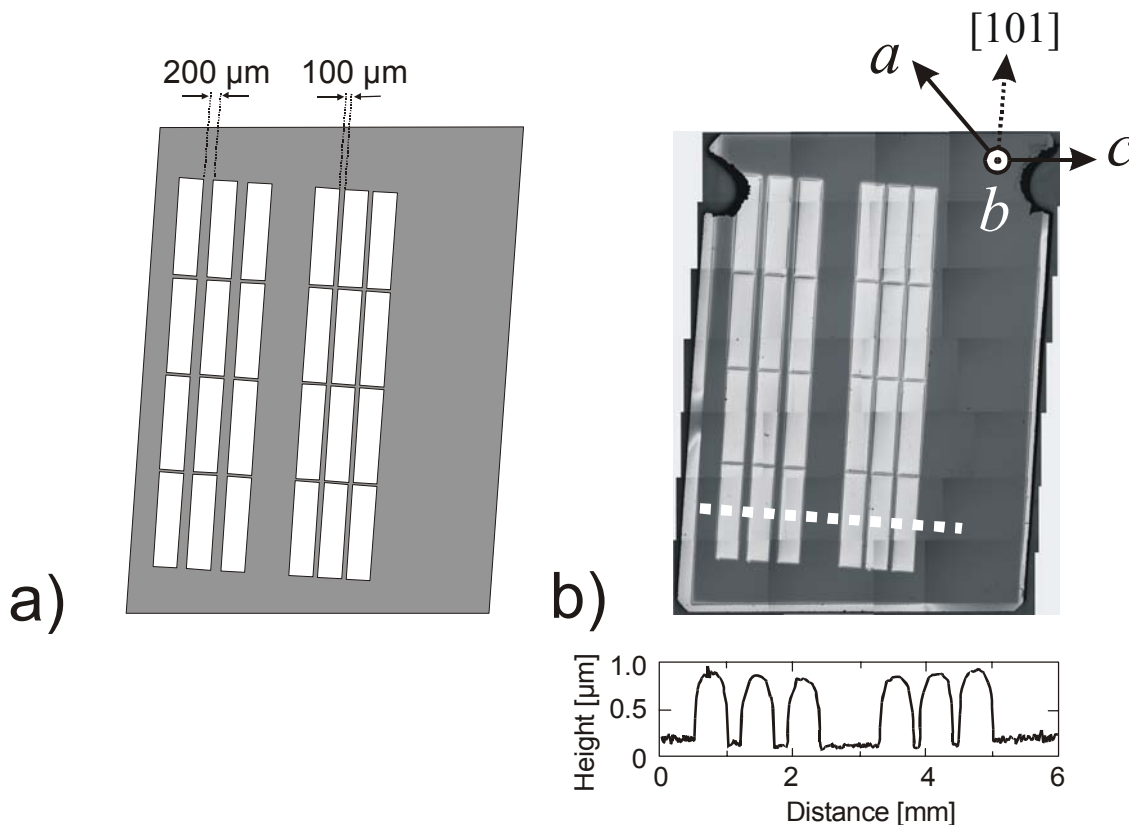


Fig. 4.20. (a) Design of the 200- μm thick steel shielding mask used for PVD. (b) Gold isolating layer (light areas) deposited on the KYW substrate together with the respective height profile of the deposit.

The shielding mask was produced by cutting a 200- μm steel foil with the Nd:YAG pulsed laser. The mask design is shown in Fig. 4.20a. There are two pairs of vertical strips having the width of 100 or 200 μm each. The minimum strip width was limited to 100 μm because narrower strips could be easily bent or broken during the fabrication. Moreover, 3 sets of additional crossbars, each 50 μm wide, were used to support the freestanding vertical strips.

The shielding mask was oriented on the substrate surface in such a way that the vertical strips were parallel to the $[101]$ crystallographic direction. The substrate covered with

the shielding mask was placed in a deposition chamber. The PVD deposition was performed by Dr. Ivo Utke at EMPA (Thun, Switzerland) using Ar as a transport gas. Two metals, Pt and Au, have been tested as isolating films.

The thickness of the obtained metal deposits was 0.8-1.5 μm , which could be easily controlled by varying the processing time. The height of the deposited strips was quite uniform over the whole substrate surface (Fig. 4.20b). However, we observed some metal deposition even on areas covered by the shielding steel mask. This “shadow effect” was due to a small air gap between the shielding mask and the substrate.

4.7.2 Microchannel epitaxy of $KY(WO_4)_2:Yb$ ribs

We employed the $K_2W_2O_7$ solvent to grow the KYW:Yb ribs because the tungstate solvent apparently offers better layer quality and better growth control than the chloride one. Moreover, the NaCl–KCl–CsCl solvent is quite corrosive for the used metal masks. The experimental procedure was the same as for the growth of planar KYW:RE layers (Sect. 4.5.1). The (010) $KY(WO_4)_2$ substrate with the patterned mask on the direct face was immersed in the saturated solution at a temperature of 898°C. The growth lasted for 15-60 min at a cooling rate of 0.6 K h⁻¹. The KYW:Yb ribs, which were grown on metal-free areas of the substrate, had a typical height of 3-15 μm . The quality and shape of the ribs strongly depended on the type of applied mask, as detailed below.

A. MCE with Pt foil mechanically fixed on the substrate surface. After the growth, the Pt shielding foil was carefully removed from the substrate and the grown rib structures were examined by microscopy and profilometry. Three pairs of grown ribs from the upper right part of the substrate surface are shown in Fig. 4.21.

The shape of the grown ribs corresponds well with the slit contours in the shielding mask. The top of the ribs is flat because it coincides with the natural (010) face. However, the sidewalls of the ribs are not as uniform and they contain many side outgrowths. These outgrowths appeared because it was impossible to avoid a gap between the substrate surface and the mask plane fixed with the simple Pt clamp. Thus, the liquid solution penetrated underneath the shielding mask, and the growth took place even outside the slit areas.

A more severe problem occurring during the MCE with the direct Pt foil is cracking of the substrate and grown ribs. As was described in Sect. 4.5.1, a contact of bulk Pt pieces with the KYW substrate in the liquid solution always leads to cracking of the substrate,

presumably because of induced thermal shocks. As a result, the maximum length of crack-free ribs was limited to about 1 mm, which was not sufficient for optical investigations.

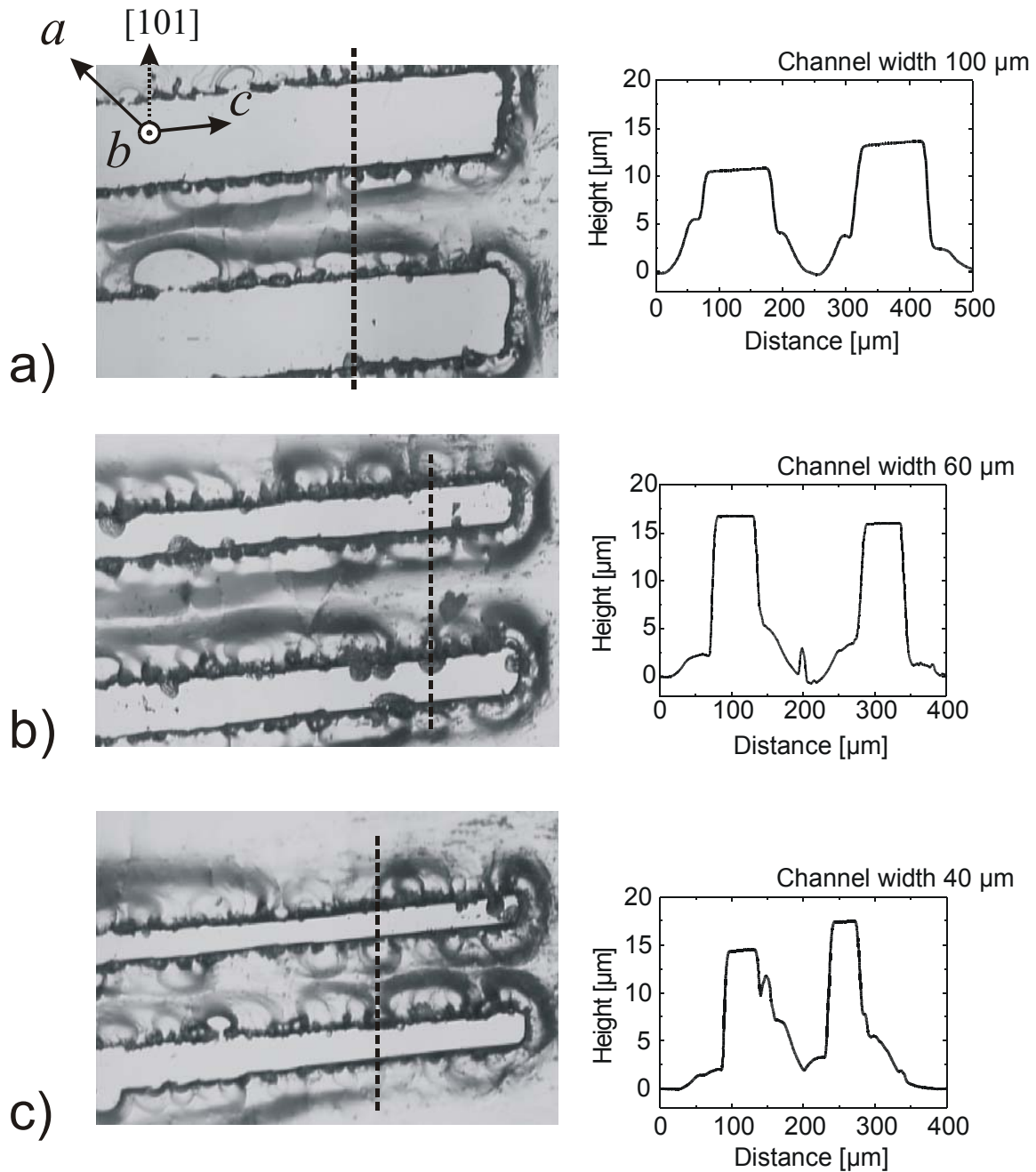


Fig. 4.21. Ribs of 1.7 mol% Yb:KYW grown through a Pt foil mask mechanically fixed to a KYW substrate.

B. MCE with Pt/Au mask deposited onto the substrate surface. Since the thickness of the Pt/Au deposits was only 0.8-1.4 μm, they could not induce cracking of the substrate. Therefore, the grown KYW:Yb ribs were crack-free over the whole length. Fig. 4.22a shows a pair of KYW:Yb ribs, which have been grown along the [101] crystallographic direction. A few growth steps are visible on the ribs' top, otherwise the ribs' surfaces are flat and parallel

to the natural (010) face. A small inclination of the ribs' top with respect to the initial surface is due to the substrate misorientation, which is about 0.3° .

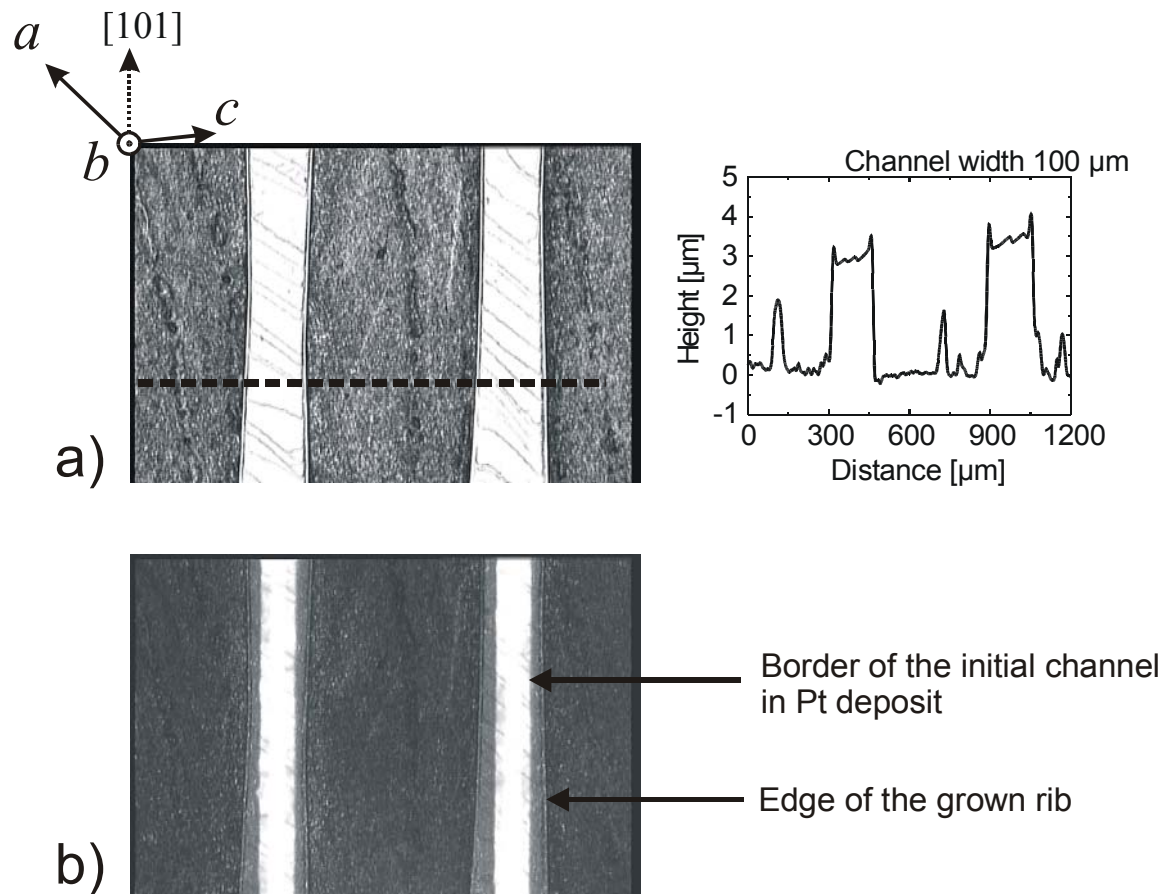


Fig. 4.22. (a) Ribs of 1.7 mol% Yb:KYW (light areas) grown through channels in the Pt isolating deposit (dark areas). (b) Transmission microphotograph showing borders of the channels in the Pt deposit. Photos (a) and (b) are taken in the same place.

While the width of the metal-free channels in the Pt deposit is $100\ \mu\text{m}$, the width of the grown ribs reaches $200\ \mu\text{m}$. The transmission microphotograph in Fig. 4.22b clearly shows that the borders of the grown ribs exceed the limits of the initial metal-free channels. This is caused by the pronounced lateral growth of the layer over the metal deposit.

The polished end-face of one as-grown rib is presented in Fig. 4.23. The KYW:Yb layer is nucleated on the metal-free area and, at the beginning, grows in the vertical $[010]$ direction. Once the layer thickness exceeds the height of the metal deposit, the layer grows more rapidly along the lateral $[001]$ direction, forming a rib with an aspect ratio of width/height ≈ 15 . This is a clear example of the horizontal MCE depicted in Fig. 4.18a. The growth rate of the layer along the lateral $[001]$ direction is much faster than that in the vertical $[010]$ direction because the substrate surface coincides with the (010) face. It is worth noting

that the side walls of the rib are also bounded with two sharp planes. They correspond to the $\{\bar{1}11\}$ faces.

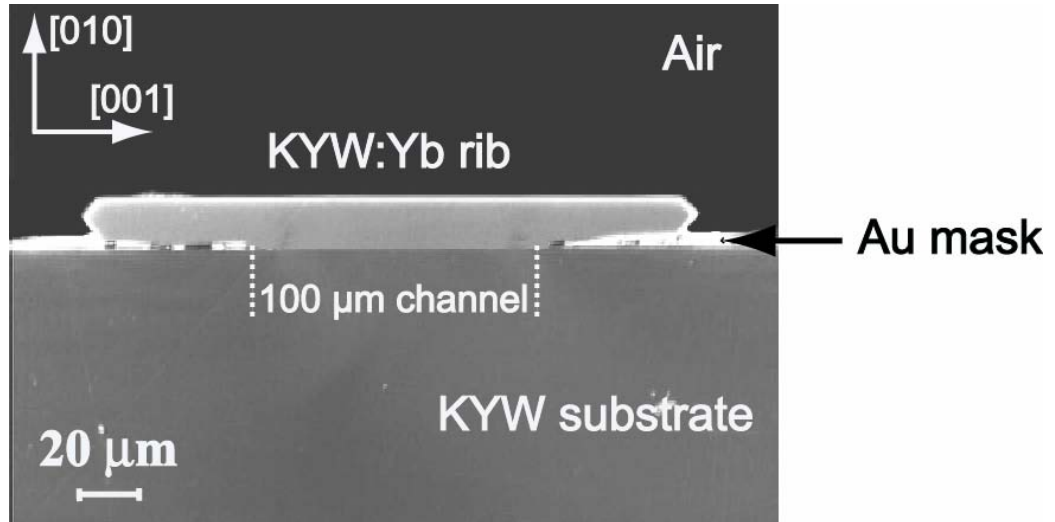


Fig. 4.23. Cross-section of a 1.7 mol% Yb:KYW rib grown on a KYW substrate with the Au isolating mask.

To obtain ribs with aspect ratios close to unity, the excessive lateral overgrowth should be blocked either by changing the substrate orientation or by increasing the thickness of the metal deposit. We have tested both possibilities. First, we tested (101)-oriented KYW substrates. However, this approach did not provide any significant improvement because the growth rate in the vertical [101] direction is high and not stable, leading to large variations in rib thickness over its length. Second, we increased the metal deposit thickness to 4-5 μm on the (010) substrate. The lateral overgrowth could be blocked if the rib thickness was below 5 μm. However, the quality of the metal pattern should be improved, and a strong “shadow effect” must be avoided when producing thick metal deposits.

Nevertheless, after removal of the metal mask, such as-grown ribs of KYW:Yb having aspect ratios of about 15 and lengths of up to 6 mm can be used for waveguide investigations.

5. Characterization of the grown layers

5.1 Orientation and crystallinity

The orientation and crystalline quality of the grown layers were evaluated by means of X-ray diffraction (XRD). The XRD measurements were performed on an X'Pert Philips diffractometer in Bragg-Brentano geometry with $\text{CuK}_{\alpha 1}$ radiation. For KYW:RE layers, the penetration depth ($1/e$ absorption) of the $\text{CuK}_{\alpha 1}$ radiation with the wavelength $\lambda = 0.154060$ nm is $12 \mu\text{m}$ at the normal incidence (the Bragg angle $\theta = 180^\circ$) and about $2 \mu\text{m}$ at the Bragg angle $\theta = 10^\circ$ (calculated using the X-ray attenuation length simulator at [cxro05]).

Layers grown from the $\text{K}_2\text{W}_2\text{O}_7$ solvent. Only $(0\ 2n\ 0)$ reflections of the α -KYW phase could be observed on all diffraction patterns of the layers grown on b -oriented KYW substrates (Fig. 5.1). Together with microscopic observations, it shows that the layers were strictly oriented in the $[010]$ direction and no other grain orientations were found.

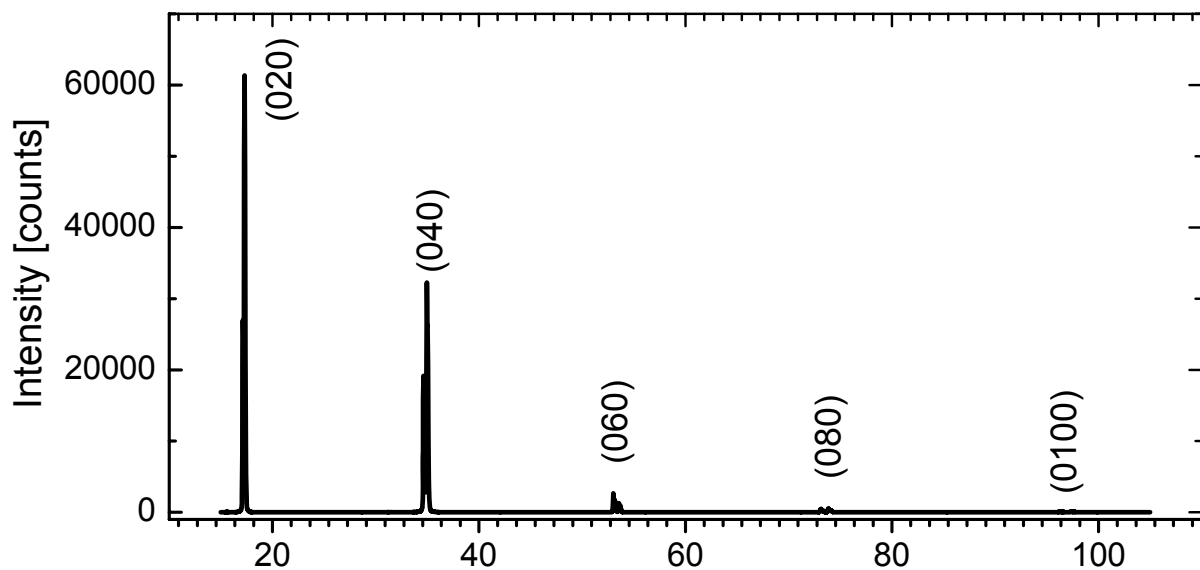


Fig. 5.1. 2θ -scan of a 30- μm thick undoped KYW layer grown on a (010) KYW substrate

The b -lattice constant was precisely calculated from the Bragg equation

$$n\lambda = 2d \sin \theta. \quad (5.1)$$

Here n is the reflection order, λ is the wavelength of $\text{CuK}_{\alpha 1}$ radiation ($\lambda = 0.154060$ nm), d is the interplane distance (in our case $d = b$), and θ is the Bragg angle. The calculated value $b =$

1.0343(2) nm is in good agreement with the reported $b = 1.035$ [kle68] and $b = 1.03452(6)$ [puj96].

A rocking curve measurement was performed for the (0 2 0) reflection of an undoped KYW layer on a KYW substrate. The layer thickness was 30 μm and we neglected the contribution of the substrate reflection. The calculated full-width-at-half-maximum (FWHM) for the layer was 0.083° . This value was very close to the $\text{FWHM} = 0.081^\circ$ measured for a high-quality undoped KYW crystal grown by TSSG, which confirms the high structural perfection of the layer.

Layers grown from the NaCl–KCl–CsCl solvent. The diffraction patterns were identical to those for the layers grown from the $\text{K}_2\text{W}_2\text{O}_7$ solvent. Only (0 $2n$ 0) reflections of the α -KYW modification were observed. No diffraction reflections of the secondary $n\text{Y}_2\text{O}_3 \times m\text{WO}_3$ phases could be found. A few tiny parasitic crystals present on the layer surface did not give sufficient reflection intensity to be detected with the XRD method.

Since the layers grown from the chloride solvent had a maximum thickness of 10 μm , the diffraction patterns also contained intensive peaks arising from the KYW substrate. Moreover, the substrate peaks shielded the layer peaks because the lattice mismatch between KYW:RE and KYW is rather low even for 100% doping (Table 3.1). Only at elevated dopant concentrations or high 2θ angles the layer peak could be discriminated.

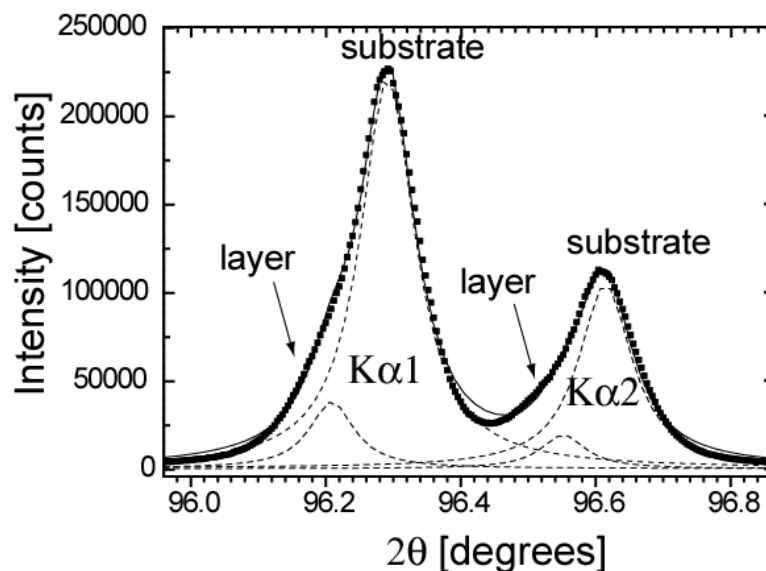


Fig. 5.2. Detail of the (0 10 0) Bragg reflection of a 10 mol% Tb-doped KYW layer on a KYW substrate. Superposed reflections of the $\text{CuK}_{\alpha 1}$ and $\text{CuK}_{\alpha 2}$ radiation for layer and substrate were fitted with four Lorentzian functions.

Figure 5.2 represents the (0 10 0) Bragg reflection of a 5- μm thick Tb-doped KYW layer on a *b*-oriented KYW substrate. Reflections of the $\text{CuK}_{\alpha 1}$ and $\text{CuK}_{\alpha 2}$ wavelengths from the (0 10 0) plane of layer and substrate gave rise to four peaks, which were fitted with four Lorentzian functions. From the difference in positions of the layer and substrate peaks we could estimate the content of Tb in the layer to be approximately 13 mol% with respect to Y, whereas the initial Tb concentration in the solution was 10 mol%. The slightly higher concentration of Tb in the KYW:Tb layer than in the initial solution is in agreement with the distribution coefficient of Tb^{3+} , $K_{\text{Tb}^{3+}} \approx 1.04$, found by electron probe microanalysis (Sect.5.2.2).

A rocking curve measurement was performed for the (0 2 0) reflection of a 14- μm thick undoped KYW layer on a KYW substrate. We assumed that the contribution of the substrate peak was negligible. The derived FWHM was 0.098° . This value is larger than FWHM of 0.083° for a layer grown from the $\text{K}_2\text{W}_2\text{O}_7$ solvent, indicating the lower crystalline quality of the layer grown from the chloride solvent.

5.2 Composition

5.2.1 Stoichiometry of the KYW matrix

Since previous works reported on possible off-stoichiometric values of KYW (Sect. 2.1.2), the composition of the grown layers was investigated by elemental X-ray fluorescence spectrometry (XRF) and energy-dispersive X-ray analysis (EDX). The XRF measurements were performed on a Kevex–Omicron system. An excitation energy of 40 keV allowed simultaneous quantitative determination of all cations (K and Y on K-lines, W on L-lines). The EDX measurements were performed with a Philips XL 30 SFEG scanning electron microscope. The excitation energy was chosen to be 5 keV in order to avoid pronounced charging effects on the non-conductive KYW:RE layers. The quantification was done with the Oxford Instruments INCA 4.04 package. The K content was determined on K-lines, Y on L-lines, and W on M lines. Taking into account that L-lines of Y partially overlap with M-lines of W, the quantification strongly depended on the peak fitting procedure.

Layers grown from the $\text{K}_2\text{W}_2\text{O}_7$ solvent. The atomic concentrations of the cations in four different KYW layers, measured against their KYW single-crystal substrates, are given in Table 5.1. We assume that the KYW substrates grown by the TSSG method have the theoretical stoichiometry of 25 at% K, 25 at% Y, and 50 at% W. The detected cation

concentrations are different for four investigated layer-substrate pairs. However, this discrepancy may not be attributed to the different layer concentrations but may arise from the difference in surface roughness between the investigated layers, i.e. from a systematic error of the XRF method. Within the standard deviation, the calculated average concentrations correspond to the substrate composition. This is expected from the fact that the layers and substrates were grown from the same tungstate solvent at similar growth temperatures.

Table. 5.1. Stoichiometric and experimental cation composition of undoped KYW layers measured by XRF. The indicated errors for individual layers are statistical errors. The indicated errors for average values are standard deviations. All layers were grown from the $K_2W_2O_7$ solvent.

Compound	Standard	K (at%)	Y (at%)	W (at%)
KYW substrate		25.0	25.0	50.0
KYW layer A	KYW substrate	24.94±0.3	24.52±0.3	50.54±0.5
KYW layer B	KYW substrate	21.22±0.3	25.69±0.3	53.09±0.5
KYW layer C	KYW substrate	25.73±0.3	23.93±0.3	50.34±0.5
KYW layer D	KYW substrate	24.42±0.3	24.79±0.3	50.79±0.5
Average A, B, C, D		24.08±1.98	24.73±0.73	51.19±1.28

In order to estimate the absolute concentration of the cations, both the layer and substrate composition was measured by EDX against internal elemental standards of the INCA 4.04 package (Table 5.2).

Table. 5.2. Stoichiometric and experimental cation composition of an undoped KYW layer and its substrate measured by EDX. The indicated errors are statistical experimental errors. The layer and the substrate were grown from the $K_2W_2O_7$ solvent.

Compound	Standard	K (at%)	Y (at%)	W (at%)
KYW	Stoichiometric formula	25.0	25.0	50.0
KYW substrate	Internal EDX standards	25.90±2.47	21.58±1.99	52.52±0.75
KYW layer	Internal EDX standards	27.01±2.59	18.99±2.05	54.00±0.77

The observed yttrium content in the KYW substrate, as well as in the KYW layer, is lower than the expected stoichiometric value of 25 at%. This is in contradiction with the previous

report on the excessive yttrium content in KYW single crystals measured by inductively coupled plasma (ICP) emission spectrometry [gal00]. We attribute this discrepancy to systematic errors of the two methods employed. In order to determine the exact composition of KYW, an independent cross-check analysis with reliable standards would be necessary. It follows from Table 5.2, that the compositions of the layer and its substrate are rather close.

Layers grown from the NaCl–KCl–CsCl solvent. The atomic concentrations of the cations in a 14- μm thick KYW layer, measured against a KYW single-crystal standard grown by the TSSG method, are given in Table 5.3 together with the theoretical cation concentrations of the stoichiometric KYW compound. Within the experimental statistical error, the compositions of layer and single crystal are the same. However, when measuring the layer against a standard of pressed powders of K_2WO_4 and Y_2O_3 , we observed a slight deviation from this standard. This deviation may not be attributed to a non-stoichiometry of layer and single crystal but may arise from the difference in structure and aggregation state between the powder standard and the investigated samples, i.e., from a systematic error of XRF.

Table. 5.3. Stoichiometric and experimental cation composition of a 14- μm thick undoped KYW layer measured by XRF. The indicated errors are statistical experimental errors. The layer was grown from the NaCl–KCl–CsCl solvent.

Compound	Standard	K (at%)	Y (at%)	W (at%)
KYW	Stoichiometric formula	25.0	25.0	50.0
KYW layer	KYW single crystal	24.8 \pm 0.3	25.0 \pm 0.3	50.2 \pm 0.5
KYW layer	K_2WO_4 and Y_2O_3 powders	23.1 \pm 0.3	25.0 \pm 0.3	51.9 \pm 0.5

5.2.2 Incorporation of RE^{3+} ions

The incorporation rate of different RE^{3+} ions from the molten solution into the KYW layer can be expressed for each RE^{3+} ion via the distribution coefficient K :

$$K_{\text{RE}^{3+}} = \left[C_{\text{RE}^{3+}} \right]_{\text{layer}} / \left[C_{\text{RE}^{3+}} \right]_{\text{solution}}. \quad (5.2)$$

Here as well as in the previous chapters, the molar concentration $C_{\text{RE}^{3+}}$ is considered with respect to the Y^{3+} content:

$$C_{\text{RE}^{3+}} = \text{moles RE}^{3+} / (\text{moles RE}^{3+} + \text{moles Y}^{3+}). \quad (5.3)$$

Layers grown from the $K_2W_2O_7$ solvent. The distribution coefficients of different RE ions have already been investigated in the network of the FP6 European Project [dte04]. By analyzing the composition of KYW:RE crystals grown by TSSG from $K_2W_2O_7$, the following distribution coefficients, $K_{RE^{3+}}$, were found: 1.00 for Pr^{3+} , 1.02 for Nd^{3+} , 1.00 for Dy^{3+} , 0.96 for Er^{3+} , 1.04 for Tm^{3+} , and 0.99 for Yb^{3+} . All distribution coefficients are very close to unity, which should lead to an equal incorporation probability of both the Y^{3+} and RE^{3+} ions during the KYW:RE crystal growth. Obviously, the same distribution coefficients should be expected for KYW:RE layers grown from this tungstate solvent. Therefore, we did not repeat the investigation of distribution coefficients for the $K_2W_2O_7$ solvent but concentrated on the investigation of $K_{RE^{3+}}$ for the NaCl–KCl–CsCl solvent.

Layers grown from the NaCl–KCl–CsCl solvent. The doping levels of RE ions in the grown layers, $[C_{RE^{3+}}]_{layer}$, were investigated by electron probe microanalysis (EPMA) using the Cameca SX50 model with an acceleration voltage of 20 kV. The RE concentration in solution during the layer growth, $[C_{RE^{3+}}]_{solution}$, is assumed to be constant and equal to the initial RE concentration. Table 5.4 represents the detected ion concentrations in the layer together with the distribution coefficients calculated from equation (5.2).

Table 5.4. Incorporation of RE ions into KYW thin layers measured by EPMA. *K*-errors are standard deviations.

RE ion	$C_{RE^{3+}}$ in solution (mol%)	$C_{RE^{3+}}$ in layer (mol%)	Distribution coefficient, $K_{RE^{3+}}$	Ionic radius (Å) [sha76]
Tb^{3+}	0.50	0.51	1.04±0.03	1.040
	2.00	2.12		
Dy^{3+}	2.00	2.18	1.00±0.16	1.027
	5.00	4.08		
	10.00	11.05		
Y^{3+}				1.019
Yb^{3+}	1.00	1.07	0.82±0.27	0.985
	5.00	2.67		
	10.00	8.43		

The estimated distribution coefficient for Tb^{3+} and Dy^{3+} ions is close to unity, whereas the incorporation of Yb^{3+} appears to be lower due to the highest negative misfit of its ionic radius with that of the substituted Y^{3+} ion (Table 3.1). Ions with an ionic radius slightly larger than that of the substituted ion may incorporate better into oxide crystals than those with smaller ionic radius [nas71]. Although the standard deviations of our few measurements are too large

to confirm unambiguously this tendency, the RE-ion incorporation for the chloride solvent appear to decrease in the series $Tb^{3+} > Dy^{3+} > Yb^{3+}$.

The distribution coefficients of RE^{3+} ions measured in [dte04] for the layer growth from the $K_2W_2O_7$ solvent do not support this tendency. A possible reason could be the large difference in growth rate between the tungstate and chloride solutions. In particular, the typical linear growth rate from the chloride solution is $0.3 \mu m h^{-1}$, which is about 60 times lower than for the tungstate solution (Sect. 4.6.2). The low growth rate assumes more selective incorporation of the solute and dopant species and the effect of the ionic radius misfit becomes significant.

Other impurity ions could not be detected in the grown KYW:RE layers by EPMA or XRF.

5.3 Comparison of layers grown from the $K_2W_2O_7$ and NaCl–KCl–CsCl solvents

The main characteristics of the KYW:RE layers grown from the $K_2W_2O_7$ (type A) and NaCl–KCl–CsCl (type B) solvents are compared in Table 5.5.

Table 5.5. Investigated properties of KYW:RE layers grown on (010) KYW substrates from the $K_2W_2O_7$ and NaCl–KCl–CsCl solvents.

Property	(A) $K_2W_2O_7$ solvent	(B) NaCl–KCl–CsCl solvent
Accessible layer thickness	1–100 μm	1–10 μm
Orientation	(010)	(010)
Crystallinity	single crystalline	coalesced single crystalline grains
FWHM of (020) reflex	0.083°	0.098°
Parasitic phases	None	$nY_2O_3 \times mWO_3$
Composition	same as KYW substrate	same as KYW substrate
Distribution coefficient $K_{RE^{3+}}$	≈ 1.0 for Dy^{3+} , Er^{3+} , Tm^{3+} , Yb^{3+}	≈ 1.0 for Tb^{3+} and Dy^{3+} ≈ 0.8 for Yb^{3+}

For layers (A), a wide range of layer thicknesses is accessible, whereas for layers (B) the maximum layer thickness is limited to about 10 μm after 24 hours of growth. Both layers (A)

and (B) exhibit the same (010) orientation when grown on (010) KYW substrates. Layers (A) are entirely single crystalline. Layers (B) can be considered only as aggregates of coalesced single crystalline grains which developed because of the pronounced 3D nucleation mechanism. The FWHM of (020) diffraction reflex is smaller for type (A), which confirms their higher structural perfection. Moreover, the growth of layers (B) is complicated by the formation of the secondary phases $n\text{Y}_2\text{O}_3 \times m\text{WO}_3$.

The compositions of layers (A) and (B) are similar and they are very close to the composition of KYW substrates. The distribution coefficient, $K_{\text{RE}^{3+}}$, is close to unity for many RE^{3+} ions in layers (A). For layers (B), the distribution coefficient of Tb^{3+} and Dy^{3+} is close to unity, whereas $K_{\text{Yb}^{3+}} \approx 0.8$ due to the highest misfit of ionic radii between Yb^{3+} and Y^{3+} . Probably, the effect of the ionic radius misfit is more pronounced for layers (B) because of the extremely low layer growth rate in the chloride solvent.

The maximum RE^{3+} concentration incorporated into crack-free layers (A) was 5 mol% (e.g. 2.5 mol% Er^{3+} and 2.5 mol% Yb^{3+} in co-doped layers). The maximum tested RE^{3+} for crack-free layers (B) was 10 mol% Tb^{3+} or Dy^{3+} , and even 100 mol% Yb^{3+} (not reproducible). However, the possibility to incorporate high doping concentrations in layers (B) at low growth temperatures is degraded by limitations in accessible layer thickness and insertion defects due to the 3D nucleation mechanism.

As a conclusion, layers (A) grown from the $\text{K}_2\text{W}_2\text{O}_7$ solvent were suitable for the spectroscopic investigation of energy-transfer processes as well as all waveguide and laser experiments. Layers (B) grown from the NaCl-KCl-CsCl solvent were used only for the spectroscopic investigation of energy-transfer processes and tested as optical waveguides.

6. KY(WO₄)₂:RE optical waveguides

6.1 Theory of optical waveguides and waveguide lasers

Dielectric planar waveguides

Optical waveguides, also known as “dielectric” waveguides, are structures used to confine and guide light in a dielectric material surrounded by media of lower refractive indices [sal91]. The simplest waveguide is a planar slab illustrated in Fig. 6.1, where a planar film of thickness d and refractive index n_f is sandwiched between a substrate and a cover with lower refractive indices n_s and n_c ($n_f > n_s > n_c$). Often, the cover is air ($n_c = 1$), and the respective structure is called *surface* waveguide. If the cover is not air but a dense material, often the same as the substrate, the structure is called *buried* waveguide. The higher refractive index in the waveguiding film can be achieved either by using a different material than the substrate, or by changing the properties of the substrate only in specific regions where the light should be guided (doping with ions that increase the refractive index, implantation of high-energy light ions, laser irradiation, etc.).

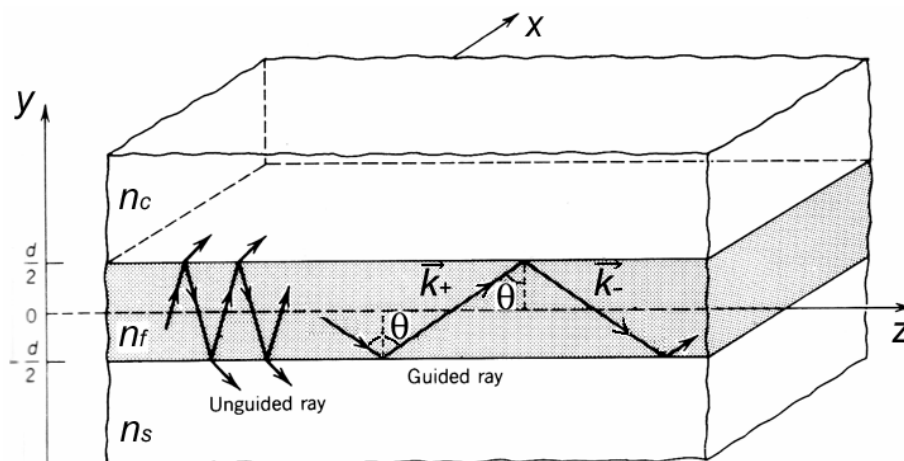


Fig. 6.1. Planar dielectric waveguide.

The light is guided inside the film along the z axis by total internal reflection. This phenomenon takes place when the angle θ between an incident beam and a normal to the z propagation axis is greater than a certain critical angle θ_{crit} . The critical angle can be calculated from Snell's law

$$\theta_{\text{crit}} = \arcsin \frac{n_2}{n_1}, \quad (6.1)$$

where n_1 is the refractive index of the film and n_2 is the refractive index of the substrate or cover, so that $n_1 > n_2$. If $\theta < \theta_{\text{crit}}$, there occurs only partial reflection and the ray is not guided. As soon as the critical angle is exceeded, $\theta > \theta_{\text{crit}}$, total reflection occurs and the ray is guided between interfaces.

The light propagates in the zig-zag manner through the film. More precisely, the propagating light can be described as two superimposed uniform plane waves [kog75]. These waves are monochromatic and coherent with angular frequency ω , wavelength λ , and wave vectors \vec{k}_+ and \vec{k}_- . The absolute value of \vec{k} is

$$|\vec{k}_+| = |\vec{k}_-| = kn_f = \frac{2\pi}{\lambda} n_f = \frac{\omega}{c} n_f, \quad (6.2)$$

where c is the velocity of light in vacuum. The z -component of the wave vector \vec{k} can be written as a *propagation constant* β

$$\beta = kn_f \sin \theta, \quad (6.3)$$

which is the z -component of the wave vector \vec{k} . However, not all angles θ are allowed; only a discrete set of angles lead to a self-consistent wave propagation, which corresponds to the existence of *guided modes*. For self-consistency, the sum of all the phase shifts of propagating waves after two reflections must be a multiple of 2π , i.e., as a waveguided wave reflects twice it duplicates itself (Fig. 6.2).

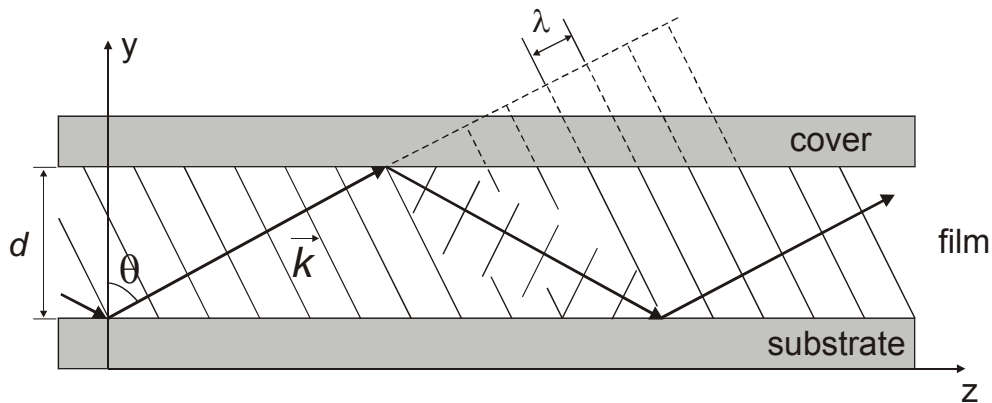


Fig. 6.2. Condition of self-consistency: as a guided wave reflects twice it duplicates itself.

For a film of thickness d we have a phase shift of $kn_f d \cos \theta$ for the first transverse course through the film, a phase shift of $-2\phi_c$ on total reflection from the film-cover interface,

another $kn_f d \cos \theta$ on the transverse course down, and, finally, a phase shift of $-2\phi_s$ on the total reflection from the film-substrate interface. Thus, the self-consistency condition known as the *transverse resonance condition* is

$$2kn_f d \cos \theta - 2\phi_c - 2\phi_s = \pm m2\pi \quad (m = 0, 1, 2, \dots). \quad (6.4)$$

Here, m is called the mode number, and the phase shift, ϕ_c or ϕ_s at a given interface, is defined by Fresnel formula

$$\tan \phi = \frac{\sqrt{n_1^2 \sin^2 \theta - n_2^2}}{n_1 \cos \theta}. \quad (6.5)$$

where $n_1 \equiv n_f$ and $n_2 \equiv n_s, n_c$. This formula holds true for the TE polarization of the guided light, and, naturally, it can be modified for the TM polarization.

To analyze possible TE modes that are supported by a waveguide, some normalized parameters are usually introduced. First, a frequency parameter, V , normalized to the film thickness is defined as

$$V = kd \sqrt{n_f^2 - n_s^2}. \quad (6.6)$$

Then, a normalized guide index b is defined as

$$b = (N_{\text{eff}}^2 - n_s^2) / (n_f^2 - n_s^2), \quad (6.7)$$

where N_{eff} is the effective refractive index of the film so that $n_s < N_{\text{eff}} < n_f$:

$$N_{\text{eff}} = \beta / k = n_f \sin \theta. \quad (6.8)$$

The guide index b is zero at cut-off of the mode and approaches unity far away from it. Finally, a measure for the asymmetry of the waveguide structure is defined as

$$a = (n_s^2 - n_c^2) / (n_f^2 - n_s^2). \quad (6.9)$$

This measure applies to the TE modes and ranges in value from zero for perfect symmetry (buried waveguide with $n_s = n_c$) to infinity for strong asymmetry (surface waveguide with $n_s \neq n_c$ and $n_s \approx n_f$). Using equations (6.6)–(6.9), one can rewrite the transverse resonance condition (6.4) in the form:

$$V \sqrt{1-b} = m\pi + \arctan \sqrt{b/(1-b)} + \arctan \sqrt{(b+a)/(1-b)}. \quad (6.10)$$

Setting $b = 0$ in equation (6.10), we can determine the cut-off frequency V_m of the m -th order TE mode and the minimum thickness of a given waveguide, which can support the propagation of the m -th order mode:

$$V_m = m\pi + \arctan \sqrt{a}; \quad (6.11)$$

$$d = (\lambda / 2\pi)(m\pi + \arctan \sqrt{a})(n_f^2 - n_s^2)^{-1/2}. \quad (6.12)$$

A numerical simulation of the last equation (6.12) yields the cut-off for different order TE modes as a function of the film thickness d and refractive index change $\Delta n = n_f - n_s$.

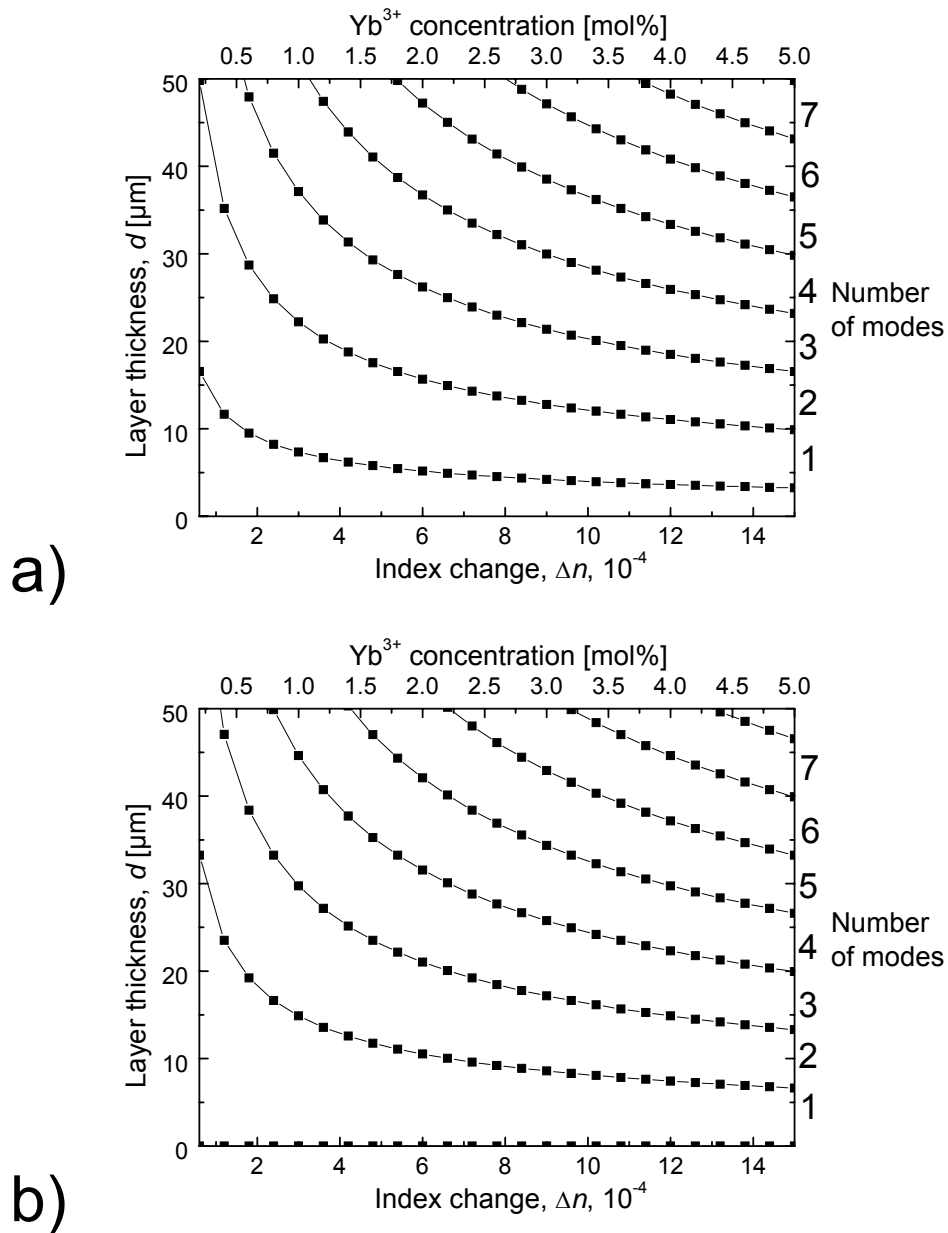


Fig. 6.3. Simulation of TE modes in surface (a) and buried (b) planar KYW:Yb waveguides at $\lambda = 0.98 \mu\text{m}$.

Fig. 6.3 shows the simulation of the cut-off for TE waveguiding modes in a KYW:Yb thin layer on a KYW substrate, as a function of the layer thickness, the refractive index change, and the respective Yb³⁺-concentration in the layer. Initial parameters used in equation (6.12) are $\lambda = 0.98 \mu\text{m}$, $n_s \equiv n_{\text{KYW}} = 2.010$ along the N_m principal axis at $\lambda = 0.98 \mu\text{m}$ (see. Fig. 2.7 from Sect. 2.1.3), and $n_f \equiv n_{\text{KYW:Yb}} = \chi_{\text{Yb}^{3+}} \times n_{\text{KYbW}} + (1 - \chi_{\text{Yb}^{3+}}) \times n_{\text{KYW}}$. Here, $\chi_{\text{Yb}^{3+}}$ is the molar fraction of Yb³⁺ with respect to Y³⁺, and $n_{\text{KYbW}} = 2.037$ along the N_m principal axis at $\lambda = 0.98 \mu\text{m}$ [puj02].

Both surface (a) and buried (b) waveguides are considered. For the surface waveguide, the asymmetry parameter $a > 0$ whereas for the buried case $a = 0$. For the surface waveguide with a given index profile, there is always a certain minimum thickness, below which no modes can propagate. In contrary, for the perfect symmetry of the buried waveguide, the fundamental mode does not have a cut-off, and it can exist even in a layer of an infinitesimal thickness.

Finally, the difference of refractive indices between the layer and substrate defines the *numerical aperture* of a waveguide, NA , as well as its acceptance angle θ_{accept} :

$$NA = \sin \theta_{\text{accept}} = \sqrt{(n_f^2 - n_s^2)}. \quad (6.13)$$

For instance, for a typical KYW:Yb layer with the Yb concentration of 1.8 mol%, $NA = 0.05$ and $\theta_{\text{accept}} = 2.9^\circ$.

Waveguide lasers

When a high-quality waveguiding layer is doped with an active lasing ion, a waveguide laser can be realized by placing the waveguide in a cavity with two mirrors. In this approach, both pump and laser light are guided in a thin layer over the whole waveguide length, which results in some considerable advantages of this geometry over conventional bulk laser media:

- high pump confinement over the whole waveguide length;
- high pump intensity;
- low threshold;
- good overlap between pump and oscillating beams;

The advantages become even more obvious in quasi-three-level lasers, which require a strong excitation density in order to reach leaser threshold. For instance, it follows from equation (2.12) from Sect. 2.3.2 that $P_{\text{thr}} \propto w_p^2$, where w_p is the mode waist of the pump beam. When the mode is guided, the waist is comparable with the thickness of the active layer. Thus,

confinement of the pump beam to a small guiding area decreases the threshold power, because high excitation density of active ions can be achieved at low pump power.

The concept of Yb-doped waveguide lasers has been investigated for different host materials, like Yb:YAG [han93, pel95], Yb:GGG [shi96], or Yb:LiNbO₃ [jon95]. The highest slope efficiency of 77% at a threshold of 43 mW and a maximum output power of 250 mW have been reported by Pelenc *et al.* for an LPE-grown planar 10 μm -thick Yb:YAG waveguide [pel95].

6.2 Surface and end-face polishing

The quality of the surface and both end-faces of the waveguide strongly affects coupling efficiency and light propagation. Therefore, surface and end-face polishing is an important step to prepare flat, defect-free faces, which are suitable for waveguide and laser experiments.

Surface polishing

Polishing of the layer surface was required to remove growth steps and solution residuals which remained after the LPE growth. Furthermore, by polishing an initially thick layer, a desired and uniform waveguide thickness could be obtained. The surface polishing was performed on a Logitech CL40 polishing machine. It consisted of two main steps:

1. Orienting the sample on a precision jig.
2. Polishing the layer surface using alumina suspensions.

Since the layer is grown on both sides of the substrate, directly placing the sample on the polishing jig does not ensure strict parallelism of the substrate-layer interface with respect to the jig surface. Therefore, the sample was mounted on a polishing jig with a low-melting organic wax, which acted as an intermediate layer between the sample and the jig. The sample inclination could be easily modified by heating the wax above the solidification temperature of about 50°C. The upper part of the substrate, which was not covered by the layer and, hence, coincided with the interface, was employed as a reference plane. The parallelism of the reference plane and the jig surface was controlled with a mechanical profilometer Sylvac 229. The angular precision of this alignment procedure is better than 0.05°.

The aligned and fixed substrate was polished on different polishing tissues provided by Struers[®]. Deagglomerated alumina ($\alpha\text{-Al}_2\text{O}_3$) suspensions with grain sizes from 5 to 0.1 μm were used. Alumina is a suitable polishing agent because it possesses a hardness of 9.0 according to Mohs' scale, which is higher than that of 4.5-5 for KYW. The initial polishing

started on a hard tissue using large alumina grains to obtain a high removal rate. The fine polishing was done on a soft, resilient tissue with small alumina grains. The standard polishing procedure is given in Table 6.1.

Table 6.1. Process conditions for polishing KYW.

Step	Alumina grain size, μm	Tissue	Hardness / Resilience	Rotation rate, rpm	Time, min
1	5	MD-Plan	Hard / Very low	25-30	10-30
2	1	MD-Dac	Hard / Medium	30-50	10-20
3	0.1	MD-Dur, Nap	Soft / High	50-70	1-2

The polishing time was determined mainly by the amount of layer material that had to be removed to obtain a desired thickness. The removal rate was controlled with a precision of $\pm 1\mu\text{m}$ using a micrometer installed on the polishing precision jig. A spring inside the polishing jig allowed us to vary the load on the sample continuously from 0 to 15 N. We found that the optimum sample load is 0.15–0.2 N for a layer area of 0.7 cm^2 , which corresponds to a maximum pressure of 0.2 Bar.

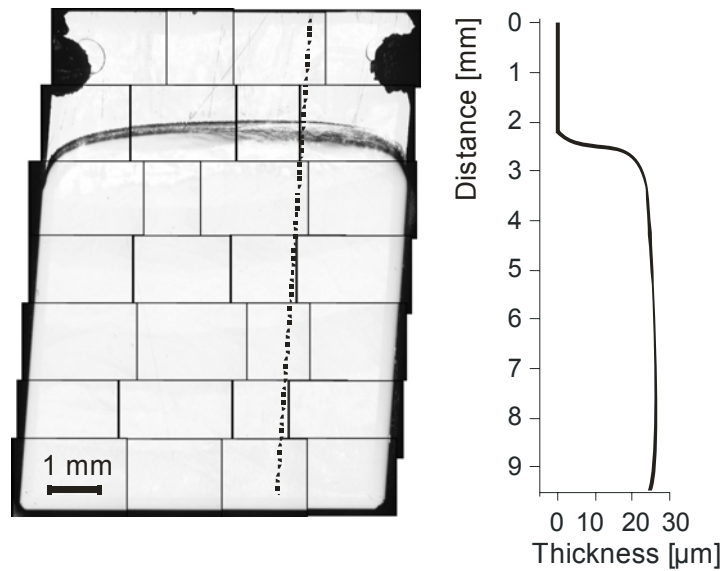


Fig. 6.4. Polished surface of a KYW:Yb layer together with the respective thickness profile.

The composite DIC photograph of a polished layer is shown in Fig. 6.4. The layer thickness is uniform over the whole substrate length, as can be seen from the respective thickness profile. A slight curvature of the thickness profile is caused by a high resilience of the tissue for final polishing.

The flatness and surface roughness of the polished layers were inspected with a ZYGO interferometer. A surface line profile taken in the center of the polished sample is given in Fig. 6.5.

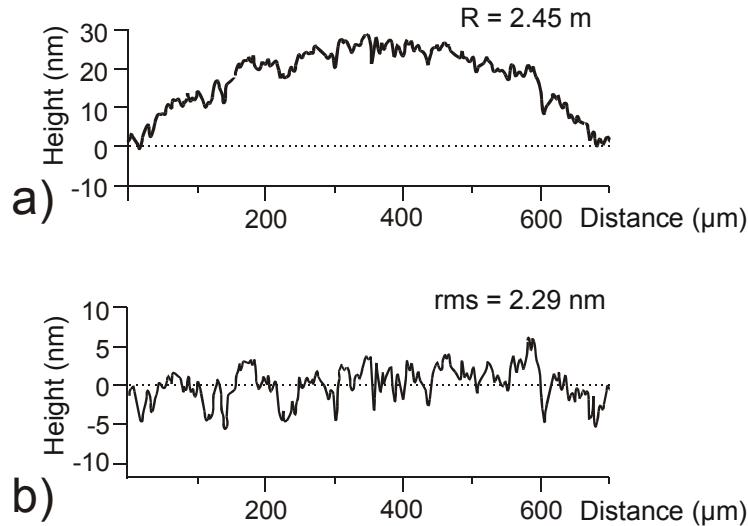


Fig. 6.5. Line profile of the polished layer surface inspected with ZYGO interferometer: (a) non-leveled curved profile; (b) profile leveled with a radius of curvature of 2.45 m.

The surface is not perfectly flat but exhibits a small bend with a curvature radius of 2.45 m. This curvature implies a maximum layer thickness in the center of the substrate, whereas the layer edges are thinner. However, such long-range variations in layer thickness do not seriously affect light propagation in the waveguiding layer. The same line profile, leveled with respect to the curvature radius, exhibits a root-means-square (rms) value of only 2.29 nm for the local surface roughness. This small roughness should ensure very low scattering losses of light propagating in the layer.

End-face polishing

The polishing of waveguide end-faces is often not a trivial issue, because a small end-face inclination (in the order of 1°) or rounded edges can result in a decrease of the in- and out-coupling efficiency by 10-20% [ger01]. Therefore, we employed a special sample holder for the end-face polishing, which is shown in Fig. 6.6.

The sample is placed between two glass plates, each 1 mm thick. The layer is separated from the glass plate by a very thin (5-10 μm) gap filled with solidified wax. Thus, the sample and protecting glass plates behave like a single piece during polishing, and the chamfering of the inner layer edge becomes minimal. The holder has a flat crosspiece, which presses the sample and glass plates with two screws to a metal bar. The bar is fixed on the metal base also with two screws. Since the bar has the shape of a parallelepiped, it can be turned upside-down allowing for the other waveguide end-face to be polished. If the position

of the crosspiece remains constant, both polished end faces are strictly parallel with a maximum measured deviation of 0.02° .

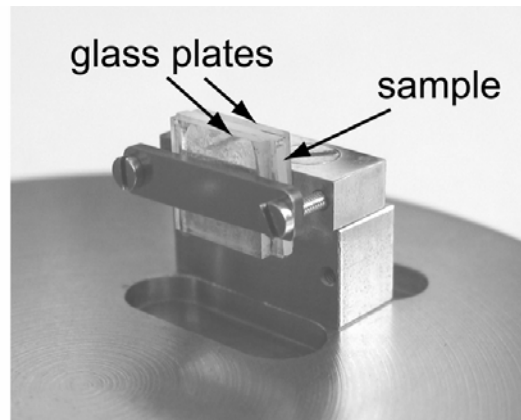


Fig. 6.6. Sample holder used for the end-face polishing.

The polishing procedure for end-faces was similar to that given in Table 6.1. Since the hardness of silica glass is 7.0 on Mohs' scale, the maximum applied sample pressure was increased to 0.5 Bar.

Figure 6.7 illustrates the polished end face of a KYW:Yb layer brought in close contact with the glass plate. The layer thickness is about $37\ \mu\text{m}$. The line profile indicated in Fig. 6.7a shows that the layer face is flat and tilted by about 0.1° from an ideal right angle. The inset in Fig. 6.7b confirms that the edge is sharp and its rounding is negligible as compared to the layer thickness.

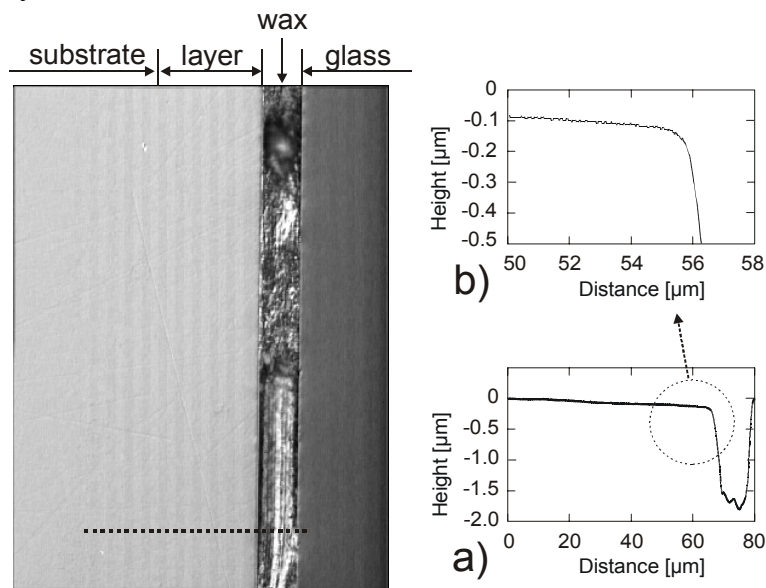


Fig. 6.7. Polished end-faces of a KYW:Yb layer. (a) Depth profile and (b) enlargement of the near-edge region of the layer.

6.3 Waveguiding and beam profiles

The prepared surface, buried, and channel KYW:RE layers were tested as passive and active optical waveguides. The experimental set-up that was used for waveguide investigation is shown in Fig. 6.8.

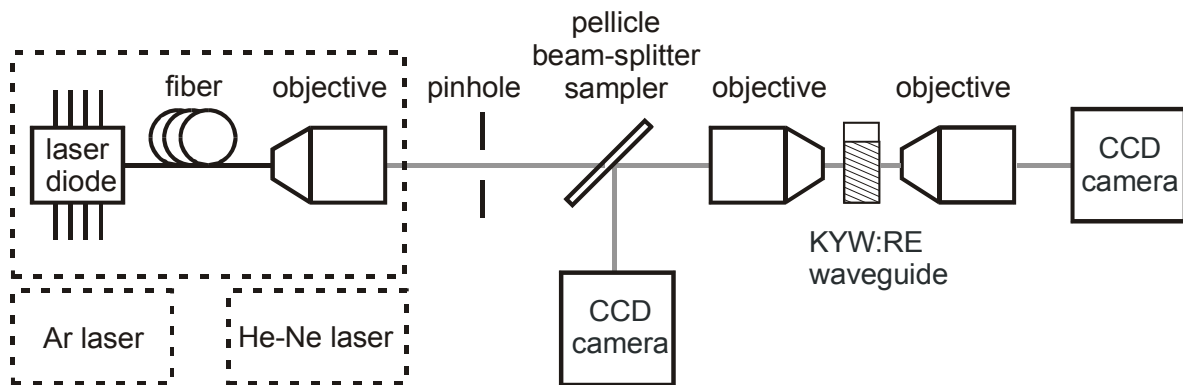


Fig. 6.8. Experimental set-up for optical waveguide investigation.

The Yb-doped waveguides are pumped with a Lumix LU0980M250 laser module, which consists of a fiber-pigtailed InGaAs laser diode mounted on a heat-removing copper base. The laser diode is driven with a Thorlabs LDC210 laser diode controller (not shown in Fig. 6.8). Due to a fiber Bragg grating, the laser diode operates in a single-mode regime and delivers a maximum output power of 300 mW at 980.8 nm. The output beam from the fiber tip is about 80% linearly polarized.

Alternatively, the KYW:RE waveguides are investigated with an Ar ion laser (488 nm, maximum output power up to 15 W) or with a He-Ne laser (632.8 nm, maximum output power 5 mW). Different pump sources provide the possibility to observe both passive and active waveguiding. In the case of passive waveguiding, only incoupled light propagates in the layer, whereas in active waveguiding, a part of the pump light is absorbed by the active ions and the generated fluorescence is guided in the same layer.

The parallel pump beam with a waist of 1 mm passes through the pinhole and splits on a thin (2 μm) nitrocellulose membrane, which acts as a beam-sampler. The sampler has a reflectivity/transmission ratio of 8/92% in the wavelength range of 400-2400 nm. The transmitted light is focused with a microscope objective on the incoupling end-face of the waveguide. A CCD-camera, installed at 45° to the beam-splitter sampler, allows us to monitor the incoupling spot by observing the light back-reflected from the waveguide face. The

incoupling spot has a diameter of 5 to 40 μm , depending on the magnification of the objective and the laser wavelength.

The waveguide is positioned on a 6-axis rotation and translation stage allowing optical alignment with the laser beam. The waveguide end-faces are polished to optical quality, as described in Sect. 6.2. The waveguide orientation corresponds to propagation along the [001] crystallographic direction (*c*-crystallographic axis) for most samples, however other orientations can be used as well after appropriate polishing. The out-coupled light is imaged onto the sensor of a CCD-camera with another objective.

Fig. 6.9a shows the polished end-face of a planar surface KYW:Tb waveguide. The waveguiding region is a 2.5- μm thick 10 mol% Tb:KYW layer grown from the chloride solvent. The waveguide is 4 mm long.

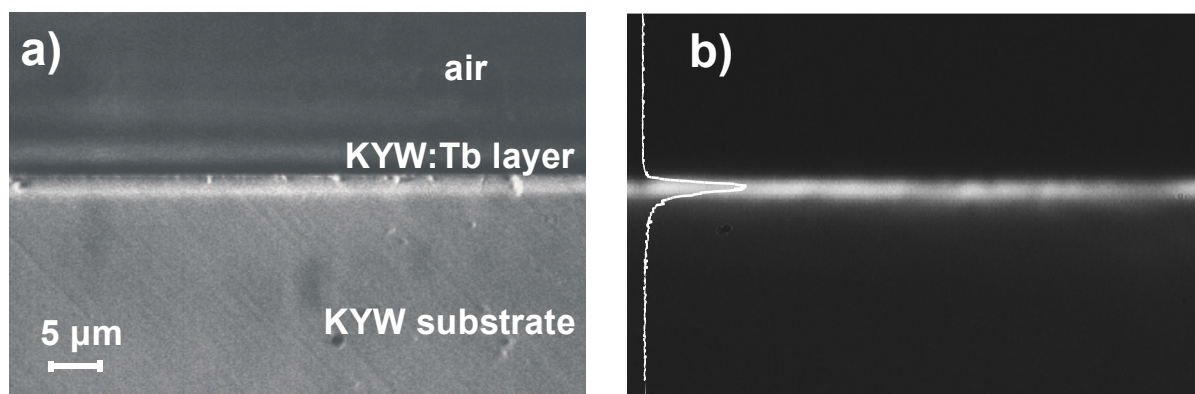


Fig. 6.9. (a) Optical photograph of an end-face of a 10 mol% Tb:KYW surface waveguide.

(b) Near-field image of the guided Tb³⁺ fluorescence outcoupled from the waveguide.

Ar-ion laser light at 488 nm is coupled into the KYW:Tb layer with a 25 \times objective. The guided pump light excites the Tb³⁺ ions, which emit fluorescence in the yellow and red spectral regions. Because the fluorescence is emitted over a solid angle of 4π steradians, only a small part of fluorescence is guided together with the non-absorbed pump beam. A filter is used to block the residual pump radiation transmitted through the waveguide. The guided fluorescence outcoupled from the sample is shown in Fig. 6.9b. The intensity of outcoupled fluorescence in the horizontal direction is not uniform because of several defects at the layer edge. The vertical profile corresponds to the beam intensity in the center of the image.

Another example of a surface waveguide is shown in Fig. 6.10. The 1.2 mol% Yb:KYW layer was grown from the K₂W₂O₇ solvent and the layers thickness is 11 μm . This combination of thickness and doping of the surface waveguide supports propagation of only the fundamental TE mode, as predicted by Fig. 6.3. The waveguide is 6 mm long.

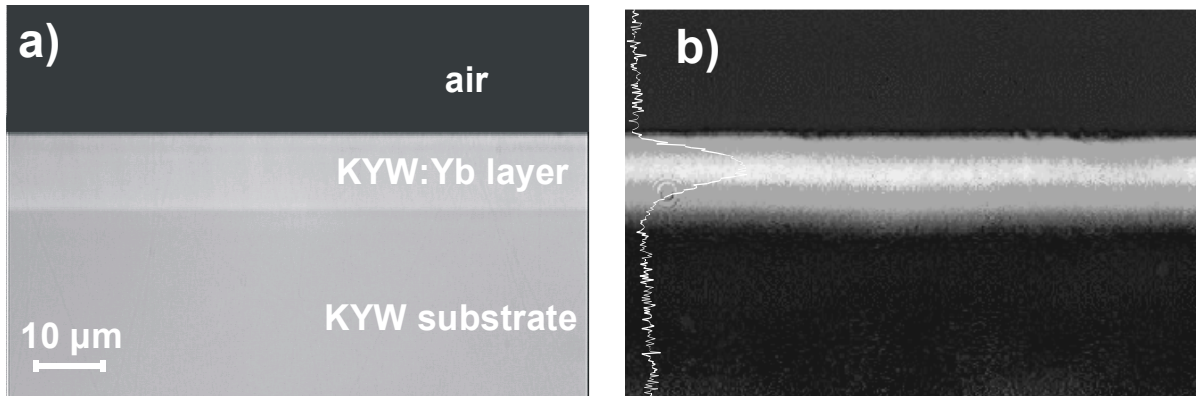


Fig. 6.10. (a) Optical photograph of the end-face of a 1.2 mol% Yb:KYW surface waveguide. (b) Near-field image of the guided pump light and Yb³⁺ fluorescence outcoupled from the waveguide.

The pump light from the laser diode is coupled into the layer with a 40× objective. The Yb³⁺ ions absorb a part of the pump light at 981 nm and emit fluorescence at 980-1050 nm. Fig. 6.10b shows the pump light and Yb³⁺ fluorescence outcoupled from the waveguide and collimated with a 40× objective. The presence of a background signal in the bulk on the intensity profile indicates some leaking of light into the substrate. It can be explained by a non-perfect incoupling, because the NA of 0.65 for the 40× incoupling objective far exceeds the NA of 0.04 calculated for the 1.2 mol% Yb:KYW layer on KYW.

A symmetric mode-field distribution of the outcoupling light is assured in buried waveguides. Fig. 6.11a shows a 22 μm-thick KYW:Yb buried layer overgrown with a 25-μm thick KYW overlay using the K₂W₂O₇ solvent. Laser diode light at 980.8 nm is injected with a 10× objective and transmitted pump light and fluorescence are outcoupled with a 16× objective.

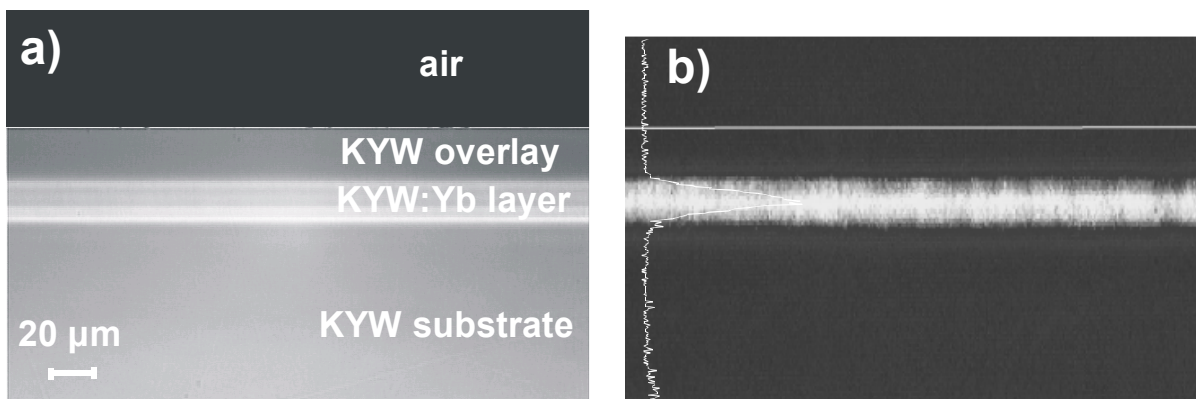


Fig. 6.11. (a) Optical photograph of the end-face of a 1.8 mol% Yb:KYW buried waveguide. (b) Near-field image of the guided pump light and Yb³⁺ fluorescence.

The vertical profile of the outcoupled pump light intensity is nearly symmetric because of the equal refractive index change on both sides of the active layer (Fig. 6.11b). The shape of the intensity distribution is close to a Gaussian distribution. However, at least 3 TE modes are supported $\lambda = 981$ nm by this 22- μm thick buried waveguide in the vertical direction.

Finally, Fig. 6.12 represents a channel waveguide. The selected KYW:Yb channel is 18 μm in height and 200 μm in width. The channel length is 6 mm along the [101] crystallographic direction. Pump light from a He-Ne laser at 632.8 nm is coupled into the waveguide with a 40 \times objective.

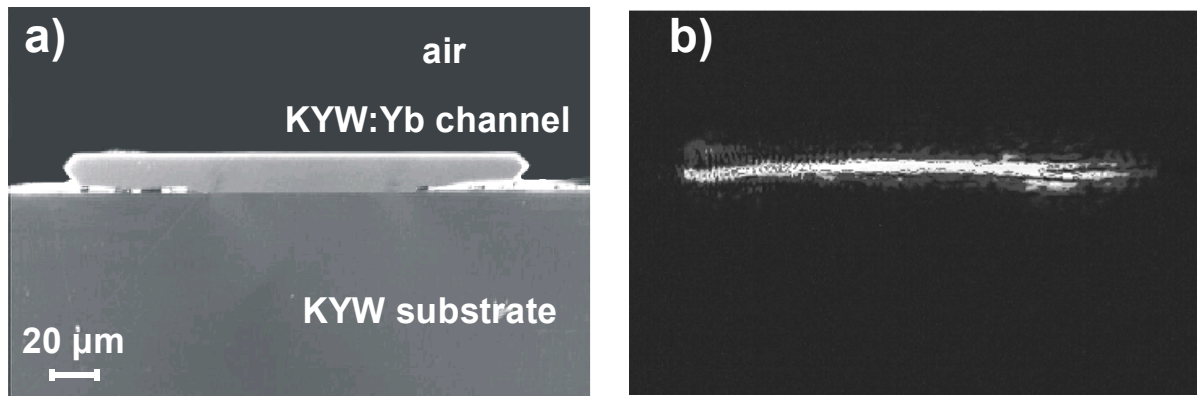


Fig. 6.12. (a) Optical photograph of the end-face of a 1.7 mol% Yb:KYW channel waveguide. (b) Near-field image of the guided laser light outcoupled from the channel.

The outcoupled laser light shown in Fig. 6.12b generally coincides with spatial outline of the wide channel. However, the intensity profile is not uniform over the channel width. This slightly inferior waveguiding performance, as compared with planar structures, is attributed to the unpolished surface of the channel containing growth steps and flux residuals. Three pairs of transversal outgrowths, which adjoin the channel, also lead to some leakage of the pump light. These outgrowths are formed during the growth due to the presence of 3 horizontal cross-bars in the shielding mask (Fig. 4.20 in Sect. 4.7.1). However, by use of a better mask design and smaller channel width, the channel waveguiding performance can be improved.

6.4 Loss measurements

Signal light traveling through an optical waveguide always exhibits attenuation. This attenuation is generally attributed to three different loss mechanisms: absorption, scattering and radiation [hun91].

Absorption loss is important in semiconductors and other materials, where the propagating light can be considerably absorbed due to optical or interband transitions and free carrier absorption. In KYW:RE layers, the absorption comes from doped RE³⁺ ions if the wavelength of guided light matches an absorption band of the RE³⁺ ion. The pump light is absorbed according to the Lambert-Beer law

$$I_l = I_{\text{in}} \exp[-\alpha(\lambda_p)l], \quad (6.14)$$

where I_{in} is the initial coupled intensity and I_l is the residual pump intensity after propagating length l . As described in Sect. 2.3.2, $\alpha(\lambda_p)$ is the absorption coefficient at the selected pump wavelength, which is a product of the effective absorption cross-section and the ground-state population:

$$\alpha(\lambda_p) = \sigma_a(\lambda_p)N_1. \quad (6.15)$$

There are two types of scattering loss in an optical waveguide: volume scattering and surface scattering. Volume scattering is caused by imperfections, such as voids, contaminant atoms, and crystalline defects within the volume of the waveguide. Surface scattering comes from interface defects and roughness of the surface waveguide. In both cases, the scattered intensity is proportional to $1/\lambda_p^4$, so that propagating light with shorter wavelength is more heavily scattered than that with longer wavelength.

Radiation losses into surrounding media from either planar or straight channel waveguides are generally negligible for well-confined modes that are far from cutoff. In typical waveguides of reasonably good quality, radiation losses can often be neglected compared to scattering and absorption losses.

Hence, the total attenuation of the guided light can be expressed with a modified Lambert-Beer law

$$I_l = I_{\text{in}} \exp[-(\sigma(\lambda_p)N_1 + \alpha_{\text{scat}})l], \quad (6.16)$$

where α_{scat} is the additional absorption coefficient that corresponds mainly to scattering losses. The value of α_{scat} represents the crystalline quality of the waveguide and both interfaces.

To evaluate the layer quality and to determine α_{scat} for the grown waveguides, we have used a method based on the observation of the fluorescence intensity coming out of an active surface waveguide. For instance, when a KYW:Yb planar waveguide is pumped with laser light at 980.8 nm, the subsequent Yb³⁺ fluorescence at 980-1050 nm is emitted over a solid angle of 4π steradians. In the absence of nonlinear spectroscopic processes, the

fluorescence intensity in a certain point is directly proportional to the intensity of the residual pump light guided to that point. Knowing the decay of the pump light due to absorption in the waveguide, one can estimate α_{scat} from equation (6.16).

The experimental set-up for the loss measurement is shown in Fig. 6.13. Laser light at 980.8 nm is focused into a 45- μm thick 1.7 mol% Yb:KYW layer with a lens having a focal length $f = 120$ mm. The laser-beam diameter is approximately 4 mm at the lens plane and 20 μm at the incoupling face. Hence, the laser light is focused at the waveguide entrance with $\text{NA} = 0.017$, which is far below the acceptance $\text{NA} = 0.05$ for the 1.7 mol% Yb-doped layer. This enables better light incoupling as compared to the coupling using microscope objectives, which have larger NA. A Glan-Taylor polarizer maintains the polarization of the coupled laser light so that $E // b // N_p$, for which the effective absorption cross-section of Yb^{3+} is well defined, $\sigma(980.8 \text{ nm}) = 3.35 \times 10^{-20} \text{ cm}^2$ (Sect. 2.2.1).

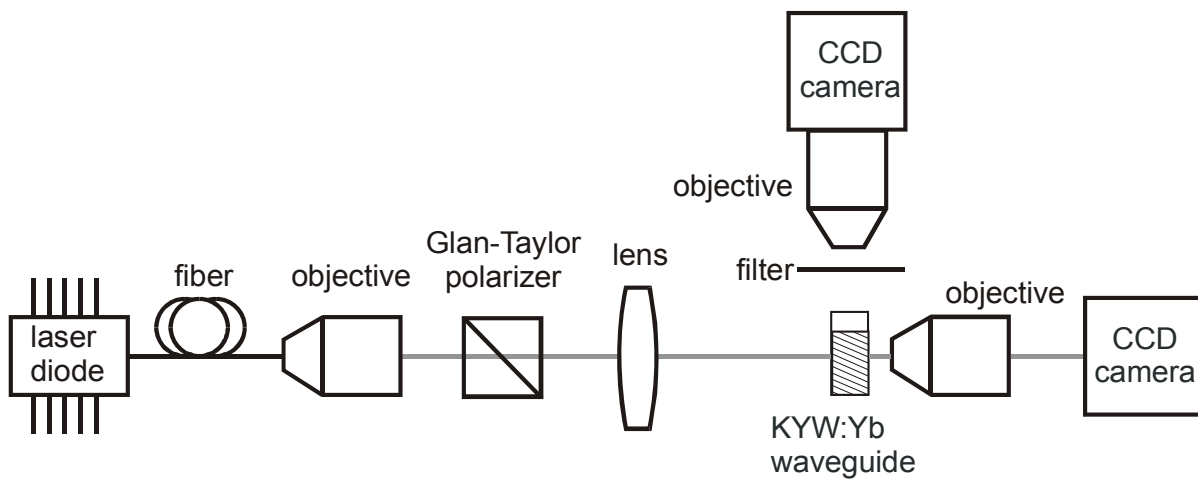


Fig. 6.13. Experimental set-up for loss measurement.

The Yb^{3+} fluorescence is recorded with a CCD camera fixed above the waveguide surface. A filter, which transmits about 99% at 1025 nm and only 2% at 980.8 nm, is used to detect only the fluorescence light and to block the pump signal.

A rather strong IR fluorescence along the entire waveguide length is observed (Fig. 6.14a). The 3D profile of the relative fluorescence intensity illustrates well the fluorescence decay (Fig. 6.14b).

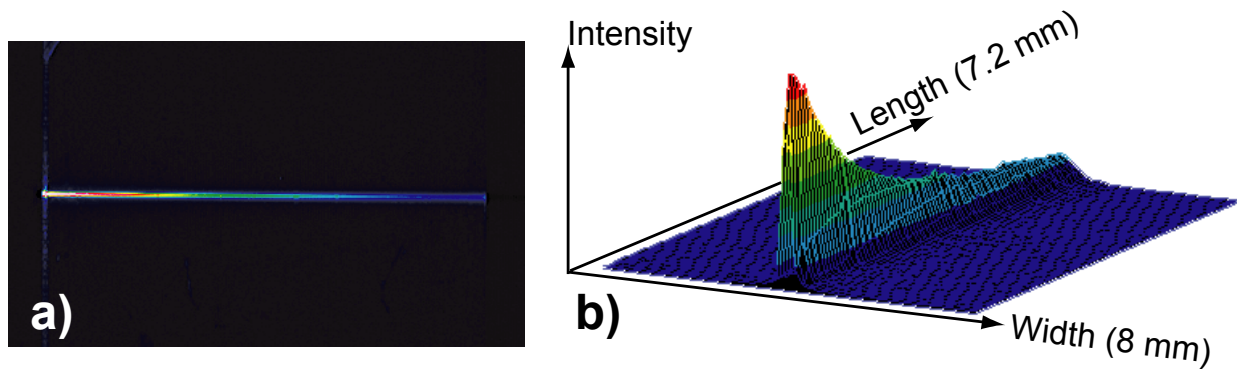


Fig. 6.14. IR fluorescence from a 1.7 mol% Yb:KYW waveguide when propagating laser light at 980.8 nm. a) Two-dimensional and b) three-dimensional intensity profiles.

Since the intensity peak broadens over the waveguide length due to the pump beam divergence, an integration of the peak is required in order to evaluate the total fluorescence intensity after a given propagation length. Fig. 6.15 represents the fluorescence intensity decay obtained after the peak integration.

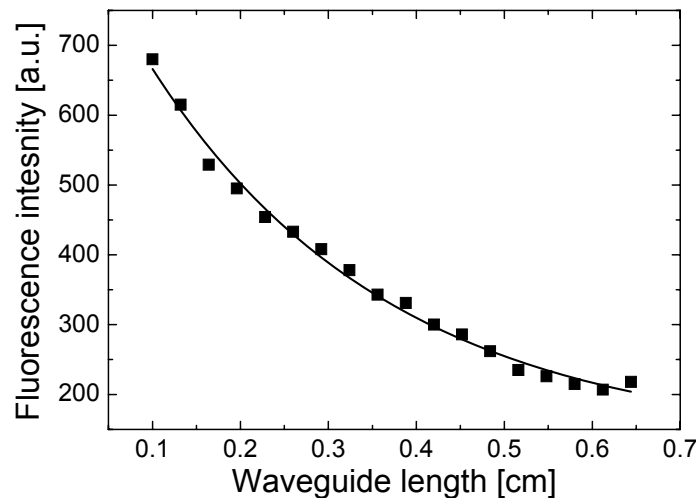


Fig. 6.15. Laterally integrated fluorescence intensity over the waveguide length.

Using $\sigma(980.8 \text{ nm}) = 3.35 \times 10^{-20} \text{ cm}^2$ and $N_1 \approx N_{\text{tot}} = 1.08 \times 10^{20} \text{ cm}^{-3}$ for the 1.7 mol% Yb:KYW waveguide, from equation (6.16) we obtain $\alpha_{\text{scat}} = 0.043 \text{ cm}^{-1}$, which amounts to a propagation loss of 0.19 dB cm^{-1} at 980.8 nm. The obtained value for the scattering losses is consistent with literature data for high-quality oxide layers grown by LPE [jel98].

The propagation losses in the grown KYW:RE layers have also been evaluated by Dr. Camelia Borca (Institute of Imaging and Applied Optics, EPF Lausanne) [bor05]. A $4 \mu\text{m}$ -thick, 1.8 mol% Yb:KYW planar layer grown by LPE during this thesis work was structured

with He⁺-ion implantation to produce 8-12 μm wide channels. Laser light at 632.8 nm was coupled into the channels with a single-mode fiber HP630. In one case the guided light was outcoupled into a single mode fiber, in the other into a multimode fiber AF550. The decrease of guided light power due to the waveguide scattering could be estimated with approximative formula

$$L_{\text{scat}} = P_{\text{in}} + P_{\text{out}}^{\text{S}} - 2 P_{\text{out}}^{\text{M}}. \quad (6.17)$$

Here, L_{scat} is the scattered power, P_{in} is the initial laser power, $P_{\text{out}}^{\text{S}}$ and $P_{\text{out}}^{\text{M}}$ are the powers outcoupled into the single-mode and multimode fibers, respectively. The calculated propagation losses were 0.5-0.7 dB cm⁻¹ at 633 nm. Taking into account that the scattered intensity is proportional to $1/\lambda_p^4$, these losses are lower than those expected from the loss of 0.19 dB cm⁻¹ at 980.8 nm. Moreover, since the channels possess side barriers created by implanted He⁺ ions, their presence should induce additional scattering losses. A possible reason is the difference in the layer thickness. A thicker waveguide implies higher propagation losses because it allows for the propagation of higher-order modes, which normally exhibit higher losses than the lower-order modes.

Finally, the propagation losses in the grown waveguides have been evaluated during laser experiments described in next Sect. 6.5. Depending on the waveguide thickness and doping concentration, the obtained propagation losses vary from 0.06 to 0.18 dB cm⁻¹. Again, the higher losses were measured for thicker waveguides investigated.

6.5 Planar waveguide laser based on KY(WO₄)₂:Yb

Laser experiments with samples prepared during this thesis were performed by Simon Rivier, Dr. Valentin Petrov, and Dr. Uwe Griebner at Max-Born-Institute for Nonlinear Optics and Ultrafast Spectroscopy (Germany).

One buried ($d = 17 \mu\text{m}$) and two surface ($d = 17$ and $35 \mu\text{m}$) KYW:Yb waveguides with polished end- and surfaces, each about 6 mm long and uncoated, were selected for laser experiments. Firstly, an astigmatically compensated Z-shaped cavity was chosen (Fig. 6.16a). The planar KYW:Yb waveguides were positioned at the Brewster angle of 64° between two folding mirrors with a radius of curvature ROC = -10 cm, such that the resonator waist is located at both end-faces of the waveguide and negligible diffraction losses occur for the

resonator mode at the waveguide interfaces. The waveguide orientation corresponded to propagation approximately along the N_g principal optical axis and polarization along the N_m axis (Fig. 6.16b). The sample was mounted on a copper plate without active cooling. The KYW:Yb layers were pumped in a single pass by a tunable CW Ti:Sapphire laser at 980.5 nm. Due to the high absorption cross-section of $\approx 1.33 \times 10^{-19} \text{ cm}^2$ at the pump wavelength of 980.5 nm, the single-pass low-signal absorption of the 1.8 mol% Yb:KYW layer was $>99\%$. However, part of the mode field of the guided pump beam did not penetrate the active layer, resulting in a pump absorption of 56%.

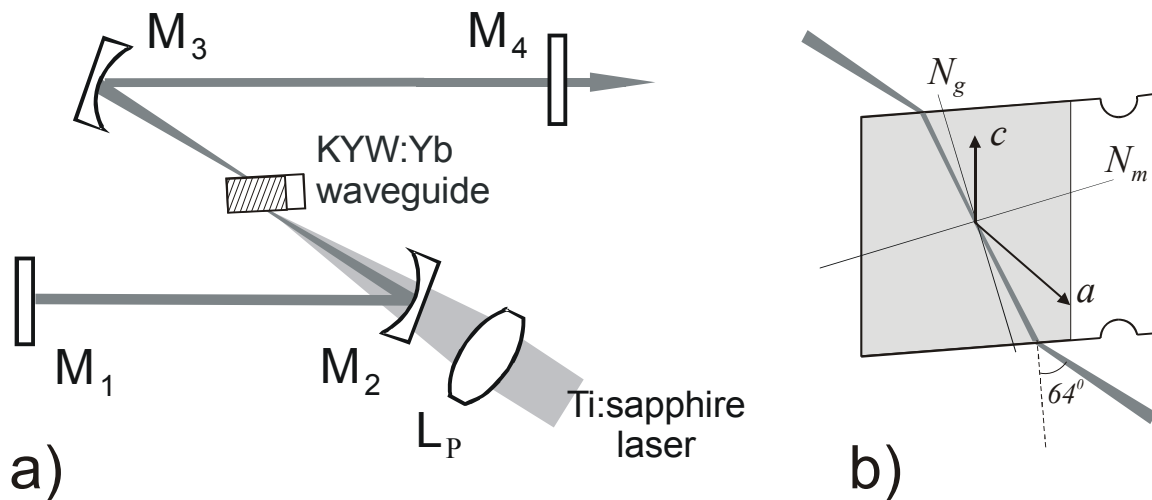


Fig. 6.16. (a) Setup of the Z-shaped laser cavity: L_p – focusing pump lens, M_1 , M_2 , M_3 – high reflecting mirrors (M_2 , M_3 ; ROC = -10 cm), M_4 – plane output coupler.

(b) Orientation of the laser beam propagation with respect to the principal optical axes.

Independent of the output coupler transmission T , which was chosen between $T = 1.2$ and 13.5%, stable CW oscillation near $\lambda = 1025 \text{ nm}$ could be achieved for all waveguides investigated. For an example, see Fig. 6.17a. Since reabsorption of oscillating laser light in this quasi-three-level laser system could be greatly reduced due the high pump-light confinement in the active layer, the spectral laser emission corresponds to the maximum of the gain curve. The output was 95% linearly polarized.

The laser threshold of the 35- μm thin KYW:Yb layer was reached at an absorbed pump power of about 100 mW. Using an output coupler with a transmission of $T_{OC} = 5.1\%$, the maximum output power amounted to 290 mW, resulting in a slope efficiency of $\eta = 46\%$ with respect to the absorbed pump power, as measured under lasing conditions (Fig. 6.17b). The slope efficiency was maximum for $T_{OC} = 7.6\%$ and amounted to 50%. Applying a chopper with a duty cycle of 10%, the output power decreased ten times. Hence, it can be

concluded that no thermal problems occur up to the maximum applied pump power of 2 W despite the absence of active cooling. The observed far-field intensity distribution indicated that the laser output is close to the diffraction limit and the resonator mode is well matched within the physical dimensions of the planar waveguide.

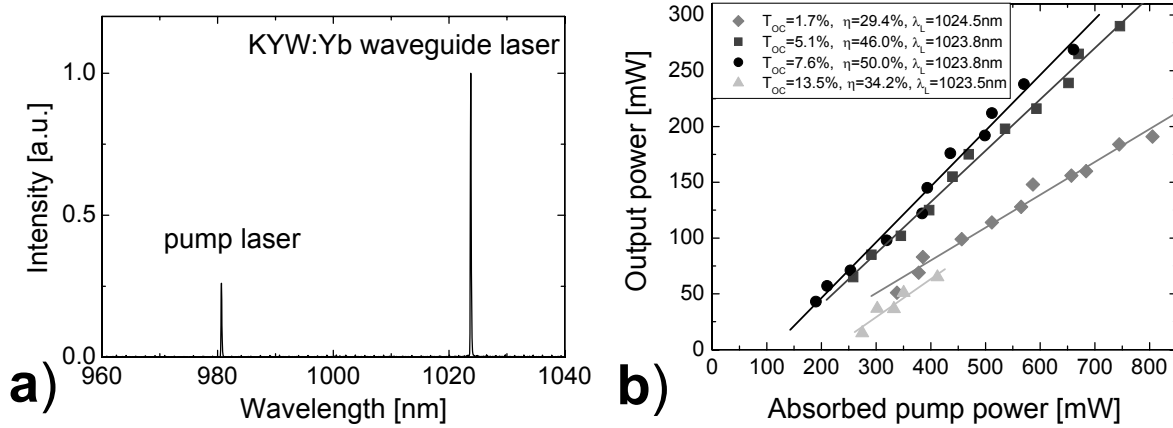


Fig. 6.17. Laser performance of the 35- μm thin, 1.8 mol%Yb:KYW layer: (a) Spectral record of the laser emission and the residual pump radiation; (b) Laser output power versus absorbed pump power for different transmissions of the output coupler.

The best laser performance was achieved with the 17- μm thin surface waveguide doped with 1.2 mol% Yb^{3+} . With a 3.7%-transmission output coupler the laser threshold was only 80 mW of absorbed pump power and the maximum output power amounted to 290 mW, resulting in a slope efficiency versus absorbed pump power of $\eta = 67.4\%$. A maximum slope efficiency of 80.4% was obtained for $T = 6.2\%$ (Fig. 6.18a).

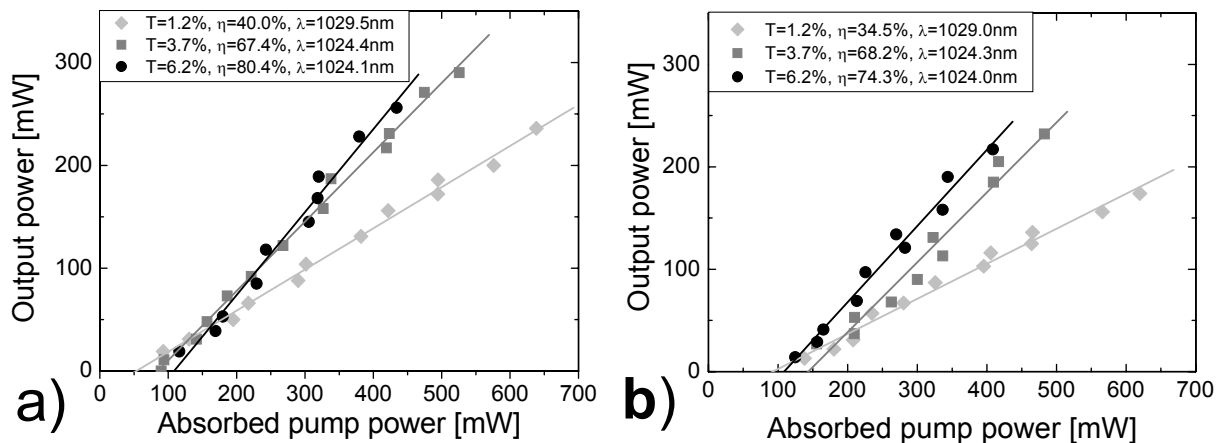


Fig. 6.18. Laser output power versus absorbed pump power of (a) 17- μm thick surface and (b) 17- μm thick buried KYW:Yb planar waveguides for different transmissions of the output coupler.

Although a buried waveguide should, in principle, exhibit lower propagation losses, the laser performance in the buried 2.4 mol% Yb:KYW waveguide was slightly inferior (Fig. 6.17b) presumably as a result of the higher doping concentration, which led to higher reabsorption losses.

Cavity round-trip losses derived from the obtained slope efficiencies using equation (2.15) from Sect. 2.3.2 equal to 4.8%, 1.8%, and 2.2% for 35- μm thick surface, 17- μm thick surface, and 17 μm -thick buried waveguides, respectively. Attributing these losses completely to waveguide propagation losses leads to an upper limit of 0.18 dB cm^{-1} for the waveguide losses. This value is in good agreement with 0.19 dB cm^{-1} obtained for the non-lasing case in Sect. 6.4.

The observed laser thresholds were compared with theoretical values predicted from equation (2.12) in Sect. 2.3.2:

$$P_{\text{thr}} = \frac{1}{\tau} \frac{2\sigma_a N l - \ln[(1-L)R_1 R_2]}{2(\sigma_e + \sigma_a)} \frac{1}{\eta_q} \pi w_p^2 \frac{hc}{\lambda_p}. \quad (6.18)$$

We used the parameters listed in Table 6.2 to estimate the absorbed power threshold for the 17- μm thin Yb:KYW surface waveguide.

Table 6.2. Parameters for the calculation of the expected threshold pump power for a 17- μm thin 1.2 mol% Yb:KYW waveguide laser.

Parameter		Value	Reference
Radiative lifetime of Yb ³⁺	τ	0.230 ms	Sect. 2.2.1
Stimulated emission cross-section at 1024.4 nm	σ_e	$3.0 \times 10^{-20} \text{ cm}^{-3}$	Eqn. (2.3), Sect. 2.2.1
Stimulated absorption cross-section at 1024.4 nm	σ_a	$8.1 \times 10^{-21} \text{ cm}^{-3}$	Fig. 2.10, Sect. 2.2.1
Total Yb ³⁺ concentration	N	$7.60 \times 10^{19} \text{ cm}^{-3}$	Calculated for 1.2 mol% Yb:KYW
Waveguide length	L	6 mm	Sect. 6.5
Round-trip cavity loss	L	1.8%	Sect. 6.5
Reflectivity of cavity mirrors	R_1	100%	Fig. 6.15
Reflectivity of output coupler	R_2	96.3%	Fig. 6.17a
Quantum efficiency	η_q	1	Assumed
Pump beam radius	w_p	8.5 μm	$\approx \frac{1}{2}$ waveguide thickness
Pump wavelength	λ_p	980.5 nm	Fig. 6.15

Inserting the parameters from Table 6.2 into equation (6.18) leads to an expected absorbed power threshold $P_{\text{thr}} = 21$ mW. This value is smaller than the observed $P_{\text{thr}} \approx 85$ mW for $R_2 = (100-T) = 96.3\%$ and $\lambda_L = 1024.4$ nm (Fig. 6.18a). The main source of the discrepancy between the calculated and observed threshold is likely to be pump beam divergence in the horizontal direction. Indeed, equation (6.18) is valid for the space-independent model, in which the pump beam waist is assumed to be constant over the active medium length. Obviously, this is not the case for the planar waveguides, where the focused pump beam spreads considerably in the unguided horizontal plane. In order to estimate the averaged w_p to be inserted in equation (6.18), we assume the natural divergence of the pump Gaussian beam in the horizontal direction and average the pump beam waist weighted by the transmitted power at a given length. For instance, for a pump beam spot of 22 μm in diameter, focused on one end-face of the 6-mm long waveguide, the averaged pump beam diameter is calculated to be 34 μm . Inserting $w_p = 17$ μm into equation (6.18), we obtain $P_{\text{thr}} = 82$ mW, which is very close to the observed value.

“True” waveguide laser

In order to demonstrate the waveguiding effect of the layers under lasing conditions employing an external cavity, a simple linear laser cavity was used. In this second resonator setup (Fig. 6.19), we compared the laser performance of bulk and waveguide Yb-doped samples versus the resonator length L_{res} . For the chosen, nearly hemispherical resonator with a radius of curvature (ROC) of the output coupler equal to -5 cm, the losses are expected to increase rapidly when the resonator length L_{res} exceeds this ROC and the resonator becomes unstable.

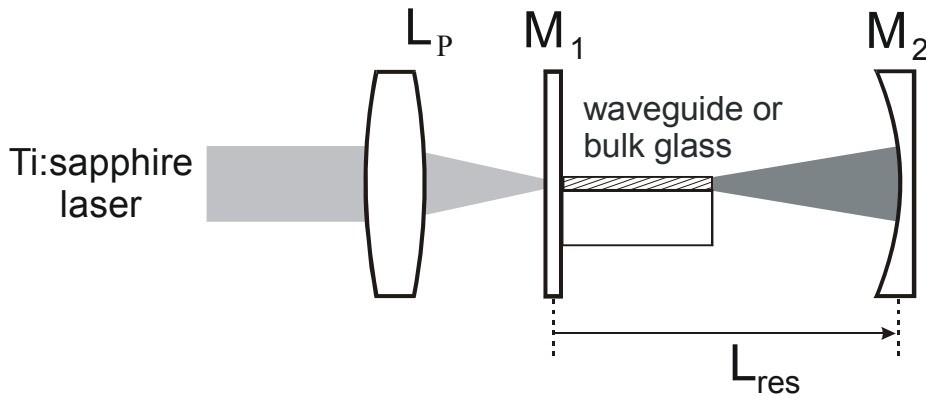


Fig. 6.19. Setup of the linear laser cavity: L_p – focusing pump lens, M_1 – plane dichroic mirror, M_2 – output coupler (ROC = -5 cm).

The active media were positioned as close as possible to the plane mirror and an index-matching liquid was used to minimize the Fresnel loss. The samples were end-pumped through the plane dichroic mirror by the same CW Ti:sapphire laser near 980 nm. The focused pump spot had a waist diameter of 22 μm . The CW output powers measured versus resonator length for a glass:Yb bulk sample and a 17- μm thick KYW:Yb surface waveguide are shown in Fig. 6.20. The bulk laser operated for resonator lengths between 43 mm and 49.9 mm. No lasing could be achieved for resonator lengths longer than 49.9 mm, as expected from the resonator stability criterion. When replacing the 6-mm long bulk by the waveguide sample, laser operation could be achieved for resonator lengths extending to 54 mm.

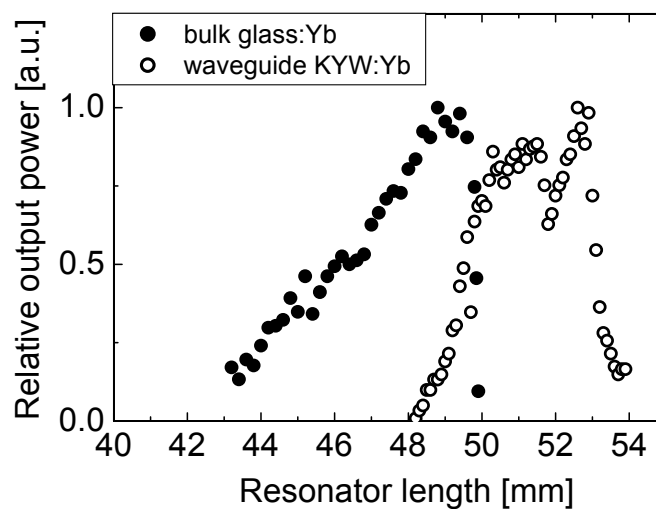


Fig. 6.20. Comparison of relative laser output power versus resonator length L_{res} for a 6-mm long glass:Yb bulk sample and a 6-mm long 1.2 mol% Yb:KYW surface waveguide.

The shift between the two curves in Fig. 6.19 indicates that the waist of the resonator mode is moved from the plane mirror toward the opposite waveguide end-face without substantially changing the resonator losses, i.e., the laser resonator remains stable even for $L_{\text{res}} > \text{ROC}$ [gri99]. This is a clear indication of the guiding behavior of the active layer. The observed cavity extension is shorter than the waveguide length, because the positive waveguiding effect occurs in only one transverse direction.

In this simple resonator configuration, maximum output powers of 158 mW at 1040 nm and 121 mW at 1025 nm for resonator lengths of 48.8 mm and 52.6 mm were obtained at $T = 1\%$ with the glass:Yb bulk sample and the KYW:Yb waveguide, respectively. The strong decrease of the output powers for smaller resonator lengths is due to the inferior overlap between the pump and resonator modes as well as inferior coupling into the waveguide.

7. Conclusions and Outlook

During this thesis work, the growth of high-quality KYW:RE thin layers has been performed using the LPE technique. Low-loss light guiding and efficient laser operation have been demonstrated in the prepared KYW:RE waveguides.

It has been proven that LPE remains a reliable and suitable method for the thin-layer fabrication of complex oxide materials, because LPE operates at near-equilibrium conditions. A proper selection of growth parameters, like solution supersaturation, lattice misfit and substrate orientation, enables the growth of high-quality KYW:RE layers with thicknesses ranging from 10 to 100 μm and RE^{3+} concentrations ranging from 0.2 to 3 mol% with respect to Y^{3+} . Numerical simulations of the liquid flow in the growth crucible helps to optimize the substrate rotation rate in order to obtain uniform layer thickness. The RE-doped layers can be overgrown by undoped KYW overlays in order to obtain buried active structures.

By comparing the quality of the layers grown from two different solvents, we conclude that the $\text{K}_2\text{W}_2\text{O}_7$ solvent offers higher crystalline perfection than the chloride NaCl-KCl-CsCl solvent. The “intrinsic” tungstate flux contains no other ions than required for the KYW crystal growth and is a good solvent for KYW, which is the only stable phase to be crystallized from the solution. In contrary, when using the chloride solvent, the formation of parasitic phases and pronounced 3D island nucleation generate insertion defects, which limit the maximum layer thickness to approx. 10 μm . Nevertheless, the chloride solvent with its melting point of 480°C offers exceptionally low growth temperatures that can reduce the thermal stress during cooling heavily RE-doped thin layers from growth to room temperature.

The original concept of microchannel epitaxy, which has been employed for the first time to obtain channels of an oxide material, opens new horizons in the fabrication of waveguiding channel structures. Applying a simple, patterned metal mask on the surface of KYW substrates, 5-6 mm long KYW:RE ribs with high width/height aspect ratios can be grown from the $\text{K}_2\text{W}_2\text{O}_7$ solvent using MCE. The metal mask can be designed so that the rib surface and side-walls coincide with natural faces of the KYW crystal, which results in atomically smooth facets of the ribs.

End-face polished surface and buried planar layers as well as channels of KYW:RE are suited for optical waveguiding. Propagation losses induced by scattering centers and interface imperfection are 0.1-0.2 dB cm^{-1} , which confirms the high optical quality of the LPE-grown layers. A relatively small refractive index change on the order of 6×10^{-4} in the low-doped KYW:RE layers on undoped KYW substrates corresponds to a waveguide

numerical aperture of 0.05. Higher numerical apertures that assure better light confinement could be obtained by co-doping the KYW:RE layers with another heavy ion. For instance, Gd^{3+} is an optically inactive ion, which easily incorporates into the KYW host and increases the refractive index similarly to the Yb^{3+} ion.

CW laser emission near 1 μm is demonstrated with both, surface and buried planar KYW:Yb waveguides under Ti:sapphire laser pumping. Output powers up to 290 mW are achieved in the fundamental mode and the slope efficiency is above 80%, which is, to the best of our knowledge, the highest value ever reported for a planar waveguide laser. A future step is establishing a monolithic laser cavity by use of butt-coupled laser mirrors and demonstrating laser diode pumping.

The investigation of already grown KYW layers doped with other RE^{3+} ions and their combinations with the Yb^{3+} ion is currently in progress. In particular, Dy^{3+} - Yb^{3+} and Tb^{3+} - Yb^{3+} co-doped KYW layers are studied at the University of Cantabria (Spain) in order to determine the nature of energy transfer processes within the RE^{3+} - Yb^{3+} pairs. This ongoing research could lead to a discovery of new laser transitions in KYW:RE crystals. Tm-doped KYW thin layers having different thicknesses and doping concentrations will be tested as waveguide lasers at Max-Born-Institute for Nonlinear Optics and Ultrafast Spectroscopy (Germany), where very promising laser results have been demonstrated recently with bulk KYW:Tm crystals, a new laser material in the 2- μm region.

Finally, structuring of the grown KYW:RE thin layers ions using several different techniques is currently pursued at the Advanced Photonics Laboratory (EPF Lausanne). The structuring methods include light ion implantation through slits, reactive ion etching through photolithographically deposited masks, and direct laser ablation. Initial results showed that it is possible to obtain efficient light confinement in channel waveguides with dimensions from 8 to 20 μm in width and from 4 to 30 μm in height.

References

- [ata00] P.A. Atanasov, R.I. Tomov, J. Perrière, R.W. Eason, N. Vainos, A. Klini, A. Zherikhin, E. Millon, "Growth of Nd:potassium gadolinium tungstate thin-film waveguides by pulsed laser deposition", *Appl. Phys. Lett.* **76**, 2490 (2000).
- [ata02] P.A. Atanasov, M. Jimenez de Castro, A. Perea, J. Perriere, J. Gonzalo, C.N. Afonso, "Composition and optical properties of thin films prepared by laser ablation of Nd:KGW", *Appl. Surf. Sci.* **186**, 469 (2002).
- [azn04] A. Aznar, R. Solé, M. Aguiló, F. Diaz, U. Griebner, R. Grunwald, and V. Petrov, "Growth, optical characterization and laser operation of epitaxial Yb:KY(WO₄)₂/KY(WO₄)₂ composites with monoclinic structure", *Appl. Phys. Lett.* **85**, 4313 (2004).
- [bag00] S.N. Bagayev, S.M. Vatnik, A.P. Majorov, A.A. Pavlyuk, D.V. Plakushev, "The spectroscopy and lasing of monoclinic Tm:KY(WO₄)₂ crystals", *Quantum Electron.* **30**, 310 (2000).
- [bat02] L.E. Batay, A.N. Kuzmin, A.S. Grabtchikov, V.A. Lisinetskii, V.A. Orlovich, A.A. Demidovich, A.N. Titov, V.V. Badikov, S.G. Sheina, V.L. Panyutin, M. Mond, S. Kück, "Efficient diode-pumped passively Q-switched laser operation around 1.9 μm and self-frequency Raman conversion of Tm-doped KY(WO₄)₂", *Appl. Phys. Lett.* **81**, 2926 (2002).
- [bata02] L.E. Batay, A.A. Demidovich, A.N. Kuzmin, A.N. Titov, M. Mond, S. Kück, "Efficient tunable laser operation of diode-pumped Yb,Tm:KY(WO₄)₂ around 1.9 μm ", *Appl. Phys. B* **75**, 457 (2002).
- [bau58] E. Bauer, *Z. Kristallogr.* **110**, 395 (1958).
- [bau94] E. Bauser, in: *Handbook of crystal growth*, edited by D.T.J. Hurle, Vol**3a**, Elsevier, Amsterdam, 1994.
- [bla72] S.L. Blank and J.W. Nielsen, "The growth of magnetic garnets by liquid phase epitaxy", *J. Cryst. Growth* **17**, 302 (1972).
- [bor05] C.N. Borca, F. Záh, C. Schnider, R.P. Salathé, M. Pollnau, and P. Moretti, "Fabrication of optical planar waveguides in KY(WO₄)₂ by He-ion implantation", *Conference on Lasers and Electro-Optics Europe*, Munich, Germany, 2005, *Conference Digest*, paper CE6-3-FRI.
- [bor68] S.V. Borisov and R.F. Klevtsova, "Crystal structure of KY(WO₄)₂", *Soviet Physics Crystallography* **13**, 420 (1968).

- [bou03] G. Boulon, L. Laversenne, C. Goutaudier, Y. Guyot, M.T. Cohen-Adad, “Radiative and non-radiative energy transfers in Yb³⁺-doped sesquioxide and garnet laser crystals from a combinatorial approach based on gradient concentration fibers”, *J. Lumin.* **102-103**, 417 (2003).
- [bru02] F. Brunner, T. Südmeyer, E. Innerhofer, F. Morier-Genoud, R. Paschotta, V. E. Kisel, V. G. Shcherbitsky, N. V. Kuleshov, J. Gao, K. Contag, A. Giesen, and U. Keller, “240-fs pulses with 22-W average power from a mode-locked thin-disk Yb:KY(WO₄)₂ laser”, *Opt. Lett.* **27**, 1162 (2002).
- [bru97] T.C. Brunold and H.U. Güdel, “Absorption and luminescence spectroscopy of MnO₄²⁻-doped crystals of BaSO₄”, *Inorg. Chem.* **36**, 1946 (1997).
- [bur51] W.K. Burton, N. Cabrera, and F.C. Frank, “The growth of crystal and the equilibrium structure of their surfaces”, *Phil. Trans. A* **243**, 299 (1951).
- [bur53] J.A. Burton, R.C. Prim, and W.P. Slichter, “The distribution of solute in crystals grown from the melt”, *J. Chem Phys.* **21**, 1987 (1953).
- [cab56] N. Cabrera and M.M. Levine, “On the dislocation theory of evaporation of crystals”, *Phil. Mag.* **1**, 450 (1956).
- [car58] A.E. Carlson, in: *Growth and perfection of crystals*, edited by R.H. Doremus, B.W. Roberts, and E. Turnbull, Wiley, New York, 1958.
- [che04] A.A. Chernov, “Notes on interface kinetics 50 years after Burton, Cabrera and Frank”, *J. Cryst. Growth* **264**, 499 (2004).
- [che91] L.V. Cherginets and E.G. Khailova, “Interaction of Ba²⁺, Sr²⁺, Ni²⁺, and Zn²⁺ ions with oxide ions in molten eutectic CsCl-KcL-NaCl melts”, *Russ. J. Inorg. Chem.* **36**, 1798 (1991).
- [cle98] C. Klemenz and H.J. Scheel, “Crystal growth and epitaxy from solutions”, *Mater. Sci. Forum* **276-277**, 175 (1998).
- [CRC00] CRC Handbook of Chemistry and Physics, edited by D.R. Lide, 81st ed., CRC Press, Boca Raton, 2000.
- [del93] L.D. DeLoach, S.A. Payne, L. Chase, L.K. Smith, W.L. Kway, and W.F. Krupke, “Evaluation of absorption and emission properties of Yb³⁺ doped crystals for laser applications”, *IEEE J. Quantum Electron.* **29**, 1179 (1993).
- [dem00] A.A. Demidovich, A.N. Kuzmin, G.I. Ryabtsev, M.B. Danailov, W. Strek, A.N. Titov, “Influence of Yb concentration on Yb:KYW laser properties”, *J. Alloys Comp.* **300-301**, 238 (2000).
- [die63] G.H. Dieke and H.M. Crosswhite, “The spectra of the doubly and triply ionized rare earths”, *Appl. Optics* **2**, 675 (1963).

- [dte04] FP6 European project “Double tungstate crystals: synthesis, characterization and applications”, 1st annual report, 2004. <http://www.dt-crys.net/> (internal).
- [ehr02] D. Ehrentraut and M. Pollnau, “Flux growth of barite-type BaSO₄ from chloridic alkaline metal solvents”, *J. Cryst. Growth* **234**, 533 (2002).
- [ehr03] D. Ehrentraut, “Epitaxial growth and optical characterization of BaSO₄:Mn⁶⁺ layers for novel coherent light sources”, Ph.D. dissertation, Ecole Polytechnique Fédérale de Lausanne, Switzerland, 2003.
- [elw75] D. Elwell and H.J. Scheel, *Crystal growth from high-temperature solutions*, Academic Press, London-New York, 1975.
- [fer99] B. Ferrand, B. Chambaz, and M. Couchaud, “Liquid phase epitaxy: a versatile technique for the development of miniature optical components in single crystal dielectric media”, *Opt. Mater.* **11**, 101 (1999).
- [fer99] B. Ferrand, B. Chambaz, and M. Couchaud, “Liquid phase epitaxy: A versatile technique for the development of miniature optical components in single crystal dielectric media”, *Opt. Mater.* **11**, 101 (1999).
- [fra49] F.C. Frank and J.H. Van der Merwe, “One-dimensional dislocations. 1. Static theory”, *Proc. R. Soc. London A* **198**, 205, (1949).
- [gal98] E. Gallucci, C. Goutaudier, G. Boulon, and M.T. Cohen-Adad, “Growth of KY(WO₄)₂ single crystal: investigation of the WO₃ rich region in the K₂O-Y₂O₃-WO₃ ternary system. 2 – The KY(WO₄)₂ crystallization field”, *Eur. J. Solid State Inorg. Chem.* **35**, 433 (1998).
- [gal00] E. Gallucci, C. Goutaudier, G. Boulon, M.Th. Cohen-Adad, B.F. Mentzen, “Nonstoichiometric KY(WO₄)₂: crystal growth, chemical and physical characterization”, *J. Cryst. Growth* **209**, 895 (2000).
- [galu00] E. Gallucci, C. Goutaudier, M.Th. Cohen-Adad, B.F. Mentzen, T. Hansen, “A neutron diffraction study of non-stoichiometric KYW₂O₈”, *J. Alloys Comp.* **306**, 227 (2000).
- [gal01] C. Goutaudier, E. Gallucci, G. Boulon, and M.T. Cohen-Adad, “Growth of well-characterized KY(WO₄)₂ single crystals using a Bridgman-type technique and based on the K₂O-Y₂O₃-WO₃ ternary system knowledge”, *J. Phase Equilibria* **22**, 208 (2001).
- [ger01] R. Gerhardt, “Channel waveguide lasers in epitaxial garnet films”, Ph.D. dissertation, Universität Osnabrück, Germany, 2001.

- [gri99] U. Griebner and H. Schönagel, “Laser operation with nearly diffraction-limited output from a Yb:YAG multimode channel waveguide“, *Opt. Lett.* **24**, 750 (1999).
- [gue70] R. Guerin and P. Caillet, “Phases of system K_2WO_4 - WO_3 and their reduction by potassium vapor”, *C. R. Acad. Sci., Ser. C* **271**, 815 (1970).
- [han02] X. Han, G. Wang, and T. Tsuboi, “Growth and spectral properties of Er^{3+}/Yb^{3+} -codoped $KY(WO_4)_2$ crystal”, *J. Cryst. Growth* **242**, 412 (2002).
- [han92] D.C. Hanna, A.C. Large, D.P. Shepherd, A.C. Tropper, I. Chartier, B. Ferrand, and D. Pelenc, “A side-pumped Nd:YAG epitaxial waveguide laser”, *Optics Comm.* **91**, 229 (1992).
- [hsi74] J.J. Hsieh, “Thickness and surface morphology of GaAs LPE layers grown by supercooling, step-cooling, equilibrium cooling, and two-phase solution techniques”, *J. Cryst. Growth* **27**, 49 (1974).
- [hun91] R.G. Hunsperger, *Integrated Optics: Theory and Technology*, in: Springer Series in Optical Sciences, Vol. **33**, 3rd ed., edited by T. Tamir, Springer-Verlag, Berlin, 1991.
- [ily62] I. Il'yasov and A.G. Bergman, “Melting points in the Cs, K, Na//Cl ternary system”, *Zh. Neorg. Khim.* **7**, 695 (1962).
- [ivl88] L.I. Ivleva, D.T. Kiselev, Y.S. Kuzminov, N.M. Polozkov, "Growth and study of barium metaborate single crystals", *Inorg. Mater.* **24**, 982 (1988).
- [jan82] G.J. Janz and N.P. Bansal, “Diffusion coefficients in molten salts”, *J. Phys. Chem. Ref. Data* **11**, 595 (1982).
- [jas83] L. Jastzebski, J.F. Corboy, J.T. McGinn, and R. Pogliar, Jr., “Growth process of silicon over SiO_2 by CVD: epitaxial lateral overgrowth technique”, *J. Electrochem. Soc.* **130**, 1571 (1983).
- [jel02] M. Jelinek, J. Lancok, M. Pavelka, P.A. Atanasov, A. Macjova, F. Flory, C. Garapon, “Optical and waveguiding properties of Nd:KGW films grown by pulsed laser deposition”, *Appl. Phys. A* **74**, 481 (2002).
- [jel98] M. Jelinek, J. Lancok, J. Sonsky, J. Oswald, M. Simeckova, L. Jastrabik, V. Studnicka, “Planar waveguide lasers and structures created by laser ablation – an overview”, *Czech. J. Physics* **48**, 577 (1998).
- [jm04] Alfa Aesar – A Johnson Matthey Company, *Research Chemicals and Metals*, Product catalogue, 2003-2004. <http://www.alfa-chemcat.com>.

- [jon95] J.K. Jones, J.P. de Sandro, M. Hempstead, D.P. Shepherd, A.C. Large, A.C. Tropper, and J.S. Wilkinson, "Channel waveguide laser at 1 μm in Yb-indiffused LiNbO_3 ", *Opt. Lett.* **20**, 1477 (1995).
- [kam71] A.A. Kaminskii, P.V. Klevtsov, and A.A. Pavlyuk, "Stimulated emission from $\text{KY}(\text{WO}_4)_2\text{-Nd}^{3+}$ crystal laser", *Phys. Stat. Sol. A* **5**, K79 (1971).
- [kam72] A.A. Kaminskii, P.V. Klevtsov, L. Li, and A.A. Pavlyuk, "Laser ${}^4\text{F}_{3/2}\rightarrow{}^4\text{I}_{9/2}$ and ${}^4\text{F}_{3/2}\rightarrow{}^4\text{I}_{13/2}$ transitions in $\text{KY}(\text{WO}_4)_2\text{:Nd}^{3+}$ ", *IEEE J. Quantum Electron.* **8**, 457 (1972).
- [kam77] A.A. Kaminskii, A.A. Pavlyuk, P.V. Klevtsov, I.F. Balashov, V.A. Berenberg, S.E. Sarkisov, V.A. Fedorov, M.A. Petrov, and V.V. Lyubchenko, "Stimulated radiation of monoclinic crystals of $\text{KY}(\text{WO}_4)_2$ and $\text{KGd}(\text{WO}_4)_2$ with Ln^{3+} ions", *Izv. Akad. Nauk SSSR, Neorgan. Mater.* **13**, 582 (1977).
- [kam78] A.A. Kaminskii, A.A. Pavlyuk, I.F. Balashov, V.A. Berenberg, V.V. Lyubchenko, V.A. Fedorov, T.I. Butaeva, and L.I. Bobovich, "Stimulated emission by $\text{KY}(\text{WO}_4)_2\text{-Er}^{3+}$ crystals", *Izv. Akad. Nauk SSSR, Neorgan. Mater.* **14**, 2256 (1978).
- [kam79] A.A. Kaminskii, A.A. Pavlyuk, Ch. Ngok, L.I. Bobovich, V.A. Fedorov, and V.V. Lyubchenko, "3 μ stimulated emission by Ho^{3+} ions in $\text{KY}(\text{WO}_4)_2$ crystals at 300K", *Dokl. Akad. Nauk SSSR* **245**, 575 (1979).
- [kam83] A.A. Kaminskii, A.A. Pavlyuk, A.I. Polyakova, and V.V. Lyubchenko, "A new lasing channel in a self-activated erbium crystal $\text{KEr}(\text{WO}_4)_2$ ", *Dokl. Akad. Nauk SSSR* **268**, 856 (1983).
- [kam97] A.A. Kaminskii, L. Li, A.V. Butashin, V.S. Mironov, A.A. Pavlyuk, S.N. Bagayev, and K. Ueda, "New stimulated emission channels of Pr^{3+} and Tm^{3+} ions in monoclinic $\text{KY}(\text{WO}_4)_2$ type crystals with ordered structure ($\text{R}=\text{Y}$ and Gd)", *Jpn. J. Appl. Phys.* **36**, LI07 (1997).
- [kam00] A. Kaminskii, U. Hömmerich, D. Temple, J.T. Seo, K. Ueda, S. Bagayev, and A. Pavlyuk, "Visible laser action of Dy^{3+} ions in monoclinic $\text{KY}(\text{WO}_4)_2$ and $\text{KGd}(\text{WO}_4)_2$ crystals under Xe-flashlamp pumping", *Jpn. J. Appl. Phys.* **39**, L208 (2000).
- [kam01] A.A. Kaminskii, A.F. Konstantinova, V.P. Orekhova, A.V. Butashin, R.F. Klevtsova, and A.A. Pavlyuk, "Optical and nonlinear laser properties of the $\chi^{(3)}$ -active monoclinic $\alpha\text{-KY}(\text{WO}_4)_2$ crystals", *Crystallography Reports* **46**, 665 (2001).

- [kam02] A.A. Kaminskii, J.B. Gruber, S.N. Bagaev, K. Ueda, U. Hommerich, J.T. Seo, D. Temple, B. Zandi, A.A. Kornienko, E.B. Dunina, A.A. Pavlyuk, R.F. Klevtsova, and F.A. Kuznetsov, "Optical spectroscopy and visible stimulated emission of Dy^{3+} ions in monoclinic $\alpha\text{-KY}(\text{WO}_4)_2$ and $\alpha\text{-KGd}(\text{WO}_4)_2$ crystals", *Phys. Rev. B* **65**, 125108 (2002).
- [kis04] V.E. Kisel, A.E. Troshin, V.G. Shcherbitsky, and N.V. Kuleshov, "Spectroscopic and laser properties of $\text{Yb}^{3+}:\text{KY}(\text{WO}_4)_2$ with high doping level", EPS-QEOD Europhoton Conference on Solid-State and Fiber Coherent Light Sources, Lausanne, Switzerland, 2004, Europhysics Conference Abstracts, Vol. 28C, paper TuC18.
- [kle68] P.V. Klevtsov, L.P. Kozeeva, and R.F. Klevtsova, "Crystallographic study of potassium-yttrium tungstate and molybdate", *Izv. Akad. Nauk SSSR, Neorgan. Mater.* **4**, 1147 (1968).
- [kle69] P.V. Klevtsov and L.P. Kozeeva, "Synthesis and X-ray and thermal studies of potassium rare-earth tungstates, $\text{KLn}(\text{WO}_4)_2$, Ln=rare-earth element", *Dokl. Akad. Nauk SSSR, Crystallography* **185**, 571 (1969).
- [kle96] C. Klemenz, H.J. Scheel, "Flat $\text{YBa}_2\text{Cu}_3\text{O}_{7-x}$ layers for planar tunnel-device technology", *Physica C* **265**, 126 (1996).
- [klo03] P. Klopp, V. Petrov, and U. Griebner, "Potassium Ytterbium Tungstate Provide the Smallest Laser Quantum Defect", *Jpn. J. Appl. Phys.* **42**, L246 (2003).
- [klo03] P. Klopp, V. Petrov, U. Griebner, V. Nesterenko, V. Nikolov, M. Marinov, M.A. Barsukova, M. Galan, "Continuous-wave lasing of a stoichiometric Yb laser material: $\text{KYb}(\text{WO}_4)_2$ ", *Opt. Lett.* **28**, 322 (2003).
- [kog90] H. Kogelnik, *Theory of optical waveguides*, in: *Guided-wave optoelectronics*, edited by T. Tamir, Springer Series in Electronics and Photonics, Vol. **26**, 2nd ed., Springer-Verlag, Berlin-Heidelberg, 1990.
- [kry02] I.M. Krygin, A.D. Prokhorov, V.P. D'yakonov, M.T. Borowiec, and H. Szymczak, "Spin-spin interaction of Dy^{3+} ions in $\text{KY}(\text{WO}_4)_2$ ", *Physics Solid State* **44**, 1513 (2002).
- [kul97] N.V. Kuleshov, A.A. Lagatsky, V.G. Shcherbitsky, V.P. Mikhailov, E. Heumann, T. Jensen, A. Dening, and G. Huber, "CW laser performance of Yb and Er, Yb doped tungstates", *Appl. Phys. B* **64**, 409 (1997).
- [kule97] N.V. Kuleshov, A.A. Lagatsky, A.V. Podlipensky, V.P. Mikhailov, and G. Huber, "Pulsed laser operation of Yb-doped $\text{KY}(\text{WO}_4)_2$ and $\text{KGd}(\text{WO}_4)_2$ ", *Opt. Lett.* **22**, 1317 (1997).

- [lac91] P. Lacovara, H.K. Choi, C.A. Wang, R.L. Agarwal, and T.Y. Fan, "Room-temperature diode-pumped Yb:YAG laser", *Opt. Lett.* **16**, 1089 (1991).
- [lb77] *Numerical Data and Functional Relationships in Science and Technology*, edited by K.H. Hellwege and A.M. Hellwege, Landolt-Börnstein series Vol. **III/7**, Part f, Springer-Verlag, Berlin, 1977.
- [mac98] L. Macalik, J. Hanuza, B. Macalik, W. Ryba-Romanovski, S. Golab, A. Pietraszko, "Optical spectroscopy of Dy³⁺ ions doped in KY(WO₄)₂ crystals", *J. Lumin.* **79**, 9 (1998).
- [mat05] X. Mateos, R. Solé, Jna. Gavaldà, M. Aguiló, F. Díaz, and J. Massons, "Ultraviolet and visible emissions of Er³⁺ in KY(WO₄)₂ single crystals co-doped with Yb³⁺ ions", *J. Lumin.* **115**, 131 (2005).
- [mat72] J.W. Matthews and E. Klokholm, "Fracture of brittle epitaxial films under the influence of misfit stress", *Mat. Res. Bull.* **7**, 213 (1972).
- [met97] G. Métrat, N. Muhlstein, A. Brenier, G. Boulon, "Growth by the induced nucleated floating crystal (INFC) method and spectroscopic properties of KY_{1-x}Nd_x(WO₄)₂ laser materials", *Opt. Mater.* **8**, 75 (1997).
- [met99] G. Métrat, M. Boudeulle, N. Muhlstein, A. Brenier, G. Boulon, "Nucleation, morphology and spectroscopic properties of Yb-doped KY(WO₄)₂ crystals grown by the top nucleated floating crystal method", *J. Cryst. Growth* **197**, 883 (1999).
- [mil69] S.E. Miller, "Integrated optics - an introduction", *Beel System Techn. J.* **48**, 2059 (1969)
- [mob97] P.A. Möbert, E. Heumann, G. Huber, B.H.T. Chai, "Green Er³⁺:YLiF₄ upconversion laser at 551nm with Yb³⁺ codoping: a novel pumping scheme", *Opt. Lett.* **22**, 1412 (1997).
- [nas71] K. Nassau, *The Chemistry of Laser Crystals*, in: *Applied Solid State Science: Advances in Materials and Device Research*, edited by R. Wolfe, Vol. **2**, Academic Press, New York, 1971.
- [nel63] H. Nelson, "Epitaxial growth from the liquid state and its application to the fabrication of tunnel and laser diodes", *RCA Review*, **24**, 603 (1963).
- [nish96] T. Nishinaga and H.J. Scheel, in: *Advances in Superconductivity VIII*, edited by H. Hayakawa and Y. Enomoto, Springer-Verlag, Tokyo, 1996.
- [pav97] A.A. Pavlyuk, L.I. Yudanova, and O.G. Potapova, "KGd(WO₄)₂-KNd(WO₄)₂ and RbGd(WO₄)₂-RbNd(WO₄)₂ phase diagrams and growth of Nd-doped KGd(WO₄)₂ and RbGd(WO₄)₂ single crystals", *Inorg. Mater.* **33**, 64 (1997).

- [pel95] D. Pelenc, B. Chambaz, I. Chartier, B. Ferrand, C. Wyon, D.P. Shepherd, D.C. Hanna, A.C. Large, A.C. Tropper, "High slope efficiency and low laser threshold in a diode-pumped epitaxially grown Yb:YAG waveguide laser", *Optics Comm.* **115**, 491 (1995).
- [pet05] K. Petermann, D. Fagundes-Peters, J. Johannsen, M. Mond, V. Peters, J.J. Romero, S. Kutovoi, J. Speiser, A. Giesen, "Highly Yb-doped oxides for thin disc lasers", *J. Cryst. Growth* **275**, 135 (2005).
- [pol00] M. Pollnau, D.R. Gamelin, S.R. Lüthi, H.U. Güdel, M.P. Hehlen, "Power dependence of upconversion luminescence in lanthanide and transition-metal-ion systems", *Physical Review B* **61**, 3337 (2000).
- [puj99] M.C. Pujol, R. Solé, V. Nikolov, Jna. Gavalda, J. Massons, C. Zaldo, M. Aguiló, F. Díaz, "Linear thermal expansion tensor in $KRE(WO_4)_2$ (RE=Gd, Y, Er Yb) monoclinic crystals", *J. Mater. Res.* **14**, 3739 (1999).
- [pujo99] M.C. Pujol, R. Solé, J. Gavalda, J. Massons, M. Aguiló, F. Díaz, V. Nikolov, C. Zaldo, "Growth and ultraviolet optical properties of $KGd_{1-x}RE_x(WO_4)_2$ single crystals", *J. Mater. Res.* **14**, 3739 (1999).
- [puj01] M.C. Pujol, X. Mateos, R. Solé, J. Massons, J. Gavalda, X. Solans, F. Díaz, and M. Aguiló, "Structure, crystal growth and physical anisotropy of $KYb(WO_4)_2$, a new layer matrix", *J. Appl. Cryst.* **35**, 108 (2002).
- [puj02] M.C. Pujol, M.A. Bursukova, F. Güell, X. Mateos, R. Solé, J. Gavalda, M. Aguiló, J. Massons, F. Díaz, P. Klopp, U. Griebner, and V. Petrov, "Laser operation of the new stoichiometric crystal $KYb(WO_4)_2$ ", *Appl. Phys. B* **74**, 185 (2002).
- [pujo02] M.C. Pujol, M.A. Bursukova, F. Güell, X. Mateos, R. Sole, J. Gavalda, M. Aguiló, J. Massons, F. Díaz, P. Klopp, U. Griebner, and V. Petrov, "Growth, optical characterization, and laser operation of a stoichiometric crystal $KYb(WO_4)_2$ ", *Phys. Rev. B* **65**, 165121 (2002).
- [rob78] J.M. Robertson, "Liquid phase epitaxy of garnets", *J. Cryst. Growth* **45**, 233 (1978).
- [rom03] Y.E. Romanyuk, D. Ehrentraut, A. Aznar, R. Solé, M. Aguiló, P. Gerner, H.U. Güdel, M. Pollnau, "Liquid-phase epitaxy and optical investigation of $KYb(WO_4)_2$ thin layers", *International Spring Workshop on Spectroscopy, Structure and Synthesis of Rare Earths Systems*, Ladek-Zdroj, Poland, 2003, Abstracts, paper O22.

- [roma03] Y.E. Romanyuk, D. Ehretraut, M. Pollnau, S. Kück, "Liquid phase epitaxy of Mn⁶⁺-doped tungstates and molybdates", Swiss Physical Society Meeting, Basel, Switzerland, 2003, Bulletin SPG/SSP, Vol. **20**, paper 216, p. 53.
- [rom04] Y.E. Romanyuk, D. Ehretraut, M. Pollnau, S. García-Revilla, R. Valiente, "Low-temperature flux growth of sulfates, molybdates, and tungstates of Ca, Sr, and Ba and investigation of doping with Mn⁶⁺", Appl. Phys. A **79**, 613-618 (2004).
- [roma04] Y.E. Romanyuk, D. Ehretraut, M. Pollnau, S. Kück, "Flux growth and liquid phase epitaxy of Mn⁶⁺-doped tungstates and molybdates", Conference on Lasers and Electro-Optics Europe, Munich, Germany, 2003, Europhysics Conference Abstracts Vol. **27E**, paper CG2-1-WED.
- [ros79] F.E. Rosenberger, *Fundamentals of crystal growth*, Vol.1, Springer, Berlin, 1979.
- [sal01] G.M. Salley, R. Valiente, and H.U. Güdel, "Luminescence upconversion mechanisms in Yb³⁺-Tb³⁺ systems", J. Lumin. **94-95**, 305 (2001).
- [sal91] E.A. Saleh and M.C. Teich, *Fundamentals of photonics*, Wiley series in pure and applied optics, edited by J.W. Goodman, John Wiley & Sons, Inc., New York, 1991.
- [sch74] H.J. Scheel, "Crystallization of sulfides from alkali polysulfide fluxes", J. Cryst. Growth **24-25**, 699 (1974).
- [sha76] R.D. Shannon, "Revised effective ionic radii and systematic studies of interatomic distances in halides and chalcogenides", Acta Cryst. A **32**, 751 (1976).
- [shi96] M. Shimokozono, N. Sugimoto, A. Tate, Y. Katoh, M. Tanno, S. Fukuda, and T. Ryuoh, "Room-temperature operation of an Yb-doped Gd₃Ga₅O₁₂ buried channel waveguide laser at 1.025 μm wavelength", Appl. Phys. Lett. **68**, 2177 (1996).
- [sol96] R. Solé, V. Nikolov, X. Ruiz, J. Gavaldà, X. Solans, M. Aguiló, and F. Diaz, "Growth of beta-KGd_{1-x}Nd_x(WO₄)₂ single crystals in K₂W₂O₇ solvents", J. Cryst. Growth **169**, 600 (1996).
- [str38] J.N. Stranski and L. Krastanov, Ber. Akad. Wiss. Wien **146**, 797 (1938).
- [sve98] O. Svelto, *Principles of lasers*, edited by D.C. Hanna, 4th ed., Plenum Press, New York, 1998.
- [tie72] P.K. Tien, R.J. Martin, S.L. Blank, S.H. Wemple, L.J. Varnerin, "Optical waveguides in single-crystal garnet films", Appl. Phys. Lett. **21**, 207 (1972).
- [tu92] C. Tu, Y. Huang, Z. Luo, and G. Chen, "Crystal growth of KY(WO₄)₂:Er³⁺, Nd³⁺", J. Cryst. Growth **135**, 636 (1994).
- [uji89] Y. Ujiie and T. Nishinaga, "Epitaxial lateral overgrowth of GaAs on a Si substrate", Jpn. J. Appl. Phys. **28**, L337 (1989).

- [uit61] L.G. Van Uitert and R.R. Soden, "Enhancement of Eu^{3+} emission by Tb^{3+} ", J. Chem. Phys. **36**, 1289 (1961).
- [vol26] M. Volmer and A. Weber, Z. Phys. Chem. **119**, 277 (1926).
- [wan90] G. Wang and Z. Luo, " $\text{Nd}^{3+}:\text{KY}(\text{WO}_4)_2$ crystal growth and X-ray diffraction", J. Cryst. Growth **102**, 765 (1990).
- [wan92] G. Wang and Z. Luo, "Crystal growth of $\text{KY}(\text{WO}_4)_2:\text{Er}^{3+}$, Yb^{3+} ", J. Cryst. Growth **116**, 505 (1992).
- [zuc74] S. Zuca and R. Borcan, "Viscosity of binary molten alkali chloride systems", Rev. Roumaine Chim. **19**, 553 (1974).

List of Publications and Conference Contributions

(September 2002 – November 2005)

Parts of this dissertation have previously been published in journal articles:

1. Y.E. Romanyuk, C.N. Borca, M. Pollnau, S. Rivier, V. Petrov, U. Griebner, "Yb-doped KY(WO₄)₂ planar waveguide laser", *Optics Lett.* **31** (1), in press (2006).
2. Y.E. Romanyuk, I. Utke, D. Ehrentraut, V. Apostolopoulos, M. Pollnau, S. García-Revilla, R. Valiente, "Low-temperature liquid-phase epitaxy and optical waveguiding of rare-earth-ion doped KY(WO₄)₂ thin layers", *J. Cryst. Growth* **269** (2-4), 377-384 (2004).
3. D. Ehrentraut, Y.E. Romanyuk, M. Pollnau, "Flux Growth and Liquid-Phase Epitaxy of Mn⁶⁺-doped Barium Sulfate", *J. Ceramic Processing Res.* **5** (3), 256-260 (2004).
4. Y.E. Romanyuk, D. Ehrentraut, M. Pollnau, S. García-Revilla, R. Valiente, "Low-temperature flux growth of sulfates, molybdates, and tungstates of Ca, Sr, and Ba and investigation of doping with Mn⁶⁺", *Appl. Phys. A* **79**, 613-618 (2004).

Other journal articles:

5. O.V. Parasyuk, L.V. Piskach, Y.E. Romanyuk, I.D. Olekseyuk, V.I. Zaremba, V.I. Pekhnyo, "Phase relations in the quasi-binary Cu₂GeS₃–ZnS and quasi-ternary Cu₂S–Zn(Cd)S–GeS₂ systems and crystal structure of Cu₂ZnGeS₄", *J. Alloys Comp.* **397** (1-2), 85-94 (2005).
6. I.D. Olekseyuk, O.V. Parasyuk, O.M. Yurchenko, V.Z. Pankevych, V.I. Zaremba, R. Valiente, Y.E. Romanyuk, "Single crystal growth and properties of AgCd₂GaS₄", *J. Cryst. Growth* **279**, 140-145 (2005).
7. O.V. Parasyuk, Y.E. Romanyuk, I.D. Olekseyuk, "Single-crystal growth of Cu₂CdGeS₄", *J. Cryst. Growth* **275**, e169-e172 (2005).
8. L.D. Gulay, O.V. Parasyuk, Ya.E. Romanyuk, I.D. Olekseyuk, "Crystal structure of the Cu_{5.976}Hg_{0.972}SiSe₆ compound", *J. Alloys Comp.* **367** (1-2), 121-125 (2004).
9. G.E. Davidiyuk, O.V. Parasyuk, S.A. Semenyuk, Ya.E. Romanyuk, "Electrical and optical properties of Cu₂CdGeS₄ single crystals", *Inorg. Mater.* **39** (9), 919-923 (2003).

10. O.V. Parasyuk, L.D. Gulay, Ya.E. Romanyuk, I.D. Olekseyuk, L.V. Piskach, "The $\text{Ag}_2\text{Se-HgSe-GeSe}_2$ system and crystal structures of the compounds", *J. Alloys Comp.* **351** (1-2), 135-144 (2003).
11. O.V. Parasyuk, L.D. Gulay, Y.E. Romanyuk, I.D. Olekseyuk, "The $\text{Ag}_2\text{Se-HgSe-SiSe}_2$ system in the 0–60 mol.% SiSe_2 region", *J. Alloys Comp.* **348** (1-2), 157-166 (2003).
12. Y.E. Romanyuk, O.V. Parasyuk, "Phase equilibria in the quasi-ternary $\text{Cu}_2\text{Se-ZnSe-GeSe}_2$ system", *J. Alloys Comp.* **348** (1-2), 195-202 (2002).

Conference contributions:

1. Y.E. Romanyuk, C.N. Borca, M. Pollnau, M. Pollnau, "Thin layers of $\text{KY}(\text{WO}_4)_2:\text{Yb}^{3+}$ for waveguide lasers", 16th American Conference on Crystal Growth, Big Sky Resort, Montana, 2005, Abstract Book, p.51.
2. C.N. Borca and Y.E. Romanyuk, "Methods of fabricating surface undoped and Yb-doped $\text{KY}(\text{WO}_4)_2$ planar waveguides", Photonic Integrated Components & Applications Workshop, Barcelona, Spain, 2005, Conference Proceedings, p. 315, paper Tu.B2.6, Invited Paper.
3. Y.E. Romanyuk, C.N. Borca, M. Pollnau, U. Griebner, S. Rivier, and V. Petrov, "High slope efficiency in epitaxially grown $\text{KY}(\text{WO}_4)_2:\text{Yb}^{3+}$ waveguide laser", International Laser Physics Workshop, Kyoto, Japan, 2005, Book of Abstracts, p. 243, Invited Paper.
4. Y.E. Romanyuk, C.N. Borca, M. Pollnau, S. Rivier, V. Petrov, U. Griebner, "Surface and buried planar waveguide lasers based on $\text{KY}(\text{WO}_4)_2:\text{Yb}^{3+}$ ", Conference on Lasers and Electro-Optics Europe, Munich, Germany, 2005, Conference Digest, paper CJ6-3-THU.
5. Y.E. Romanyuk, C.N. Borca, M. Pollnau, U. Griebner, S. Rivier, and V. Petrov, " $\text{KY}(\text{WO}_4)_2:\text{Yb}^{3+}$ planar waveguide laser", Conference on Lasers and Electro-Optics, Baltimore, Maryland, 2005, Technical Digest (Optical Society of America, Washington, DC 2005), paper CThI5.
6. Y.E. Romanyuk, C.N. Borca, I. Utke, L.L. Kuandykov, M. Pollnau, " $\text{KY}(\text{WO}_4)_2:\text{Yb}^{3+}$ buried planar waveguides grown by liquid-phase epitaxy ", Gemeinsame Jahrestagung der Deutschen Gesellschaft für Kristallwachstum und Kristallzüchtung und der Deutschen Gesellschaft für Kristallographie, Köln, 2005, Referate, p. 194.

7. O.V. Parasyuk, O.M. Yurchenko, V.Z. Pankevych, Y.E. Romanyuk, R. Valiente, "Optical properties of $\text{AgCd}_2\text{GaS}_4$ ", EPS-QEOD Europhoton Conference on Solid-State and Fiber Coherent Light Sources, Lausanne, Switzerland, 2004, Europhysics Conference Abstracts, Vol. 28C, paper TuC15.
8. S. García-Revilla, R. Valiente, Y.E. Romanyuk, M. Pollnau, "Optical spectroscopy of rare-earth ions doped $\text{KY}(\text{WO}_4)_2$ thin films", EPS-QEOD Europhoton Conference on Solid-State and Fiber Coherent Light Sources, Lausanne, Switzerland, 2004, Europhysics Conference Abstracts, Vol. 28C, paper TuC16.
9. Y.E. Romanyuk, V. Apostolopoulos, I. Utke, M. Pollnau, "Rare-earth-ion doped $\text{KY}(\text{WO}_4)_2$ optical waveguides grown by liquid-phase epitaxy", EPS-QEOD Europhoton Conference on Solid-State and Fiber Coherent Light Sources, Lausanne, Switzerland, 2004, Europhysics Conference Abstracts, Vol. 28C, paper ThD6.
10. O.V. Parasyuk, Y.E. Romanyuk, I.D. Oleskeyuk, "Single crystal growth of $\text{Cu}_2\text{CdGeS}_4$ ", 14th International Conference on Crystal Growth, Grenoble, France, 2004, Abstracts, p. 73, paper 0544.
11. Y.E. Romanyuk, I. Utke, D. Ehrentraut, M. Pollnau, S. García-Revilla, R. Valiente, N.V. Kuleshov, "Low-temperature liquid-phase epitaxy of rare-earth-ion doped $\text{KY}(\text{WO}_4)_2$ thin layers", 14th International Conference on Crystal Growth, Grenoble, France, 2004, Abstracts, p. 404, paper 0981.
12. Y.E. Romanyuk, I. Utke, M. Pollnau, "Rare-earth-ion doped $\text{KY}(\text{WO}_4)_2$ thin layer growth by low-temperature liquid-phase epitaxy", 12th International Summer School on Crystal Growth, Berlin, Germany, 2004, Program and Abstracts, p. 113, paper P5-13.
13. Y.E. Romanyuk, I. Utke, D. Ehrentraut, S. García-Revilla, R. Valiente, M. Pollnau, "Low-temperature liquid-phase epitaxy of rare-earth-ion doped $\text{KY}(\text{WO}_4)_2$ thin films", Gemeinsame Jahrestagung der Deutschen Gesellschaft für Kristallwachstum und Kristallzüchtung und der Deutschen Gesellschaft für Kristallographie, Jena, 2004, Referate, p. 194.
14. Y.E. Romanyuk, S. García-Revilla, R. Valiente, I. Utke, M. Pollnau, "Liquid-phase epitaxy of rare-earth-ion doped $\text{KY}(\text{WO}_4)_2$ thin films ", Conference of the Swiss Physical Society, Neuchâtel, Switzerland, 2004, in Bulletin SPG/SSP, Vol. 21, 2004, paper 205, p. 39.

15. D. Ehretraut, Y.E. Romanyuk, M. Pollnau, "Flux growth and liquid phase epitaxy of undoped and Mn⁶⁺-doped sulfates, tungstates, and molybdates", Advanced Crystal Growth Conference, Seoul, Korea, 2003, Abstract Book, A22 (invited).
16. Aznar, D. Ehretraut, Y.E. Romanyuk, R. Solé, M. Aguiló, P. Gerner, H.U. Güdel, M. Pollnau, "Liquid phase epitaxy and spectroscopic investigation of optically active KYb(WO₄)₂ thin layers", International Conference on f-Elements, Geneva, Switzerland, 2003, Final Programme and Abstract Book, p. 111, paper PC-42.
17. Y.E. Romanyuk, D. Ehretraut, S. Kück, M. Pollnau, "Flux growth and liquid phase epitaxy of undoped and Mn⁶⁺-doped sulfates, tungstates, and molybdates", Fifteenth American Conference on Crystal Growth and Epitaxy, Keystone, Colorado, 2003, Abstract Book, pp. 82-83.
18. Y.E. Romanyuk, D. Ehretraut, M. Pollnau, S. Kück, "Flux growth and liquid phase epitaxy of Mn⁶⁺-doped tungstates and molybdates", Conference on Lasers and Electro-Optics Europe, Munich, Germany, 2003, Europhysics Conference Abstracts Vol. 27E, paper CG2-1-WED.
19. Y.E. Romanyuk, D. Ehretraut, A. Aznar, R. Solé, M. Aguiló, P. Gerner, H.U. Güdel, M. Pollnau, "Liquid-phase epitaxy and optical investigation of KYb(WO₄)₂ thin layers", International Spring Workshop on Spectroscopy, Structure and Synthesis of Rare Earths Systems, Ladek-Zdroj, Poland, 2003, Abstracts, paper O22.
20. Y.E. Romanyuk, D. Ehretraut, M. Pollnau, S. Kück, "Liquid phase epitaxy of Mn⁶⁺-doped tungstates and molybdates", Swiss Physical Society Meeting, Basel, Switzerland, 2003, Bulletin SPG/SSP, Vol. 20, paper 216, p. 53.

Acknowledgements

This thesis work could not be possible without help and support of many people. I would like to express my sincere gratitude to

Prof. René-Paul Salathé, my thesis director and head of the Institute of Imaging and Applied Optics for offering me the position of a doctoral candidate and directing my thesis work with interest and motivating spirit,

Prof. Markus Pollnau, my direct thesis supervisor, for his confidence when having chosen me to join his research group, for helping me to make my first steps into the research community; for encouraging me to generate new ideas, publish in prominent scientific journals, and visit beautiful places during international conferences,

Members of the Examination Committee, Prof. Radivoje Popovic (EPF Lausanne), Prof. Benoît Deveaud-Plédran (EPF Lausanne), and Dr. Daniel Rytz (FEE GmbH, Idar-Oberstein) for their kind consent to evaluate and examine my thesis work,

Members of the “Comité de Parrainage”, Prof. Jürg Balmer (Universität Bern) and MER Dr. Patrik Hoffmann (EPF Lausanne) for accepting my thesis plan. I am also grateful to Patrik for his stimulating questions and friendly spirit of a real chemist,

Dr. Dirk Ehrentraut (presently at Tohoku University, Japan), my “elder brother”, whose passion to crystal growth inspired me; who taught and helped me during the first years of my thesis work. Dirk showed me the high-quality “German” standard how to maintain properly a scientific lab. I also thank Dirk for numerous celebrations and mountain trips that we shared together,

Dr. Camelia Borca, current leader of our research group (EPF Lausanne), for great team spirit, helpful discussions, useful thesis corrections, and countless number of other things. I appreciate her friendship and willingness to help me with final optical measurements even if they took several weeks in a dark lab,

Dr. Uwe Griebner, Dr. Valentin Petrov, and Simon Rivier (Max-Born-Institute, Berlin) for the great collaboration and outstanding experimental work on demonstrating the first waveguide laser based on a double tungstate material,

Dr. Ivo Utke (EMPA Thun), for his guidance and stimulated ideas, thesis revision and preparation of patterned substrates. I will always remember warm and joyful evenings with Ivo’s family,

Sara García Revilla and Prof. Rafael Valiente (University of Cantabria, Spain) for our friendly collaboration and one month of unbelievable holidays in sunny Santander,

Dr. Laetitia Laversenne (presently at University of Lion), for the help with waveguide characterization, first lessons of French, and her nice “sourire français”. Dr. Vasilis Apostolopoulos for his rapid assistance to demonstrate the first KYW:RE waveguide,

Dr. Florent Gardillou (EPF Lausanne) for competent translation of the thesis abstract into French and Dr. James Derose (EPF Lausanne) for useful English corrections,

Dr. Nikolay Kuleshov (International Laser Center, Belorussia) for providing high-quality KYW substrates,

Dr. Lev Kuandykov (Ioffe Physico-Technical Institute, Russia) for the colorful simulations of substrate rotation,

Dr. Kurt Schenk (EPF Lausanne) for valuable XRD measurements, Dr. Raymond Houriet (EPF Lausanne) for XRF measurements, Alain Volentik (UNI Lausanne) for EPMA measurements, Dr. Daniel Ariosa (EPF Lausanne) for XRD measurements,

Claude Amendola and Ronald Gianotti, the top class technical staff, for their help in constructing experimental set-up and polishing holders. Alejandro Salamanca for his permanent readiness to help with computer problems,

Manuelle Borruat and Yvette Bernhard, our secretaries, for their patience and high professionalism in handling administrative work,

Dragan Ćorić, Gérard Harbach, Marcel Zeller, Aurelian Crunteanu, Roman Fedoseev, Laura Barbieri, Tristan Bret, Alexandre Perentes, Yann Tissot, Rodrigue Chatton, Daniele Costantini, and Florian “Master” Dürr for numerous services, their friendship, and great working mood,

All my friends who I had a pleasure to meet in Lausanne, Sasha & Galya, Andrej & Oksana, Igor, Ilya & Lena, Sasha & Ulya, Slavik Filinchuk, Slavik Tokajchuk, Oksana Banakh, Galya & Roman, Zlata & Sergij, Pasha, Lyosha, Oleg & Doris, Lyana & Jean-Paul for these three incredible years that we shared together,

Special thanks to Nadezhda Antonovna Karpushko, Sacha & Daisy, and Laurent for their sincere support and warm evenings of excellent classical music,

Dr. Oleg Parasyuk and Dr. Lyudmyla Piskach (Volyn State University, Ukraine), my diploma work supervisors, for giving me a chance to become real researcher,

Andriy, Dmytro, Taras, and Vadym, my faithful friends in Ukraine, who were ready to help even if they were 2.000 km away,

My girlfriend Svitlana for her love and patience,

My big family, my dear parents, and my sister Oksana, who always believed in me.

Curriculum Vitae

Yaroslav ROMANYUK

Data and place of birth January 21, 1980, Ivano-Frankivs'k, Ukraine
Nationality Ukrainian
Professional address Institute of Imaging and Applied Optics
 Ecole Polytechnique Fédérale de Lausanne
 IOA / STI / EPFL BM 4.107
 CH-1015 Lausanne, Switzerland
 yaroslav.romanyuk@epfl.ch
Private address Gordijuk Str. 33A / 28,
 43026 Lutsk, Ukraine

WORK EXPERIENCE

Since August 2002 **Research Assistant**, Institute of Imaging and Applied Optics, EPFL
1999-2002 **Laboratory assistant**, Volyn State University, Lutsk, Ukraine

EDUCATION

Since August 2002 **Ph.D. Candidate**, EPFL
2002 **MSc Degree** in Chemistry, Volyn State University, Lutsk, Ukraine
2001 **BSc Degree** in Chemistry, Volyn State University, Lutsk, Ukraine

HONORS AND AWARDS

2001 “The best young researcher” award, Volyn State University
1998 Student grant from the International Science and Educational Program
1994–2001 Awards in all-Ukrainian and regional competitions on chemistry and mathematics for schoolboys and students

LANGUAGES

Ukrainian: Mother tongue
Russian: Fluent
English: Fluent
French: Good, since 3 years in the French-speaking part of Switzerland
German: Elementary, level A1 in the European Language Scale

